University of Nottingham
UK | CHINA | MALAYSIA

Optimisation of a Protocol for the Study of Subcellular cAMP Compartmentalisation in Epithelial Cells of *Drosophila Melanogaster*

Submitted September 2022, in partial fulfilment of the conditions for the award of the degree ***Masters of Research***

Isabelle Forder-Denham, BSc

Student ID- 14325096

Supervised by Dr Marios Georgiou & Dr Isabella Maiellaro

School of Life Sciences
Division of Physiology, Pharmacology and Neuroscience
University of Nottingham

Table of Contents

Acknowledgements

I would like to thank Marios Georgiou and Isabella Maiellaro for their constant support, reassurance, encouragement and the opportunity to undertake such an enriching project. I appreciate all of their help, advice and good ideas; every time I needed support or career advice they were always there. I definitely would not have been able to finish this year without them! I'd like to thank the members of the Georgiou Lab: Zsuzsa Markus, Carver Wong and in particular Emma Szamek (my lab big sister) for making me feel so welcome in the lab, always sharing invaluable advice or 'gems of wisdom' about research or the project and all of the coffee breaks. I am so grateful for their kindness and patience, I would've been lost without their continual support and encouragement through all of the successes and failures. I would also like to thank the SLIM Team, in particular Robert Markus and Ian Ward who provided me with invaluable experimental design tips and technical advice regarding confocal microscopy and FRET experiments.

Finally, I'd like to thank Hannah Bailey, Jessica Petts and Mahari Rodrigo for going on the research journey with me and sharing all of the ups and downs. I'd also like to thank my housemates Evangeline Richardson and Jack Wilson for putting up with my grumpiness after a long lab day, in addition to being pillars of support and helping me cultivate a life outside the lab throughout the project.

Abstract

Rationale

The coordination and regulation of actin-based structures throughout the cell is tightly spatiotemporally regulated and linked to spatiotemporal activation of key players in actin polymerisation and de-polymerisation (Rac, RhoA and Cdc42). cAMP (cyclic adenosine monophosphate) and its effectors have been linked to the regulation of RhoGTPases Rac, Cdc42 and RhoA providing a convincing mechanism for their regulation, although direct evidence is not forthcoming due to limitations in currents methods of studying cAMP signalling dynamics within the cell. Most previous work has measured cAMP dynamics and concentrations within *in vitro* or within subcellular fractions, potentially conferring a misleading representation of cAMP dynamics. Here we present an optimised protocol for studying cAMP dynamics *in vivo* within live *Drosophila melanogaster* pupae, overcoming previous limitations in characterising cAMP dynamics in the study of actin membrane-based protrusions.

Methods

Using the Gal4-UAS system and the MARCM system, we expressed a genetically encoded cAMP FRET-based (Förster resonance energy transfer) biosensor within well-spaced epithelial cells and in epithelial cell clones in *Drosophila melanogaster,* using the tissue specific promoters Neuralized, in well-spaced epithelial cells, and Pannier, in epithelial cell clones, to restrict expression to the notum. Our aim was to employ this protocol in the measurement of cAMP gradients within actin membrane-based protrusions at high spatial resolution.

Results

We successfully created and optimised a confocal microscopy protocol for undertaking sensitised emission FRET measurements to assess localised cAMP gradients within intermediate-lateral actin protrusions in live *Drosophila melanogaster* pupae. This protocol overcomes current limitations in measuring cAMP signalling dynamics by providing high spatial resolution, allowing researchers to link precise cAMP domains to alterations in cellular morphology and interrogate the signalling events underpinning actin membrane-based protrusion dynamics. We observed statistically significant elevated relative basal cAMP concentrations within the tip of intermediate-lateral protrusions compared to the protrusion middle or base and cell cytosol within well-spaced epithelial neu-camps-epac1^{+}cells, expressing a genetically encoded FRET-based cAMP biosensor. However, no statistically significant difference in relative cAMP concentration was detected within epithelial pnr-camps-epac1^{+} clones at any point within the cell cytosol or protrusions.

Conclusion

Our preliminary data highlights the utility of this approach to measure cAMP gradients at high spatial resolutions within three-dimensional, polarised cells in a live organism. We conclude that further exploratory work is required to the elucidate the full extent of the role for cAMP in actin protrusion regulation, while this represents a promising avenue for exploration.

Chapter 1: Introduction

1.1 cAMP, a Small Nucleotide with Diverse Functions

1.11 An Introduction to cAMP Signalling

Following its discovery in 1956 by Earl Sutherland, whose seminal work regarding the cellular mechanisms and actions of cAMP (cyclic adenosine monophosphate) within several notable metabolic processes earned a him Nobel Prize, the second messenger cAMP has since been implicated in the signal transduction and regulation of a diverse range of biochemical processes(Berthet et al., 1957). cAMP functions to translate the message of an extracellular cue, such as a hormone, neurotransmitter or other ligand, transduced by an extracellular receptor to the intracellular environment, prompting activation of the corresponding signalling cascade to instigate the physiologically appropriate response to the extracellular 'message'(Zaccolo et al., 2021). Of course, it would be impossible for cAMP to enact these functions alone, therefore it is accompanied by integral components of the signalling pathway: its activators G-Protein Coupled Receptors (GPCRs) and adenylyl cyclase (AC), the secondary effectors Protein Kinase A (PKA) and Exchange Protein-Directly Activated-By cAMP (EPAC), in addition to its terminator- phosphodiesterases (PDEs)(McCormick and Baillie, 2014). The deluge of studies in the decades following the initial isolation of cAMP characterised these important members of the cAMP signalling pathway(Sassone-Corsi, 2012).

1.12 Components of the cAMP Signalling Pathway

1.121 G-Protein Coupled Receptors and Adenylyl Cyclase

GPCRs are the largest family of transmembrane receptors, with up to 1000 different receptors encoded within the human genome(Yang et al., 2021). They transduce stimuli from a wide range of ligands including neurotransmitters, hormones, and inflammatory molecules and can be found in practically all cells within the body(Rosenbaum et al., 2009). X-ray crystallography studies, initially crystallising rhodopsin in 2000 and later the β2-adrenergic receptor, provided key insights into the structure and function of GPCRs(Rasmussen et al., 2011, Palczewski et al., 2000). Crystallisation studies confirmed that GPCRs consist of seven transmembrane helices connected to three extracellular loops (ECLs), adjacent to the N-terminus, and three intracellular loops (ICLs), located next to the C-terminus, coupled to a G-protein(Latorraca et al., 2017). Heterotrimeric G-proteins are comprised of an alpha, beta and gamma subunit which transduce agonist binding, transferring agonist signal to the intracellular environment. GPCRs exist in a continual state of spontaneous fluctuation between a series of conformations. Plotting of a molecular dynamics simulation trajectory for the β2-adrenergic receptor, clustered conformations into three categories- inactive, intermediate and active, some of which have been revealed through crystallisation of GPCRs in different states(Dror et al., 2011). The classical mechanism of action for GPCRs involves binding of an extracellular ligand to the ligand-binding site, differentially located in different receptor classes, inducing a conformational change within the GPCR(Latorraca et al., 2017). It is proposed that such conformational changes stimulated by ligand binding may take the form of increased population time (time expended in a particular conformation) of the GPCR within the active conformational states or promote adoption a new conformation(Dror et al., 2011). The specific structural alterations bestowed by these

conformational modifications include rearrangement of the transmembrane helices and binding pocket contraction.

There is loose coupling of agonist binding with G-protein binding; agonists bind with higher affinity while GPCRs are in the G-protein bound active state, while alterations in the structure of the GPCR ligand-binding pocket, upon ligand binding, increases affinity of the GPCR to G-proteins, although ligand-binding does not determine coupling(Hill, 2006). Following receptor activation, Gα-bound GDP is substituted for GTP, thus provoking a conformational change of the Gα subunit decreasing its affinity for Gβγ subunits and from the receptor itself, prompting Gα dissociation(Wootten et al., 2018). The most well-known forms of the Gα subunit, Gαi and Gαs, exert opposing effects on AC activity, hence contrasting effects on cAMP production(Zaccolo et al., 2021). Gαs favours binding and activating one of the nine mammalian membrane-bound AC isoforms, via the newly exposed binding site, following Gαs dissociation from Gβγ(Rosenbaum et al., 2009). Activated ACs work quickly to convert adenosine triphosphate (ATP) to cyclic adenosine monophosphate (cAMP), amplifying the signal. There are nine membrane-bound isoforms of AC and only one soluble AC, which are differentially localised and respond to different modulators, thus increasing the compartmentalisation of cAMP signalling(Taussig, 2013). Integration of signals from several GPCRs can further heighten cAMP production; addition of the histamine H_1 receptor to the adenosine receptor was found to greatly enhance cAMP production in guinea-pig hippocampi sections(Selbie and Hill, 1998). Not only do GPCRs signal from the cell surface, but upon receptor internalisation to endosomal cellular compartments subsequent to activation, GPCRs can continue signalling(Calebiro and Godbole, 2018). Initially, evidence suggested GPCR internalisation was a mechanism of signal desensitisation to terminate receptor stimulation, but recent evidence showed that internalisation is required for prolonged signalling induced by some hormones including thyroid

stimulation hormone (TSH)(Calebiro et al., 2009, Calebiro and Godbole, 2018). Therefore, signal specificity- ensuring that each input produces the appropriate response, is of utmost importance. This is especially pertinent due to the exceedingly diffusible nature of cAMP. Rapid production of cAMP by ACs could lead to the homogenisation of cAMP concentrations throughout the cell, producing a myriad of non-physiologically relevant responses and reducing signal specificity(Anton et al., 2022). Furthermore, due to the sheer number of GPCRs available for expression within a cell (~100), discriminating between inputs could be problematic. Therefore, a system of compartmentalisation must exist to ensure the spatiotemporal specificity of signals.

Adding to the spatiotemporal regulation of GPCR signalling, differential coupling of ACs at the plasma membrane to different signalling components allows activation of different responses upon different stimuli. For example, different local responses were detected upon measurement of cAMP concentrations in a pituitary cell line which responds to two different stimuli, thyrotropin-releasing hormone and vasoactive intestinal peptide, to produce prolactin. Additionally, association of ACs with AKAPs (A-Kinase Anchoring Protein, anchoring proteins which confine PKA localisation to discrete sites in the cell), PDEs (enzymes which catalyse the breakdown of cAMP) and GPCRs within a complex further increases cAMP compartmentalisation and facilitates feedback inhibition via PKA (figure-1). AC5, 6 and 8 were found to undergo feedback inhibition through PKA whereas AC2 enjoyed feedforward regulation through protein kinase C (PKC)(Bauman et al., 2006, Willoughby et al., 2012, Efendiev et al., 2013, Shen and Cooper, 2013). This evidence all points towards a mechanism of compartmentalisation for cAMP signalling.

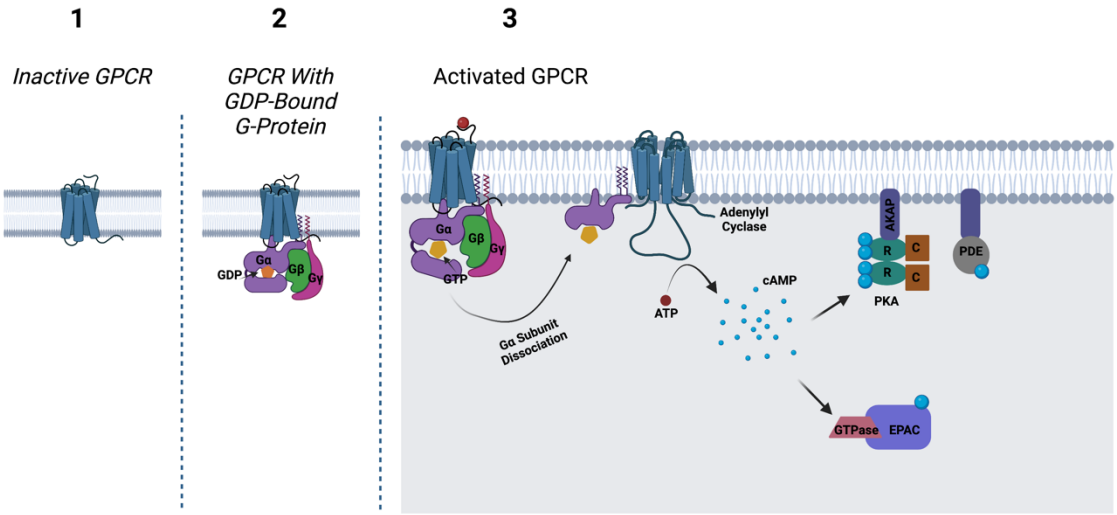

Figure 1- The different states of GPCR activation and cAMP signalling. *(1) Inactive GPCR, not bound to a G-Protein. (2) GPCR bound to inactive G-Protein, note GDP is bound to the Gα subunit. (3) Active GPCR bound to G-protein. Gα dissociates and binds to adenylyl cyclase, which catalyses conversion of ATP to cAMP. Some cAMP binds to secondary effector EPAC and four molecules of cAMP bind to secondary effector PKA, which is tethered to a specific cellular location by AKAP. Figure modified from (Wong and Scott, 2004).*

1.122 Protein Kinase A

The heterotetramer protein kinase A is one of the secondary effectors of cAMP signalling, consisting of two regulatory (R) and two catalytic subunits (C) (Zaccolo et al., 2021). There are four forms of the R subunit including RIα, RIβ, RIIα and RIIβ whereas only three forms of the C subunit exist: Cα, Cβ and Cγ(Taylor et al., 2013). cAMP binding to the R induces their conformational change preventing dimeric R subunit binding and blocking of dimeric C subunits which would have the effect of C subunit catalytic inhibition(Taylor et al., 2005). RI-type subunits are activated by cAMP at lower concentrations than RII-type subunits aiding concentration-dependent activation upon different stimuli and contributing to cAMP signalling compartmentalisation(Dostmann et al., 1990).

1.123 A-Kinase Anchoring Protein

Association of AKAPs with PKA, via the conserved dimerisation-docking domain at the R subunit N-terminus, provides anchoring of the PKA holoenzyme to specific localities proximal to their targets. Not only does this boost signalling efficiency, but it also provides specificity and adds to the compartmentalisation of cAMP signalling(Zaccolo et al., 2021). In addition to PKA binding, AKAPs have also been found to associate with GPCRs, ACs, phosphatases and PDEs(Malbon et al., 2004, Piggott et al., 2008, Dessauer, 2009, Dodge-Kafka et al., 2010, Coghlan et al., 1995, Dodge et al., 2001, Scott et al., 2013). This could provide a further mechanism by which signal specificity and compartmentalisation is achieved- the assembly of AKAP-based signalosomes. Evidence for this is forthcoming; models of mitogen-activated protein kinase and epidermal growth factor receptor scaffolds implicates the existence of signalosomes which work to enhance signal efficiency by bringing components of the MAPK signalling within close proximity of each other(Burack and Shaw, 2000). Furthermore, AKAP clusters localised to membranes have been detected. This could increase buffering capability by increasing local concentrations of PKA, thus correspondingly increasing local concentrations of the PKA R subunit which cAMP is known to bind to. This could prevent free diffusion of cAMP throughout the cell, limiting downstream effects of cAMP to local effectors(Mo et al., 2017).

1.124 Exchange Protein-Directly Activated by cAMP

Two forms of the cAMP secondary effector Epac exist, Epac1 and Epac2, which act as guanine nucleotide exchange factors for Rap1 and Rap2 respectively(Bos, 2006). Rap activation through cAMP is known to be independent of PKA and has a multitude of effects throughout the cell, including but not limited to cytoskeletal remodelling, cell polarity, proliferation and differentiation(Robichaux and Cheng, 2018). Rap is a small Ras-like GTPase, a member of the Ras superfamily of G proteins which interchange between active GTP-bound and inactive GDP-bound

states. EPAC is differentially localised which adds to its role compartmentalising cAMP signalling. EPAC1 localises to the plasmalemma, sarcoplasm and perinuclear region whereas EPAC2 localises to the T-tubules(Cazorla et al., 2009, Pereira et al., 2013, Li et al., 2006). T-tubules are cell membrane extensions found within cardiac cells, functioning to couple excitation with contraction. Furthermore, activation of EPAC upon cAMP stimulation demonstrated that Epac1 and Epac2 exert differing physiological functions in a similar fashion to PKA, hinting that they could be controlled by different cAMP pools. For example, the β-arrestin-EPAC1 signalosome has been detected at the plasma membrane upon activation of β_2-adrenoceptor, whereupon it stimulates Rap2, Ras and CaMKII to induce pro-hypertrophic signalling(Berthouze-Duquesnes et al., 2013). Epac2, localised to the T-tubules, is also activated upon adrenoceptor activation but, in contrast to Epac1, it is stimulated by β_1-adrenoceptor to promote calcium release from the sarcoplasmic reticulum(Pereira et al., 2013).

1.125 Phosphodiesterases

PDEs are an important component of cAMP compartmentalisation. Although different isoforms possess an overall similar structure, a highly conserved C-terminus catalytic domain with dissimilar N-termini between isoforms, they possess differing binding affinities, targeting components and regulatory elements(Bender and Beavo, 2006). Therefore, this permits specific regulation of cAMP at different cellular locations adding to the compartmentalisation of cAMP signalling. However, what puzzles researchers is the slow kinetics of PDE action. Given that the diffusion coefficient for cAMP has been calculated at a speedy 40$\mu m^2/s$, it is unclear how PDEs act to prevent fast diffusion of cAMP to ensure signal compartmentalisation and specificity(Richards et al., 2016, Nikolaev et al., 2004). Early work demonstrated that PDE inhibition resulted in a decrease in cAMP within cellular fractions to less than 20% of its normal concentration, despite a 3.4-fold increase in

cAMP following stimulation of cAMP(Hohl and Li, 1991). This appears to lend credit to the idea of cAMP compartmentalisation by PDEs within the cell. However, it is important to remember that much of this early work was conducted in cell lysates as real-time cAMP tools for measurement in intact cells were limited, thus limiting the conclusions which can be drawn from *in vitro* work. However, later work involving the use of FRET-based biosensors in intact cells has cemented the role of PDEs in cAMP compartmentalisation, although it is clear that PDEs do not act alone to induce signal specificity(Zaccolo and Pozzan, 2002, Nikolaev et al., 2004, Leroy et al., 2008, Surdo et al., 2017).

1.126 Phosphatases

Phosphatases are a group of multimeric enzymes which modify the phosphorylation state of PKA; dephosphorylation leads to PKA deactivation via serine/threonine phosphatases (PP1, PP2A and PP2B)(Zaccolo et al., 2021). Differential expression of these phosphatase isoforms is yet another way of generating nuance and compartmentalisation of cAMP signalling. For example, different isoforms of PP1 have been found to differentially localise to the heart, longitudinal sarcoplasmic reticulum and the junctional sarcoplasmic reticulum(Herzig and Neumann, 2000, Aoyama et al., 2011). Moreover, increased concentrations of phosphatases within the cytosol as compared to the mitochondrial membrane suggest that increased phosphatase concentration within the cytosol could provide PKA compartmentalisation as detected by FRET reporters, although there is no direct evidence for this hypothesis(Burdyga et al., 2018).

1.13 cAMP Compartmentalisation: Nanodomains

Direct evidence promoting the existence of so-called microdomains of cAMP signalling within the cell first began to emerge in the late 1990s and early 2000s, although the idea of cAMP compartmentalisation was first postulated some twenty years previously(Garber, 1980, Cadd and McKnight, 1989, Dostmann et al., 1990, Hohl and Li, 1991, Zhang et al., 2001, Dodge et al., 2001, Houslay and Milligan, 1997). Work conducted in rat neonatal cardiac myocytes, taking advantage of newly developed cAMP FRET-based biosensors, revealed the existence of cAMP pools with an approximate 1μm of action upon stimulation of the β-adrenergic receptor(Zaccolo and Pozzan, 2002). Treatment of cells with a cAMP stimulator revealed discrete compartmentalised increases in cAMP within myocyte striations in comparison to non-striated areas(Zaccolo and Pozzan, 2002). Furthermore, only PKA anchored to AKAPs specifically localised within the domains were shown to successfully detect alterations in cAMP concentration, following analysis of GFP-tagged PKA anchored to AKAP, hinting at a mechanism for signal stimulation of the physiologically appropriate response for a stimulus(Zaccolo and Pozzan, 2002). Inhibition of PDEs using a broad-spectrum inhibitor generated a greater increase in cAMP concentration than β-adrenergic receptor maximal stimulation(Zaccolo and Pozzan, 2002). In combination with the revelation that PDEs could specifically localise to distinct cellular regions through association with AKAPs, this provided convincing evidence for the compartmentalisation of cAMP signalling within nanodomains(Dodge et al., 2001).

Recent work has only added to these solid foundations. Direct measurement of cAMP dynamics within intact cells using a cell-permeable fluorescent cAMP analogue, disclosed that cAMP buffering restricted cAMP diffusion dynamics within the cell(Bock et al., 2020). The idea of cAMP buffering involves the notion that cAMP binding to intracellular binding sites limits the amount of cAMP available for free

diffusion within the cell. This provides a persuasive counter to the argument against the existence of cAMP nanodomains as it conveniently explains how, if cAMP is freely diffusible, signal compartmentalisation exists. It is also one which is substantiated by experimental evidence. Recently developed fluorescent cAMP analogues were shown to possess equivalent cAMP binding and activation properties, in addition to PDE degradation resistance, making them a powerful tool to assess intracellular cAMP diffusion(Bock et al., 2020). Experiments revealed cAMP diffusion within the cell is slow(Bock et al., 2020). Spatiotemporal Image Correlation Spectroscopy (STICs), whereby diffusion coefficients of fluorescently labelled molecules within the cell are measured using temporal and spatial correlation lags for intensity fluctuations via laser-scanning microscopy, was used to assess fluorescent cAMP analogue diffusion within intact HEK293 cells(Hebert et al., 2005, Bock et al., 2020). This exposed cAMP possessed diffusion rates matching those of bound cAMP state, at low basal cAMP levels(Bock et al., 2020). cAMP is able to overcome buffering, but only upon PDE inhibition and AC stimulation, at which point cAMP concentration increased adequately to inundate nanodomains and the cell as a whole, measured using cAMP-Epac1 nanorulers within HEK293 cells(Bock et al., 2020). Specific tethered-PDE inhibition stimulated a substantial increase in cAMP concentration surrounding the sensor, of approximately 10nm or less(Bock et al., 2020). Therefore, evidence proposes that at basal state, low cAMP nanodomains exist maintained by specific and localised PDE activity(Bock et al., 2020). Moreover, low cAMP domains were showed to exert power over localised PKA activity. PKA activity reporters fused to a corresponding PDE demolished PKA activity, whereas expression of the PKA activity reporter alone was found to produce ample signal in HEK293 cells(Bock et al., 2020). Not only does this work illustrate nanometre cAMP concentration gradients but it directly correlates gradients PKA activity providing insights into the facilitation of responses at a nanometre scale. Furthermore, much previous work has

often relied upon cell cytosol preparations for analysis of cAMP compartmentalisation, producing significant yet limited results as *in vitro* work often fails to accurately replicate normal physiological conditions. Although the experiments discussed above also assayed cell cytosol preparations, much of the work was undertaken in intact cells using fluorescent probes which allow the measurement of real-time cAMP concentrations, making these findings even more promising.

However, many computational studies simulating the existence of cAMP gradients within the cell failed to reproduce compartmentalisation through only PDE action and catalytic PDE activity was found to be inadequate to restrict cAMP diffusion. Although recent studies of cAMP concentration indicated lower cytosolic cAMP concentrations than previously estimated which could suggest that subcellular cAMP concentrations fall within the kinetic limits of PDE activity, recent work has shown that 100 to 1000-fold slower cAMP diffusion is required. Therefore, other factors contributing to cAMP compartmentalisation could be at play. Adding to this growing evidence, the idea of phase separation within the cell as a mechanism of cAMP compartmentalisation is an interesting addition. Phase separation is a relatively recent theory within cell biology. It refers to the idea that a well-mixed macromolecular solution, such as those found within the cell containing proteins or key signalling molecules, could spontaneously and stochastically separate into two components, i.e. phases(Boeynaems et al., 2018). One phase is the dense phase, so named as it is ample with the macromolecule in question. The other phase is dubbed the dilute phase, which contains little to no macromolecule. Phase separation has already been implicated in many biological concepts from the development of membrane-less organelles to the control of gene expression and in the control of signalling pathways, such as Wnt, in disease contexts.(Esposito et al., 2021, Bhat et al., 2021, Boeynaems et al., 2018).

Recent work uncovered phase separation of key cAMP signalling components within the cell could also contribute to cAMP compartmentalisation. Initial experiments regarding the structure and function of PKA demonstrated that the Riα PKA subunit is essential for regulation of PKA activity(Cadd and McKnight, 1989). Contemporary work proposed that phase separation of Riα could contribute to the enactment of cAMP compartmentalisation. Introduction of GFP-labelled Riα within HEK293A cells revealed the existence of dynamic puncta in which Riα was exchanged from and to diffusible pools following Fluorescence Recovery After Photobleaching (FRAP) experiments. Additionally, application of an intermolecular force disruption agent provoked a 68% decrease in the number of puncta observed within cells. Moreover, high concentrations of cAMP were detected within Riα condensates leading the authors to propose that condensates could act as cAMP buffers. These theories were corroborated by experiments disrupting Riα condensates which resulted in an increase of cAMP concentration around PDEs, thus indicating that interruption of Riα could lead to loss of cAMP buffering(Zhang et al., 2020). Sequestration of cAMP in this way, by phase separation, could lower free cAMP concentrations sufficiently to be controlled by PDEs. Although these findings are certainly an intriguing proposition, many questions still remain. For example, are other components of the cAMP signalling pathway also enclosed within droplets? How is droplet formation controlled? Further evidence corroborates the existence of phase-phase separation in cAMP signalling as PKA C subunits were shown to co-phase in addition to Riα subunits(Zhang et al., 2020). The authors suggest that if the phase also contained a PKA phosphorylation target, this could create a nanodomain in which PKA-dependent phosphorylation could occur, where cAMP concentration is comparatively elevated to its surroundings(Zaccolo, 2021). However, this is yet to be confirmed.

Intriguingly, recent work taking advantage of FRET-based cAMP biosensors proposed the existence of Receptor Associated Independent Nanodomains (RAINs) within intact HEK239A cells(Anton et al., 2022). Two different GPCRs GLPR1 and the β2-adrenergic receptor were stimulated and the distance of a cAMP from the GPCR was assessed using molecular nanorulers. The nanorulers consisted of a single-alpha helical domain linker which was incorporated into the GPCR GLPR1 to enable placement of a cAMP biosensor at set distances from the receptor, whereby fluorescence was assessed using dSTORM microscopy techniques(Anton et al., 2022). The authors demonstrated the existence of RAINs which reached tens of nanometres from the sensor(Anton et al., 2022). They stipulated that, as this was also found to be the case for the β2-adrenergic receptor, it could be an effect common to all GPCRs, although this has not yet been proved to be true. Such RAINs were found to be insulated from the cAMP signals generated by other GPCRs as cAMP pools did not equilibrate with cytosolic cAMP or with pools generated by the β2-adrenergic receptor where measurements of the GLPR1 were undertaken(Anton et al., 2022). However, an important consideration of all data obtained within cell lines, especially simple cell lines such as HEK293A, is not representative of the more complex nature of cells found within organisms such as neurones or fibroblasts. Furthermore, the authors note that further work is required to assess change in RAINs over time and stimulus strengths required to stimulate gradient formation(Anton et al., 2022). To this end, recent work has moved to quantify cAMP gradients in living organisms. Employing the use of a genetically encoded cAMP FRET-based sensor, cAMP compartments within *Drosophila melanogaster* were identified within the range of micrometre dimensions(Maiellaro et al., 2016). Upon local cAMP stimulation, swift increases in cAMP concentration were detected within the bouton which possessed a range of 15μm(Maiellaro et al., 2016). Not only is this finding exciting as it demonstrates the presence of cAMP gradients within a more complex cell system, but measurements

were undertaken *in vivo* within a 3D intact, live organism which provides much greater insight into physiologically relevant real-time cAMP gradients and compartmentalisation.

1.2 The Actin Cytoskeleton: Its Form, Function and Regulation

1.21 An Introduction to the Actin Cytoskeleton

Cells respond to a variety of different stimuli such as growth factors, chemokines, cytokines and even cAMP to provoke the activation of cell signalling cascades which control the actin cytoskeleton. The main convergence point for cascades is the Rho-family of GTPases, including Rac, RhoA and Cdc42 which regulate actin nucleation, actin disassembly and stress fibre contraction proximal to the plasma membrane(Hall, 1998). There is an emerging body of evidence linking cAMP signalling with regulation of Rac, RhoA and Cdc42 through secondary effectors PKA and EPAC. However, specific spatiotemporal localities of signalling events within actin protrusions and their association with cAMP gradients remains relatively uncharacterised.

Polarised epithelial sheets are formed by tightly packed layers of cells which act as plastic barriers, providing mechanical strength and strong links between cells within the sheet(Lee and Streuli, 2014). The establishment and maintenance of apicobasal cell polarity is essential to the coordination of a diverse range of actin-based structures throughout the cell, in addition to accurate cell-cell junction positioning and successful coordination of activities throughout the tissue(Georgiou and Baum, 2010). Spatiotemporal regulation of the of the actin cytoskeleton aids coordination of these processes. Activation or inhibition of the appropriate signalling pathway at the correct time ensures transduction of the physiologically appropriate response to the corresponding stimuli, thus coordinating these actions. Furthermore, it is well-established that the mis-regulation of the actin cytoskeleton can significantly contribute to or lead to the development of a wide variety of disease states including metastasis in cancer, respiratory disorders such as COPD or asthma and neurological disorders(Canales Coutiño et al., 2020, Yang et al., 2018, McMurray, 2000). Therefore,

understanding the mechanisms and signalling pathways contributing to the spatiotemporal regulation of actin cytoskeleton can help develop our knowledge of abnormal cytoskeletal functioning within a disease state.

1.22 Actin Polymerisation and Contraction

Alterations in actin polymerisation and depolymerisation within the cell is tightly regulated leading to actin assembly and disassembly at the cell plasma membrane. The process of actin treadmilling, whereby tinsel-like actin filaments transition from their monomeric G-actin and filamentous F-actin form, is ATP-driven (figure-2)(Svitkina, 2018). ATP-bound actin monomers are added the asymmetric actin filament at the plus end, whereas GDP-bound actin dissociates at the minus end(Lee and Dominguez, 2010). This is catalysed by the intrinsic ATPase activity within actin, under the regulation of actin-binding proteins (ABPs) which control nucleation, elongation, capping, severing and cross-linking(Lee and Dominguez, 2010). In turn, ABPs are spatiotemporally regulated by RhoGTPases; Rac, Cdc42 and RhoA act as molecular switches to regulate formation and breakdown of actin-based protrusions such as stress fibres, filopodia and lamellipodia(Raftopoulou and Hall, 2004, Etienne-Manneville and Hall, 2002, Tapon and Hall, 1997). While RhoGTPases are in their GDP-bound state, they are inactive. Regulation by guanine nucleotide

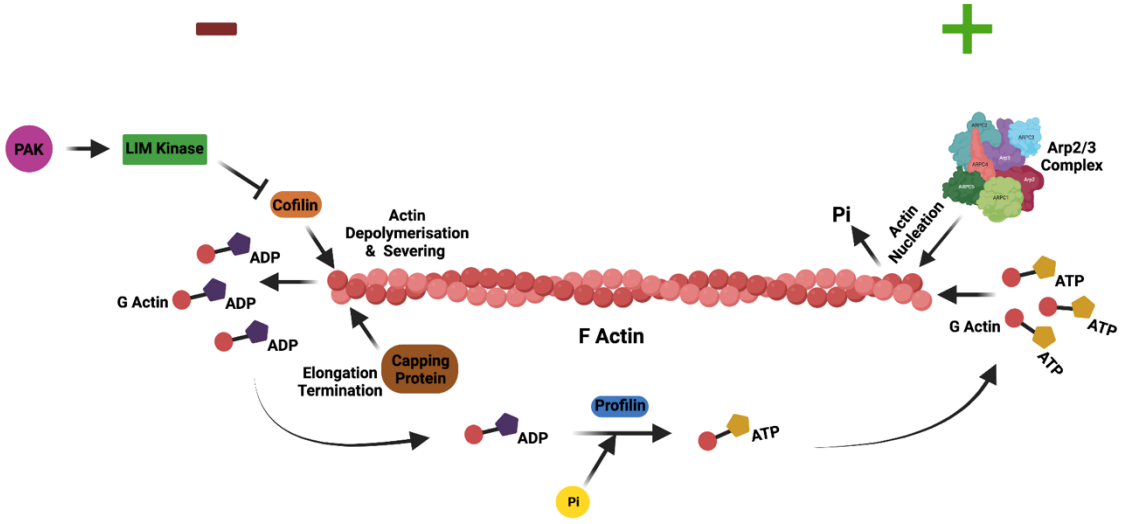

Figure 2- The process of actin treadmilling. *GTP-bound G-actin subunits are added to the plus end and GDP-bound G-actin subunits dissociate from the minus end. Cofilin catalyses actin depolymerisation and subunit severing, while capping proteins terminate elongation at the minus end. Cofilin can be inhibited by LIM kinase, which is activated by Protein Activated Kinase (PAK). The Arp2/3 complex works at the plus end to increase actin nucleation. Profilin catalyses exchange of G-actin GDP for GTP.*

exchange factors (GEFs) promote GDP release, permitting GTP to take its place. Inactivation occurs through catalysis of RhoGTPase intrinsic GTPase activity by GTPase-activated proteins (GAPs) (figure-3)(Spiering and Hodgson, 2011). Further inhibition is enacted by Rho guanine nucleotide dissociation inhibitors (GDIs) which bind to RhoGTPases preventing GDP dissociation. Not only does this prohibit RhoGTPase-membrane interaction but it also prevents binding of their downstream targets, inactivating them(Clayton and Ridley, 2020). Often, GDI binding can direct RhoGTPases to membrane compartments or protein complexes, for example RhoGDIα directs Cdc42 plasma membrane localisation(Lin et al., 2003). Therefore, tight control of the concentration of the ratio between G-actin and F-actin within the cell and dynamic ratio alterations in response to external stimuli is important(Ridley et al., 1992, Ridley and Hall, 1992, Tapon and Hall, 1997).

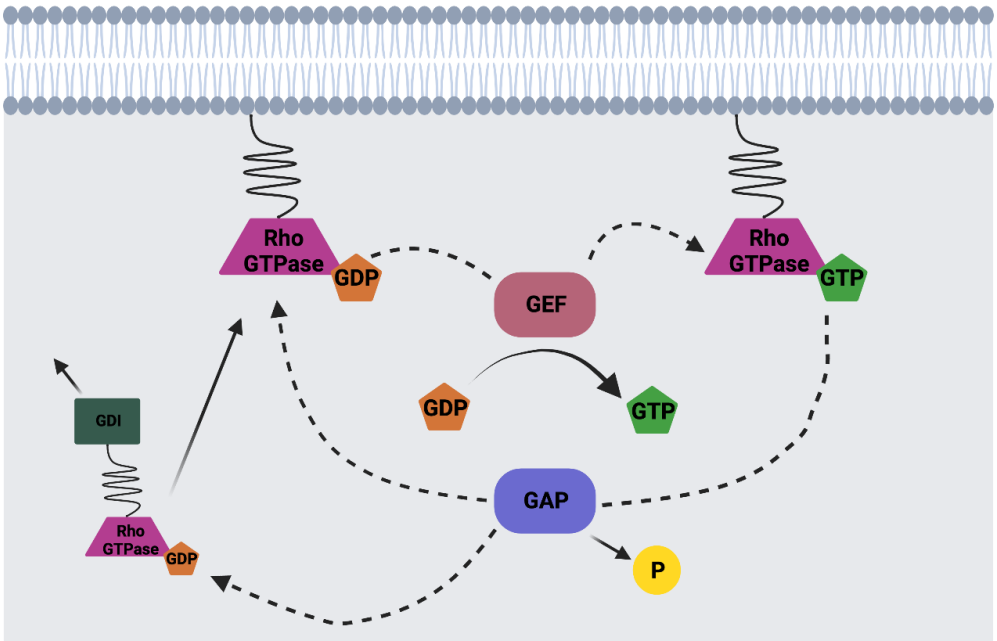

Figure 3- The mechanism of action for Rho GTPases. *In their GDP-bound state, Rho GTPases are inactive, whereas when GTP is bound, they transition to the active state. GEFs fascilitate the exchange of GDP for GTP activating RhoGTPases. GAP aids inactivation by preventing GDP exchange. RhoGTPases bound to GDIs are relocated to the cytoplasm. Figure adapted from (Biro et al., 2014)*

RhoGTPases have a number of downstream targets which affect actin polymerisation (figure-4).

Moreover, the small GTPases also regulate each other; Cdc42 can stimulate Rac activity which can in turn promote activation of RhoA. RhoA on the other hand, can stimulates inhibition of Rac activity(Hall, 1998). Furthermore, different localities within the cell exhibit different levels of Cdc42, Rac or RhoA concentration and it is the differential activation of these three RhoGTPases which leads to the formation of different structures. For example, the leading edge of migrating cells enjoys higher activation of Rac and Cdc42 which promote actin nucleation to focal adhesions(Raftopoulou and Hall, 2004). Whereas, the lagging edge in migrating cells experiences greater activation of RhoA to facilitate actin depolymerisation and contraction. It is the

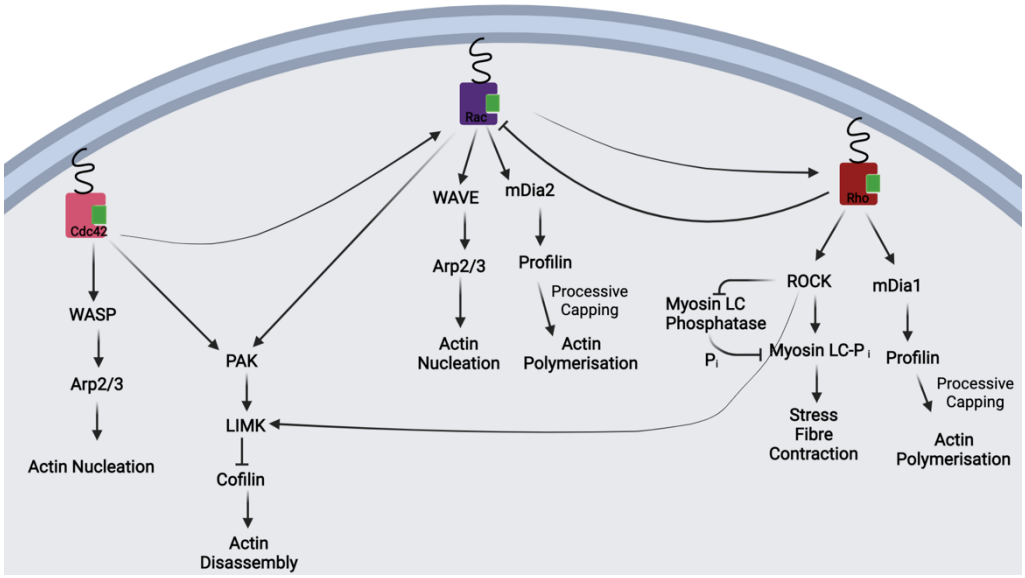

Figure 4- *Complex interplay and differential activatiton between three key Rho GTPases Cdc42, Rac and RhoA is required in the spatiotemporal regulation of actin polymerisation. Figure adapted from (Lodish, 2016).*

stimulation of pathways by RhoA that lead to Rac inactivation at the lagging edge; this prevents formation of leading-edge structures at the lagging edge(Devreotes and Horwitz, 2015). This further emphasises the importance of the correct spatial regulation of RhoGTPases within the cell.

1.23 Mechanisms of cAMP Control in Actin Cytoskeleton Remodelling and Protrusion Formation

The role of cAMP signalling in the regulation of the actin cytoskeleton has remained elusive. An emerging body of evidence appears to link cAMP secondary effectors in the regulation of key mediators of actin cytoskeletal organisation, the small GTPases Rac, RhoA and Cdc42. Much evidence relates to actin-based cell migration, whereby front-rear polarised cells polymerise actin, under the regulation of Rac and Cdc42, to form filopodia and lamellipodia the front of the cell which contact focal adhesions to pull the cell forward(Jansen et al., 2018). Meanwhile, actin-depolymerisation occurs at the rear of the cell, coordinated by RhoA, inducing contraction to further induce forward propulsion. This is an important example of the importance of the differential activation of Rac, Cdc42 and RhoA at different spatiotemporal points to coordinate forward motion. Evidence regarding the precise role of cAMP in increasing or decreasing actin polymerisation via PKA and EPAC is conflicting, however as signals are multimodal and context specific (i.e. the downstream effect of cAMP signals are dependent on the stimulus and location within the cell) this is to be expected (table-1, table-2). However, much evidence linking cAMP signalling with actin cytoskeleton remodelling is circumstantial and limited by *in vitro* experiments using simple cell lines which do not accurately represent the true physiological environment of the cell. Additionally, many studies were undertaken in the yeast *Dictyostelium discoideum* or using slug cells, thus it is unclear whether these findings translate to other organisms such as *Drosophila.* There is also evidence that regulation of actin-based chemotaxis is under control of different pathways, such as calcium signalling rather than cAMP(Hashimura et al., 2019). Supporting this notion, the downstream effects of cAMP signalling are cell and tissue specific, therefore contradicting implications of cAMP could be explained by this(Kumar et al., 2017, Kumar et al., 2018, Ichikawa et al., 2018). For example, increases in

cAMP concentration at the cell front could indeed increase actin polymerisation. Equally, such elevations in cAMP at the cell rear could serve to decrease actin polymerisation and stimulate fibre contraction. However, no direct cAMP measurements have been undertaken within actin-based protrusion therefore the true role of cAMP within actin protrusion regulation is uncharacterised. This highlights the need for a reliable protocol for measuring cAMP dynamics *in vivo* with high spatiotemporal regulation.

Table 1- Evidence for the role of cAMP in decreasing cell migration via the regulation of the actin cytoskeleton

Evidence	***Reference***
• Cells are capable of sensing cAMP gradients which prompted the engagement of chemotaxis, cell migration up a concentration gradient in the yeast Dictyostelium discoideum	Fukujin, 2016; Garcia, 2013; Hashimura, 2019 ; van Haastert, 2007
• Activation of cAMP receptors in yeast Dictyostelium discoideum induced PI3-kinase signalling via G-proteins producing phosphatidylinositol-3,4,5-triphosphate at the plasma membrane of the leading edge correlating with re-localisation of an AC regulator, Cytosolic Regulator of Adenylyl Cyclase (CRAC)	van Haastert et al., 2007
• cAMP was secreted by Dictyostelium discoideum cells and prompted them to also produce cAMP correlating with an increase in actin polymerisation	van Haastert et al., 2007
• The presence of pseudopods, (an actin-based protrusion) including lamellipodia and filopodia, was detected at the site of PIP3 increase at the membrane accompanied by an increase in migration up a cAMP gradient	Garcia et al., 2013
• cAMP microinjection into slug cells was also correlated with an increase in cell migration	Garcia et al., 2013
• cAMP-induced activation of Epac upon axon injury in neurones led to inside-out integrin signalling, ultimately provoking	Sakai et al., 2021

activation of RhoA-ROCK signalling through the MLC kinase pathway, which is known to increase rates of actin filament contraction in C. eleans	
• cAMP-induced activation of Rap1 and Rap2 via Epac1 stimulates the ERK pathway, alpha$_V$-beta$_3$ integrin (in melanoma) and integrin beta-1 (in pancreatic cancer)	Kumar et al., 2018)
• Treatment of breast cancer cells with an Epac1 inhibitor demonstrated reduced migration in a Transwell Migration Assay	Ichikawa et al., 2018, Kumar et al., 2017)
• PKA phosphorylation of CIP4 at T225 was correlated with increased cell migration • A wound-healing where cells allowed to migrate for 6 hours revealed that the phosphomimetic mutant (CIP4E) increased migration compared to wild-type CIP4 • A non-phosphorylatable mutant of CIP4 decreased migration • PKA inhibition duing a Boyden migration assay revealed an increased number of cells in lower chamber with phosphomimetic mutant vs non-phosphorylatable and wild-type	Tonucci et al., 2019)
• PKA activity gradients detected, where PKA microdomains were detected at the leading edge that were not present at the lagging edge, seemingly validating earlier findings linking PKA action with increases in cell migration • Presence of puncta, of a 250nm diameter, on the basal membrane with high PKA activity was also detected indicating signalling compartmentalisation • Elevated PKA activity detected within filopodia in comparison to the basal membrane in harmony with previous studies which showed that a pool of PKA molecules, integrin anchored type I PKA, was active at the tip of migrating cells	Mo, 2017
• Transfection of cells with Rac1 and Cdc42 followed by treatment of mouse embryonic stem cells (mESCs) with cAMP analogue 8-Bromo cAMP for four hours was found to significantly increase Arp3, TOCA, PAK and N-WASP protein expression	Kim et al., 2015

• Activation of Rac and Cdc42 upon application of cAMP increased MLCK expression and MLC phosphorylation which is known to induce filament contraction at the leading edge • Correlation of Rac activation with PKA signalling, via cAMP, in carcinoma	O'Connor and Mercurio, 2001

Table 2- Evidence Against the Role of cAMP in Decreasing Cell Migration via Regulation of the Actin Cytoskeleton

Evidence	***Reference***
• Bladder cancer cells overexpressing Epac1 showed decreased and slower migration • Wound healing assay and subsequent phase contrast micrographs exhibited decreased invasion in cell lines where Epac1 was overexpressed and implicated Epac1 localisation at the plasma membrane • Epac1 could mediate its action via Rap1 regulation of E-cadherin	Ichikawa et al., 2018
• PKA inhibits RhoA signalling via phosphorylation at Ser188 to creating a stable RhoA-GDP-RhoGDIa complex and stimulates RhoA sequestration to the cytosol • This decreases actin protrusion formation and stimulates cell rounding	Oishi et al., 2012 Dong et al., 1998

1.3 Tools for Measuring cAMP Gradients Within Membrane-Based Actin Protrusions

1.31 Drosophila melanogaster as a Model System for Studying cAMP Signalling Within Actin-Based Protrusions

Drosophila melanogaster has a long association as a model organism for the advancement of knowledge in a wide variety of cellular and genetic processes, not limited to cell signalling cascades, developmental biology and gene regulation(Langenhan et al., 2015). Not only is *Drosophila* relatively cheap and easy to maintain, it also possesses a short life cycle therefore rendering it unnecessary to wait months to undertake an experiment(ref). Furthermore, *Drosophila* has been deemed a partial replacement by National Centre for the Replacement, Refinement and Reduction of Animals in Research due to its limited ability to perceive pain, making it a more humane choice for the researcher. Furthermore, many tools have been developed for use in *Drosophila;* not only do they facilitate transgene expression and RNA interference, but the development of genetically encoded biosensors has greatly advanced the understanding cell signalling pathways(Couto et al., 2017, Maiellaro et al., 2016). For example, the Gal4UAS system allows a target gene to be expressed exclusively within cells of a particular tissue, such as sensory organ precursor (SOP) cells of the notum(Brand and Perrimon, 1993). Additionally, the FLP/FRT system facilitates site-specific recombination to produce homozygous mutant or homozygous wild-type daughter cells(Lee and Luo, 2001). The MARCM system combines the Gal4-UAS system with the FLP/FRT system to produce a mosaic of cells within a particular tissue, some of which are homozygous for the transgene and some of which are wild-type. This tool-box of sophistic genetic techniques makes *Drosophila* an attractive model organism which can be used to study a wide range of processes.

The notum of *Drosophila melanogaster* pupae has been successfully employed as a model system to study actin-based protrusions within a polarised epithelium, enabling real-time measurements to be taken in a live animal(Georgiou and Baum, 2010, Cohen et al., 2010, Couto et al., 2017, Canales Coutiño et al., 2020, Canales Coutiño et al., 2021). The notum of *Drosophila* consists of an ordered epithelium which develops during pupae maturation during thorax closure. The process of thorax closure involves the attachment at the midline of the notum of two lateral epithelial sheets(Zeitlinger and Bohmann, 1999). Epithelial cells within the *Drosophila* notum possess distinct apical and basal domains, characterised by the existence of actin-based membrane protrusions(Georgiou and Baum, 2010, Couto et al., 2017). These include microvilli-like protrusions (found at 1-2μm below the cuticle), intermediate lateral protrusions (3-6μm below the cell apex) and basal protrusions (found from 7μm and further below the apex), such as filopodia and lamellipodia(Couto et al., 2017) (figure-5). Microvilli are characterised by short microvillus-like structures distributed around the cell in the x-axis, serving to increase the cell surface area(Georgiou and Baum, 2010). Lateral intermediate protrusions fall below the adherens junction and form finger-like extensions in the x-axis, which extend several micrometres through the z-axis, giving them a sheet-like appearance(Couto et al., 2017). Within the basal domain, dynamic filopodia and lamellipodia can also be detected(Georgiou and Baum, 2010). The Georgiou lab has previously demonstrated that epithelial cells within the notum of *Drosophila melanogaster* can be used as a model system to study the spatiotemporal regulation of key components contributing to the appropriate regulation of the actin cytoskeleton(Georgiou and Baum, 2010, Cohen et al., 2010, Couto et al., 2017).

Moreover, over 200 GPCRs have been identified in the *Drosophila* genome, over half of which are orphan. The presence of G proteins has also been characterised within the genome; nine genes in total

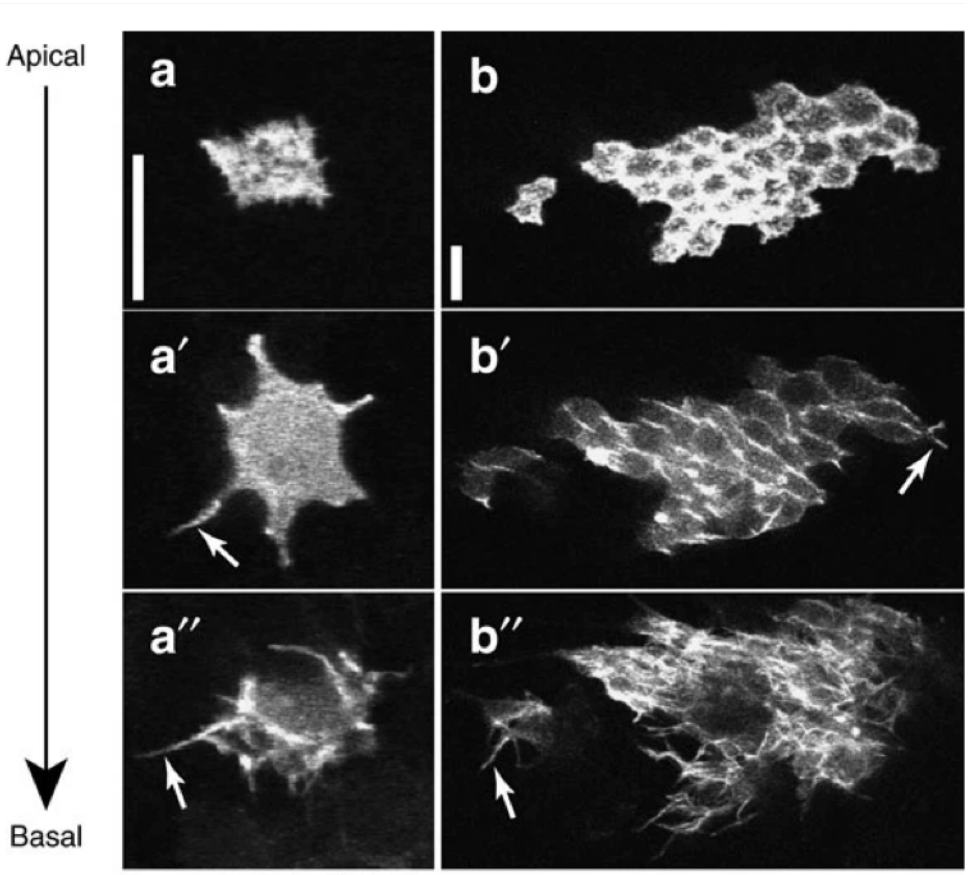

Figure 5- The distribution of actin-based membrane protrusions throughout epithelial cells of Drosophila melanogaster at different cell depths. *Microvilli-like protrusions are detected at the cell apex (a, b), thin intermediate-lateral protrusions within the intermediate region (a'b') and long, dynamic filopodia within the basal region (a"b"). Panel a shows protrusion form in Neu-GFP-Moe^{+} (expression driven by the GAL4-UAS system), whereas panel b displays protrusion form in GFP-Moe-Pnr^{+} clones (expression driven by the FLP/FRT/MARCM system). Figure adapted from Couto et al. 2017*

encoding Gα proteins (6 genes characterised, 3 uncharacterised), Gβ proteins (3 genes) and Gγ proteins(Hanlon and Andrew, 2015). Two Gα subunits (Gαi and Gαo) were found to inhibit ACs to decrease cAMP concentration within the embryonic brain, embryonic midgut, embryonic dorsal vessel and maxillary palpus among other locations(Hanlon and Andrew, 2015). Two Gαs subunits are encoded and expressed within the adult brain cell body, with ubiquitous expression in the early embryo and within the maxillary palpus. For example, the *Drosophila* GPCR Tre1 was shown to affect Rho1 and E-cadherin (Shotgun) within germ cells, enacting signalling through the Gαo subunit and Pins (a GDI), although a putative mechanism remains unknown(Kamps et al., 2010). Therefore, this presents a relatively simple system which is attractive

for studying GPCR and cAMP dynamics. Additionally, given that so many GPCRs are orphan and the role of said receptors within embryogenesis and pupal development are mostly uncharacterised, the field is open to new discoveries. Furthermore, orthologues of genes encoding core components of the cAMP signalling pathway are also present in *Drosophila* (table-3), therefore *Drosophila* is an ideal system to study cAMP signalling.

Table 3- Drosophila melanogaster orthologues of key components of the cAMP signalling pathway

***Drosophila melanogaster* Orthologue**	**cAMP Signalling Pathway Component**	**Functions**
Rutabaga	AC	Neurotransmitter signalling
Dunce	PDE	Learning
Pka-C1	PKA	Segment polarity, learning, oogenesis
AKAP-200	AKAP	Oogenesis
Cyclic-AMP Response Element Binding Protein (CREB) B	CREB	Memory, photoperiod response
Epac	Epac	Aversive odor learning, Malphigian tubule secretion
GPCR Kinase 2	GPCR Kinase	Oogenesis, learning
Radish	Rap-like GTPase activator activity	Anaesthesia-resistant memory, olfactory learning

1.32 Förster Resonance Energy Transfer (FRET)

FRET is a distance-dependent energy transfer process, whereby energy is transferred from a donor fluorochromophore to an acceptor fluorochromophore in a non-radiative manner. Initially proposed by Förster in a seminal paper during the late 1940s, it is dependent on three conditions: (1) the donor and acceptor fluorochromophores must be sufficiently proximal to each other (within nanometre range); (2) the emission of the donor must sufficiently overlap with acceptor excitation; (3) the acceptor transition dipole must not be perpendicular to the electric field of the donor dipole (the donor and acceptor must be in the correct orientation)(Forster, 1946, Algar et al., 2019) (figure-6).

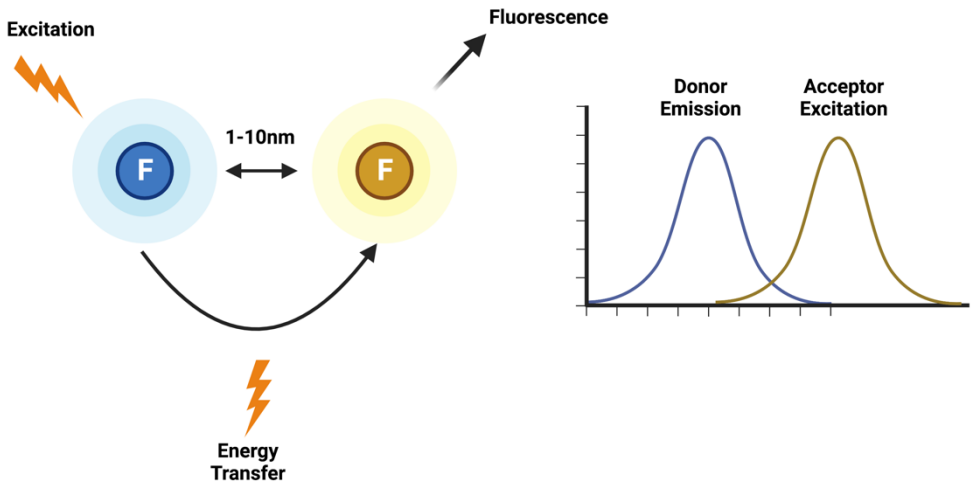

Figure 6- The process of Förster Resonance Energy Transfer. *The donor (blue F) is excited and transfers its energy to the acceptor (yellow F). The donor and acceptor must be 1-10nm away from each other, and donor emission must overlap with acceptor excitation to satisfy the conditions of a FRET reaction.*

Following excitation of the donor fluorochromophore at one wavelength, energy is transferred, via dipole-dipole coupling, from the donor to the acceptor(Algar et al., 2019). The acceptor fluorochromophore quenches donor fluorescence and itself becomes excited. Thus, an increase in the fluorescence emission of the acceptor is observed, termed sensitised emission. FRET energy transfer cannot be directly

measured- the non-radiative energy transfer is a dark process, therefore FRET efficiency is measured indirectly by recording alterations in donor or acceptor photophysical characteristics(Komatsu et al., 2011). For example, following energy transfer from the donor fluorochromophore to the acceptor fluorochromophore, a decrease in donor fluorescence intensity is observed, followed closely by an increase in acceptor fluorescence sensitised emission(Börner et al., 2011). In this way, quantitative intensity-based FRET measurements can be recorded by monitoring the ratio of acceptor sensitised emission to donor excitation (acceptor:donor), dubbed ratiometric FRET.

Although, this method is problematic in cases where a sample contains different quantities of donor fluorochromophore in comparison to acceptor fluorochromophore (i.e. during intermolecular FRET experiments), this method is well suited to experiments involving genetically encoded FRET biosensors(Robichaux and Cheng, 2018). In such experiments, the ratio of donor fluorochromophore to acceptor fluorochromophore is fixed, providing certainty that differences in FRET ratio are not due to inter-sample variability of donor and or acceptor concentration. This enables the generation of more accurate FRET ratios, albeit ratios can require extensive corrections for photobleaching and spectral bleedthrough(Börner et al., 2011). Additionally, image processing can be long and complex, requiring multiple steps and image thresholding(Robichaux and Cheng, 2018). FRET biosensors permit fast and dynamic intracellular measurements to be undertaken; ideal for revealing the fast-changing spatiotemporal complexities characteristic of signalling pathways. Furthermore, experiments can be undertaken using a widefield epifluorescent microscope, increasing accessibility, although confocal microscopy can be employed to obtain higher spatial resolutions(Willoughby and Cooper, 2008).

1.33 cAMP FRET Biosensors

We engaged a cytosolic Epac-based genetically encoded cAMP FRET sensor. Further information regarding the development and properties of the sensor can be found in the references(Maiellaro et al., 2016, Nikolaev et al., 2004). Add the other refs too. The sensor was composed of the cAMP binding site from Epac1, sandwiched by a fluorophore on either side (YFP and CFP) (figure-7). In states of low cAMP, YFP and CFP are in close proximity thus energy transfer from CFP to YFP is increased. This leads to an increase in YFP sensitised emission and a corresponding decrease in CFP emission, thus generating a high FRET ratio (where ratio is calculated by YFP/CFP). In conditions of high cAMP, cAMP binding to the Epac-1 cAMP binding domain induces a conformational change in the sensor structure, pushing YFP and CFP further apart(Börner et al., 2011). Consequently, there is a corresponding decrease in YFP sensitised emission and increase in CFP emission, counterintuitively generating a low FRET ratio (where ratio is calculated by YFP/CFP).

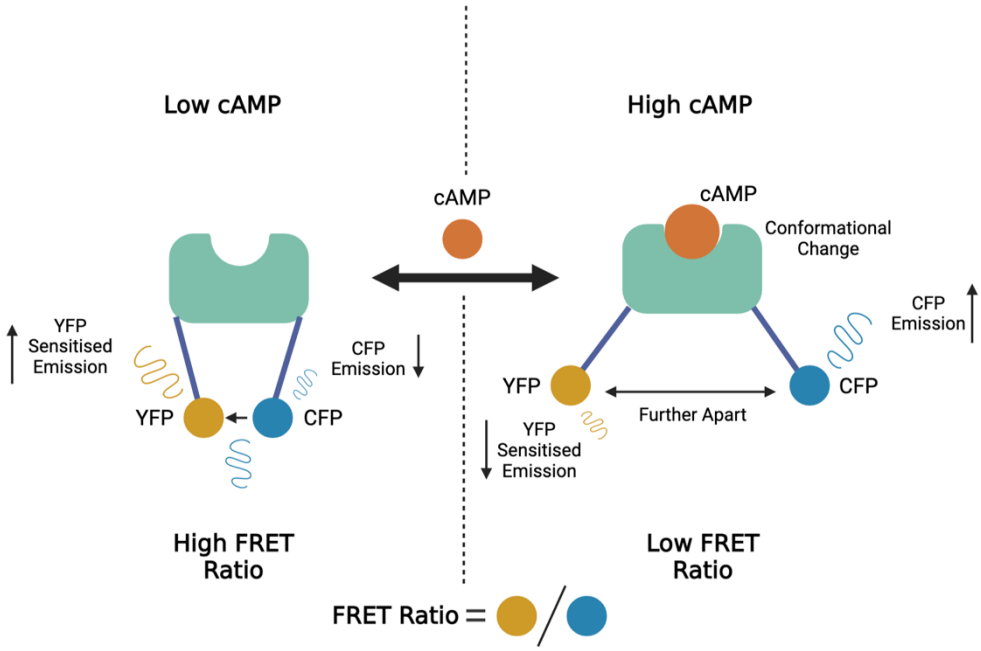

Figure 7- The mechanism of action of the Epac1 cAMP sensor. *Binding of cAMP induces a conformational change pushing the fluorophores YFP and CFP further apart. This increases CFP emission while decreasing YFP sensitised emission, thus a lower ratio is recorded. Where cAMP is not bound, the fluorophores CFP and YFP are closer together. Therefore, there is increased energy transfer from CFP to YFP, increasing YFP sensitised emission and decreasing CFP emission so a higher FRET ratio is recorded.*

1.34 A Genetically Encoded FLINC-Based PKA Sensor

Also available for use, was a sensor to detect PKA using pcSOFI (Photoconversion Soichastic Optical Fluorescent), a superesolution microscopy technique, to quantify PKA distribution within the cell. The pcSOFI technique generates images with a greater resolution than normal microscopy techniques, such as wide-field epifluorescent microscopy or confocal microscopy, the resolution of which is limited by the point spread function(Moeyaert and Dedecker, 2014). The use of reversibly switchable fluorescent proteins (RSFP), which continuously cycle between a bright and dime fluorescent state upon irradiation, are an important tool in the arsenal of acquisition in pcSOFI. The 'flickering' property of RSFPs upon low doses of selective irradiation, means only some molecules are within the 'bright' state and other molecules are within the 'dim' state. Molecules within the 'dim' state do not contribute to the overall fluorescence of the sample at the moment of irradiation, thus the PSF is decreased and resolution increased. Following repeated irradiation, cumulative analysis can be employed to isolate the contribution of each molecule as the fluctuations (i.e. the rate of cycling between 'dim' and 'bright' states) are independent for each molecule, therefore it is possible to identify each molecule contribution. Not only does pcSOFI generate fast, 3D images, it also provides high spatiotemporal resolution making it perfect for investigating the spatiotemporal regulation of cell signalling cascades.

The PKA sensor relies on the principal of Fluorescence Fluctuation Increases by Contrast (FLINC), whereby the proximity of two RSFPs can affect their blinking behaviour (figure-8). Upon PKA binding to the FHA1 domain of AKAR, it phosphorylates the PKA-specific phosphorylatable peptide sequence bringing the RSFPs Dropna and Tag-RFP-T in closer proximity(Mo et al., 2017). Dropna binding to Tag-RFP-T induces an alteration in the blinking behaviour of Tag-RFP-T in which it undergoes dark state conversion at a 25% faster rate(Mo et al.,

2017). These alterations in blinking behaviour can be analysed and extracted by cumulative analysis, providing spatiotemporal information regarding spatiotemporal PKA localisation within the cell.

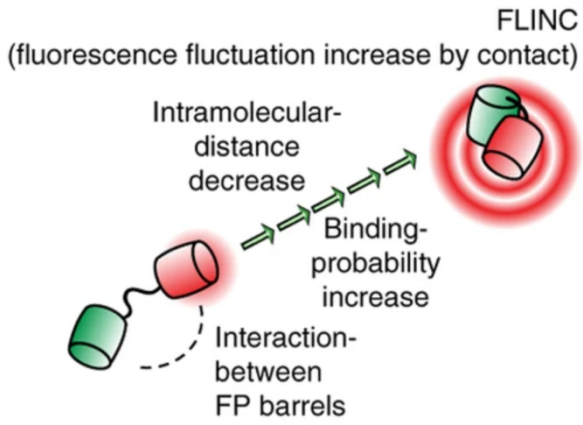

Figure 8- The process of FLINC. *Bind of PKA induces a phosphorylation event which brings FP barrels closer together, altering the flickering behaviour of Tag-RFP. Figure from (Mo et al., 2017)*

1.4 Experimental Aims

In order to quantify spatiotemporal differences in subcellular cAMP concentration, we took advantage of a cytosolic genetically encoded cAMP FRET biosensor(Börner et al., 2011, Maiellaro et al., 2016). Previous work in the Georgiou lab showed that a cytosolic genetically encoded FRET biosensor for Rac could be expressed within membrane-based actin protrusions in well-spaced epithelial cells and epithelial cell clones. Therefore, using the Gal4-UAS and the MARCM systems, cAMP sensor expression was driven well-spaced SOP cells or epithelial cell clones, homozygous for sensor expression within the notum of *Drosophila melanogaster.* Using the tissue-specific promoter Neuralized, sensor expression can be driven to well-spaced SOP cells, where sensor expression can be detected within actin membrane-based protrusions in real-time at high spatial resolutions within the cell(Georgiou and Baum, 2010, Couto et al., 2017, Furman and Bukharina, 2008). Furthermore, as SOP cells are imaged between 14 and 16 hours before they commit to a precursor fate, they are representative of all epithelial cells(Cohen et al., 2010). Unobstructed actin-membrane based protrusions containing the sensor can also be visualised within homozygous clones using the tissue-specific promoter Pannier. This permits visualisation of cAMP gradients and compartmentalisation within a complex, physiologically relevant cellular environment of the live animal *Drosophila melanogaster*.

The aim of this project was to establish and optimise a protocol for the study of cAMP gradients within actin-based membrane protrusions. Using confocal microscopy, we measured 3D cAMP gradients at high spatial resolution within actin-based protrusions via sensitised emission FRET. This allowed us to quantify local cAMP compartmentalisation within actin-based protrusions, to permit investigation of wild-type cAMP gradients.

Chapter 2: General Methods

2.1 Materials

2.11 Genetic Constructs, Balancers and Phenotypic Markers

Chromosome balancers possess multiple chromosome inversions which prevent homologous recombination by averting crossing over. Unbalanced cross-over can occur, but offspring are not viable as they lack some genes and may carry multiple copies of others. Thus, chromosome balancers are homozygous lethal and are useful to maintain the presence of genes of interest they balance. Furthermore, the presence of dominant phenotypic markers for genes of interest facilitates easy selection of pupae and adult flies containing these genes for experiments and genetic crosses. The phenotypic markers and chromosome balancers utilised are listed in Table-4 and genetic constructs within the genome of *Drosophila melanogaster* are listed in Table-5.

Table 4- Drosophila melanogaster balancers and phenotypic markers

Abbreviation	*Chromosome*	*Type*	*Phenotype*
TM6b	3	Balancer	Tubby (see below) and Stubble (see below)
Ry (Rosy)	3	Marker	Compound red/brown eyes
MKRS	3	Marker	Dominant stubble (see below), recessive rosy eyes (see above)
Tb (Tubby)	3	Marker	Pupae, larvae and adults possess short and rounded body

W[1118] (White)	1	Marker	Compound white eyes
Hu (Humeral)	3	Marker	Additional 3-6 macrochaetes which can be shorter in length
Sb (Stubble)	3	Marker	Shortened, wider bristles
IF (Irregular Facets)	2	Marker	Small, narrowed oblong eyes, irregular interommatidial bristle pattern, irregular individual facets within dorsal eye, facets absent or fused in the middle and ventral eye
Cyo-GFP (Curly of Oster)	2	Marker	Wing is curled upwards (most pronounced at 25ºC), full body GFP expression
W[+]	3	Marker	Non-mutated version of the *white* gene, gene rescue

Table 5- A table explaining the different genetic constructs and their functions employed in this study

Genetic Construct	*Function*
Neu-GAL4	The tissue specific promoter Neuralized drives GAL4 expression to well-spaced SOP cells within the notum
Pnr-GAL4	Tissue specific promoter Pannier drives GAL4 expression to a central strip of epithelial cells within the notum
Ubx-Flp	The promoter Ultrabithorax drives flippase expression to the notum

FRT40A	Flippase recognition site at position 40A on the chromosome, the site at which post-mitotic recombination is stimulated
Tub-GAL-80	Repressible cell marker GAL80 under the control of the tubulin promoter, inducing ubiquitous GAL80 expression to suppress GAL4 activity
UAS-epac1(camps)	cAMP FRET biosensor under the control of the UAS (Upstream Activation Sequence)
UAS-GFP-Moe	Moesin is the actin-binding domain which targets GFP expression to filamentous actin under the control of the UAS
UAS-GFP-Pon	Pon is the membrane localisation domain of *Drosophila melanogaster* and targets GFP expression to the plasma membrane, under the control of the UAS

2.12 *Drosophila melanogaster* Lines and Crosses

The *Drosophila* lines used in this study are listed in table-6.

Table 6- Drosophila melanogaster line genotypes

Line Name	*Drosophila melanogaster* Genotypes	*Source*
M50	w;;P[ry,Gal4][neu]/TM6b,Hu	Georgiou Lab
M361	w;IF/CyoGFP;NeuGal4/TM6b, Tb, Hu	Georgiou Lab
M595	;;PnrGal4/TM6b	Georgiou Lab
M370	w; Tub-Gal80, FRT40A; MKRS/TM6b	Georgiou Lab
M539	Ubx-flp; FRT40A/CyO-GFP; PnrGAL4/TM6b	Georgiou Lab
M287	w;;Pnr-UAS-MoeGFP/TM6b	Georgiou Lab

M60	P[mw,Gal4][neu], P[mw,UAS-Moe-GFP] / TM6b	Georgiou Lab
C19	w [1118];;*	Bloomington Stock Repository
RJK141	w[118];+;P(UAS-epac1(camps)w[+])/Sb	Maiellaro Lab
FLINC	;UAS-FLINC(PKA)/SM6a;	Maiellaro Lab

2.2 Methods

2.21 *Drosophila melanogaster* Husbandry

All lines (table-6) were housed in 25 mL plastic tubes, containing standard fly food (see

2.22 *Drosophila melanogaster* Food Recipe). Stocks maintained at 25ºC were flipped (transferred to new food) once a week and stocks housed at 18ºC were flipped once every two weeks. Crosses were exclusively maintained at 25ºC and flipped three times per week, so as to ensure a continuous supply of pupae for experiments.

In order to undertake virgin collections and establish crosses, flies were anaesthetised via a porous CO_2 polyethylene gas diffuser and observed under a Leica M60 stereomicroscope. Virgin female flies were collected every eight hours if kept at 25ºC and every sixteen hours if housed at 18 ºC, following emptying of the tube at hour zero, as females do not reach sexual maturity for eight hours therefore do not mate during this time. Flies were screened to select for or against the relevant phenotypic markers and balancers in order to ensure progeny possessed the desired genotype. Crosses were subsequently established using thirty virgin females and ten newly-hatched males.

2.22 *Drosophila melanogaster* Food Recipe

Standard fly food was prepared using the following recipe (makes 1 litre):

0.5 litres warm water, 125 millilitres cold water, 70.63g golden syrup, 15.88g yeast pellets, 9.13g soya flour, 67.00g cornmeal, 5.25g agar and 4.43g of Propionic acid. 5 millilitres of nipagin was added to food prepared for general lines whereas this ingredient was omitted when preparing food for crosses, as nipagin (an antimicrobial agent) can negatively affect *Drosophila melanogaster* growth. Food was stored at 18ºC for up to three weeks.

2.23 *Drosophila melanogaster* Crosses

2.231 Production of Non-Tubby Pupae Containing Well-Spaced Cells Labelled With GFP-Moe

Stocks of the genotype Neu-Gal4-UAS-Moe-GFP and Pnr-Gal4-UAS-Moe-GFP both contained the tubby balancer which affects development of the notum. The *tubby* gene is implicated in chitin-based cuticle development, body morphogenesis and is expressed, among other places, in the dorsal epidermis. The effects of this gene on notum development are uncharacterised, therefore crosses were established to remove the TM6b balancer, which generates a tubby phenotype. This allowed imaging of wild-type epithelial cells, labelled by *moe*-GFP, to visualise wild-type actin protrusions as a comparison for cells expressing the FRET cAMP biosensor. Virgin *pnr-moe*-GFP^{+} females were crossed with wild-type males to produce tubby-free flies (figure-9). This cross was not undertaken with *neu-moe*-GFP^{+} flies as it was found that they no longer possessed the tubby phenotypic marker but did possess the humeral marker characteristic of TM6b, therefore we could confirm presence of the genes of interest *neu-moe*-GFP.

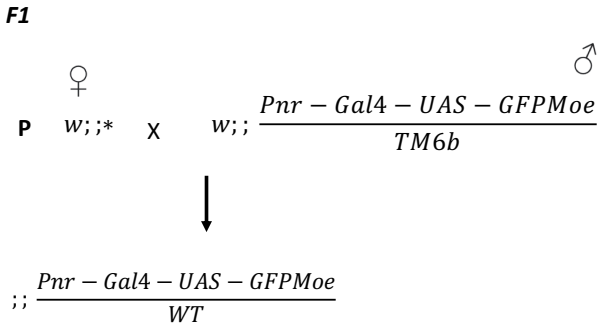

Figure 9- The Tubby balancer was removed from Pnr-GFP-Moe^{+} flies to enable imaging. *Tubby flies were selected against.*

2.232 Generation of Well-Spaced neuralized-Positive Cells Expressing the cAMP FRET Biosensor

To generate flies expressing the cAMP FRET sensor within well-spaced epithelial cells in the notum, thirty *neu*-Gal4^{+} virgin females were crossed with ten UAS-*epac1(camps)*$^{+}$ males(figure-10).

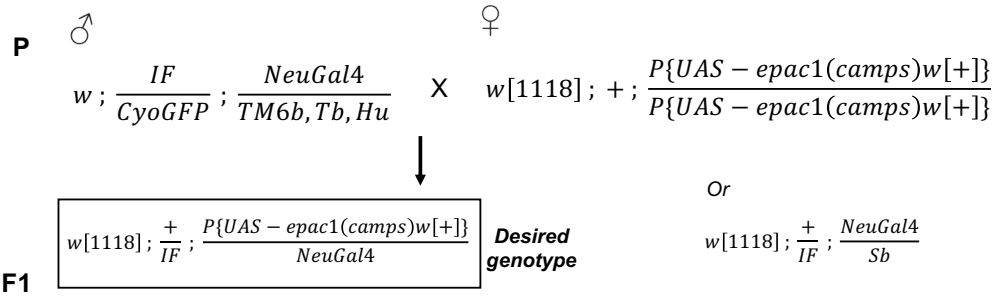

Figure 10- Generation of neu-Gal4-UAS-epac1 (camps) flies. *Virgin female flies containing neu-Gal4 on the third chromosome were mated with male flies containing UAS-epac1(camps) also on the third chromosome. Tubby (Tb) flies were selected against, pupae expressing fluorescent salivary glands were selected for experiments..*

2.233 Generation of a Central Strip of Cells Expressing the cAMP FRET Biosensor

In order to produce flies expressing the cAMP FRET sensor within all epithelial cells in the notum, *pnr*-Gal4^{+} virgin females were crossed with UAS-*epac1(camps)*$^{+}$ males (figure-11).

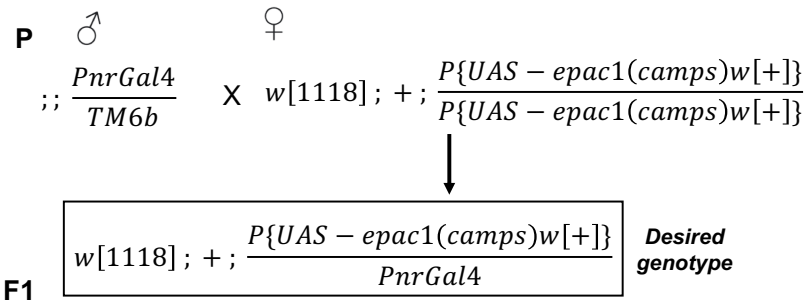

Figure 11- Generation of pnr-Gal4-UAS-epac1 (camps) flies. *Virgin female flies containing pnr-Gal4 on the third chromosome were mated with male flies containing UAS-epac1(camps) also on the third chromosome. Tubby flies were selected against, pupae expressing fluorescence in two dots in the position of the salivary glands were selected for experiments.*

2.234 Producing Homozygous Clones Containing the cAMP FRET Biosensor Using the MARCM System

To obtain flies expressing the cAMP FRET sensor in patches of epithelial cell clones within the notum, virgin female *tub-Gal80,FRT40A*$^{+}$ flies were crossed with UAS-*epac1(camps)*$^{+}$ males (line name RJK141). Male progenies from this cross, with a wild-type stubble phenotype, were further crossed with *pnr*-Gal4^{+} virgin females to produce a mosaic of sensor expression and wild-type cells within a central strip in the notum (figure-12, figure-13). Both male and female pupae were used in all experiments.

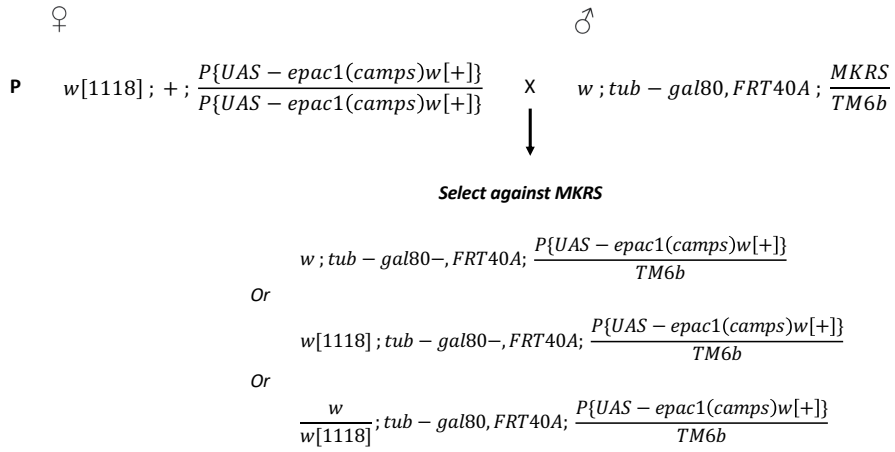

Figure 12- The F1 cross to generate Tub-Gal80-FRT40A⁺ flies. *UAS-camps(epac1)⁺ flies were crossed with Tub-Gal80-FRT40A⁺ flies, MKRS was selected against and TM6b was selected for.*

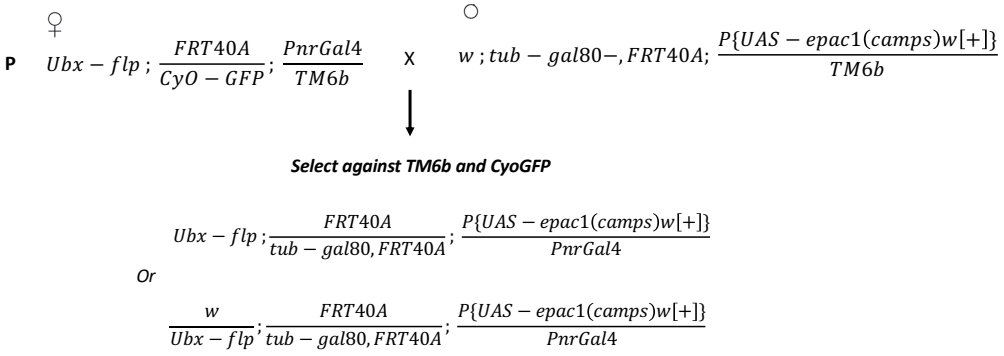

Figure 13- The F2 cross to generate Ubx-flp-TubGal80-FRT40A-UAS-epac1(camps)⁺ flies. *TubGal80,FRT40A-UAS-camps(epac1) flies were used from the F1 cross. TM6b and CyoGFP were selected against, flies with two fluorescent dots at the location of the salivary galnds were used for experiments.*

2.235 Production of Well-Spaced neu-flinc(pka)⁺ Cells and pnr-flinc(pka)⁺ Clones

To generate flies expressing the FLINC-PKA sensor in well-spaced SOP cells, thirty neu-*gal4*⁺ flies were crossed with ten uas-*flinc(pka)* male flies (figure-14). In order to produce a field of epithelial cells within the notum expressing the FLINC-PKA sensor, thirty pnr-*gal4*⁺ flies were crossed with ten uas-*flinc(pka)* flies (figure-15).

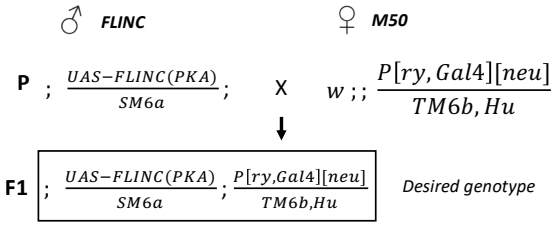

Figure 14- The generation of neu-FLINC⁺ flies. *Flies with fluorescent salivary glands were selected for.*

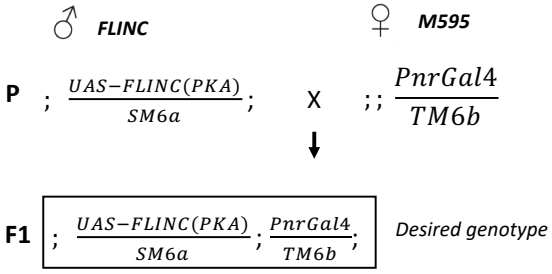

Figure 15- The generation of Pnr-FLINC⁺ flies. *Flies containing two fluorescent dots at the location of the salivary glands were selected for and used in experiments.*

2.24 *Drosophila melanogaster* Pupae Collection and Incubation

White pupae (0 hours APF- After Pupae Formation) were collected from the sides of the plastic tubes of crosses, transferred to a petri dish and their fluorescence assessed using a Leica MZ10F Fluorescence Stereomicroscope. The petri dish was lined using a piece of tissue paper and distilled water was applied (before pupae transfer), with excess water tipped away, to prevent pupae desiccation. Pupae were illuminated with a CoolLED PE-300 in combination with a GFP filter, as no filter was available for YFP or CFP and fluorescence was still visible due to wavelength overlap between YFP and GFP fluorophores. Fluorescent salivary glands were selected for in pupae containing Neuralized *neu*-Gal4 x UAS-*epac1(camps).* whereas two small dots on either side, at the top of the salivary glands, were selected for in Pannier crosses *pnr*-Gal4 x UAS-*epac1(camps).* Pupae containing the promoter Neuralized were incubated at 25ºC for 14.75 hours whereas pupae containing the promoter Pannier were incubated at 29ºC for 18 hours. All pupae were mounted twenty minutes before experiment initiation and remained at RT (Room Temperature) for this duration.

2.3 Confocal Microscopy

2.31 Pupae Mounting

Pupae were mounted ventral side down on 76 x 26 mm microscope slides (Fisher Scientific) with a bridge created using four 22 x 22 mm, 0.13-0.17 mm thick cover slips (Fisher Scientific), although bridge height was adjusted to accommodate different pupae sizes. The notum was exposed by peeling a section of the pupal casing covering the notum, using tungsten forceps. A 22 x 50 mm 0.16-0.19 mm coverslip (Fisher Scientific) coated in a thin layer of 10S VOLTALEF injection oil (VWR UK) was placed atop the slide to create an oil interface between the notum and coverslip for imaging. Images were acquired from top to bottom using the ZEISS880 Confocal Microscope using the X40 oil lens or widefield epifluorescence microscope (as specified). Further details of the protocol can be found in publications from the Georgiou lab(Canales Coutiño et al., 2021).

2.32 Visualisation of GFP Via Confocal Microscopy

2.321 General Protocol

All GFP-images were acquired via the ZEISS880 Confocal Microscope. GFP was detected in the second channels using a GAsP detector photomultiplier tube, to compensate for low signal, between 503 and 533 nm. A 488 laser was utilised at laser power 2.1, with the corresponding 488 beam-splitter. 16-bit images were obtained with a 1024 by 1024 frame size (image size 354.25 x 354.25 µm and a 1AU pinhole, a compromise between file-size and signal to noise ratio. Gain was adjusted to optimise visualisation for each sample, but ranged from 500 to 700 and all images were acquired at speed six, with a 2.06 µsec pixel dwell time. Epithelial cells were first located using the HXP 120V lamp using the FSet38 filter set (green light), before switching to the 488 laser.

2.322 GFP Z-Stacks

Z-stacks were acquired from cuticle to basal region at a 2 times optical zoom to generate 1µm slices. Tile-scans were also acquired, image size is indicated in the specific figure legends.

2.33 Acquisition of Sensitised Emission FRET Z-Stacks

Sensitised emission FRET experiments were undertaken on the ZEISS 880 Confocal Microscope (table-7,8). Cells were first located using the HXP 120V lamp in combination with the FSet38 green filter, due to wavelength overlap between YFP and GFP (no YFP or CFP filters were available for use with the HXP120V lamp). Cells were located in the Zen 'Live' tab using the YFP only laser, so as not to induce photobleaching of the CFP fluorophore which could affect energy transfer to YFP upon alterations in cAMP concentration. A two-times optical zoom was adopted upon identifying a cell of interest in order to magnify and visualise single cells rather than the whole field of view; cells selected were of equal brightness so as to exclude different concentrations of sensor as a variable affecting alterations in FRET ratio(Börner et al., 2011). A Z-stack, obtained from cell apex to the basal region, producing two images, CFP emission and YFP sensitised emission (figure-16).

Table 7- Sensitised emission FRET configuration using the ZEISS 880 Confocal Microscope

Track Number	*Track*	*Channel*	*Measurements*	*Parameters*
1	**CFP Only** *Laser 405nm*	1	CFP excitation CFP emission	Wl 415-495nm
2	**YFP Only** *Laser 514nm*	2 (GAsP Detector)	YFP excitation YFP emission	Wl 518-621nm
3	**FRET**	Channel 1 CFP	CFP emission	Wl 415-495nm

Laser 405nm	Channel 2 YFP	YFP sensitised emission	WI 518-621nm

Table 8- General settings and parameters as configured for undertaking sensitised emission FRET using the ZEISS 880 Confocal Microscope

General Settings

Setting	**Parameter**	**Justification**
Gain	CFP 670	Optimised gain for samples
	YFP 500	Optimised gain for samples
Laser Power	CFP 2.5	Optimised gain to obtain sufficient signal without photobleaching the sample
	YFP 2.6	Optimised gain to obtain sufficient signal without photobleaching the sample
Channel	YFP 2	Sensitive GAsP detector employing a photomultiplier tube to increase signal detected
	CFP 1	
Frame Size	512 x 512	Optimised to increase number of photons
Bit Depth	16 bit	Each pixel is assigned a value, in binary format, corresponding to the light emitted by the sample. Bit depth refers to the amount of possible values available for each pixel. 16-bit images were acquired over 8-bit images as a greater number of possible values are available for each pixel in 16-bit images (65536 values) vs 8 bit images (254 values) increasing accuracy of measurements.
Pinhole	1 AU	The process of excluding emitted light to resolve focal planes within a thick

		sample to produce good quality images is called optical sectioning. This is, in part, controlled by the pinhole size i.e. the diameter of the hole (aperture) through which emitted light from the sample passes to reach the detector. If a pinhole is too small, too little light (signal) reaches the detector decreasing accuracy. However, if a large pinhole is employed too much out of plane light (noise) reaches the detector meaning optical sections within the sample cannot be obtained. Therefore, this pinhole size was a compromise between optical sectioning and SNR.
Speed	3	The time taken to scan the sample. A slower scan speed improves SNR as each pixel is scanned for longer, increasing the amount of signal detected. Lower speeds were used to increase the number of photons (light/signal) reaching the detector, due to low SNR experienced within samples
Averaging	2	Each line is scanned twice and the pixel values averaged to increase accuracy of the pixel values collected within the image.
Pixel Dwell	32.97 µsec	The length of time spent scanning each pixel. Longer pixel dwell times increases the amount of signal detected for each pixel.
Scan Time	40.51 sec	Longer scan times, achieved by increasing pixel dwell times (by

		decreasing the scan speed), increase the amount of signal detected.
Beam Splitter (Visible Light)	458/514	Beam splitter for YFP
Beam Splitter (Invisible Light)	405	Beam splitter for CFP

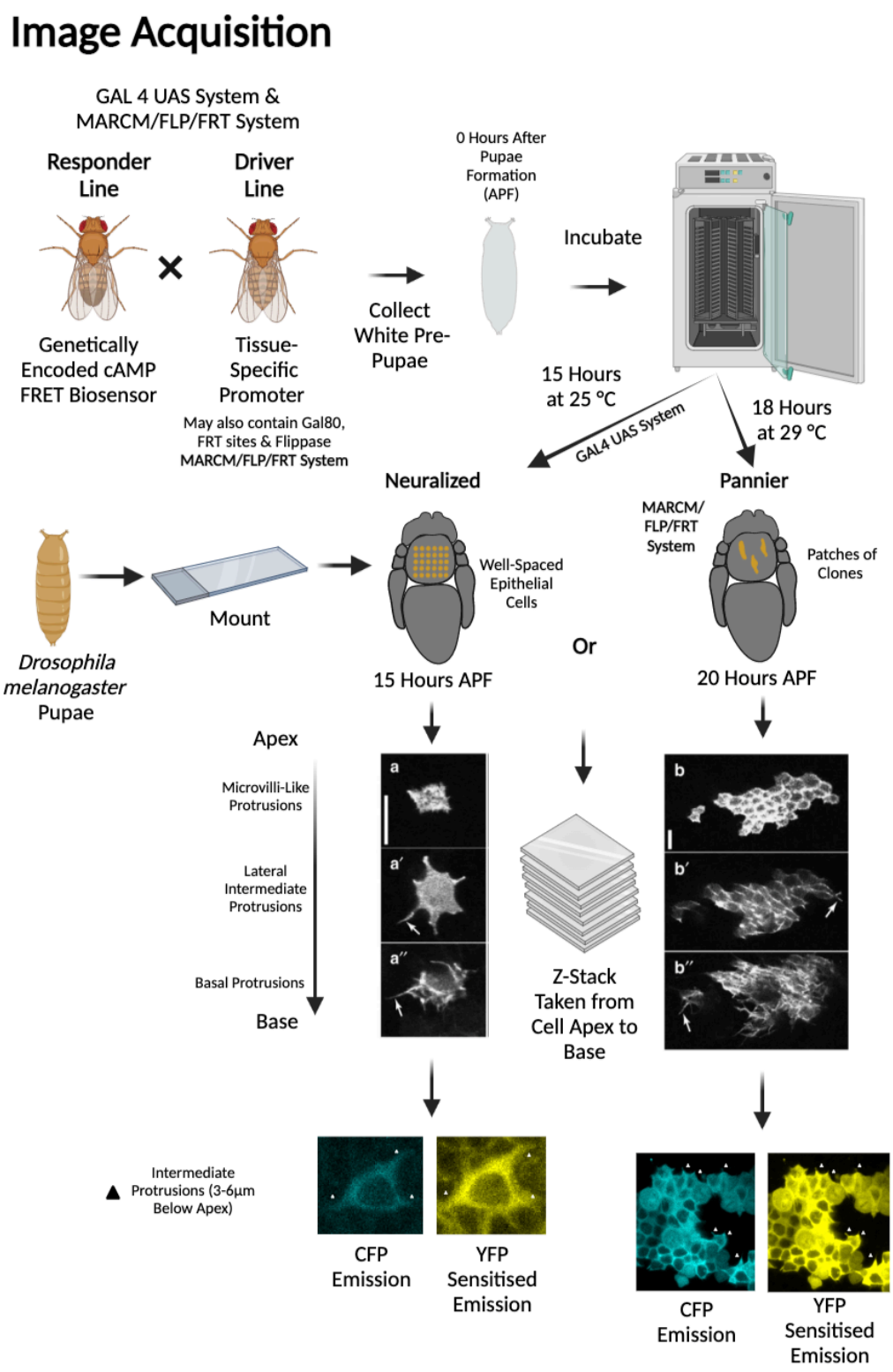

Figure 16- The sensitised emission FRET confocal microscopy workflow. *Flies containing the genetically encoded cAMP FRET sensor under the control of the UAS were crossed with flies containing a tissue specific promoter to induce sensor expression within epithelial cells of interest in the notum of the fly. White pupae were collected and aged at either at 25 degrees (for promoter Neuralized) or 29 degrees (promoter Pannier). Aged pupae were mounted for confocal imaging during which Z-stacks were taken from cell apex to base, recording CFP emission and YFP sensitised emission.*

2.34 Preliminary Acceptor Photobleaching

The confocal microscopy acquisition settings (table-9), both for generic 'before' acceptor photobleaching experiments (table-10) and specific settings associated with acceptor photobleaching (table-11) are listed below.

Table 9- Confocal microscopy protocol used for acceptor photobleaching experiments

Track Number	*Track*	*Channel*	*Measurements*	*Parameters*
1	**CFP Only** *Laser 405nm*	1	CFP excitation CFP emission	Wl 415-495nm
2	**YFP Only** *Laser 514nm*	2 (GAsP Detector)	YFP excitation YFP emission	Wl 518-621nm
3	**FRET** *Laser 405nm*	Channel 1 CFP	CFP emission	Wl 415-495nm
		Channel 2 YFP	YFP sensitised emission	Wl 518-621nm

Table 10- Specific confocal microscopy acceptor photobleaching experiments settings

Setting	*Parameter*
Number of Z-Stacks Before Photobleaching	2

Cycles	10
Iterations	40
Pinhole	1 AU
Zoom	2.8
Photobleaching Planes	All planes
Speed	3
Pixel Dwell	32.97usec
Laser	514
Laser Power	100%

Table 11- Specific confocal microscopy settings utilised in 'before' and 'after' acceptor photobleaching scans

Setting	***Parameter***	
Pinhole	1AU	
Laser	YFP	2.1
Power	CFP	2.0
Optical Zoom	2.8	
Speed	7	
Gain	YFP	700
	CFP	800

First, two 'before' acceptor photobleaching scans were undertaken within cells expressing the sensor driven by Pannier, whereby direct YFP emission, CFP emission and YFP sensitised emission intensities were recorded. Cells expressing the cAMP sensor driven by Pannier were selected due to their strong expression of the sensor. Using the 'Live' function, a five-cell radius was selected using the 'Regions' tab in ZEN. Next forty iterations, using a 514 laser at 100% power, was undertaken to bleach the acceptor YFP within the five-cell radius selected. This photobleaching was undertaken equally at all planes

throughout the Z-Stack. SafeBleaching for the GaAsP detector was utilised to avoid damage to the microscope. Following this, five further scans recording direct YFP emission, CFP emission and YFP sensitised emission were recorded. Direct YFP emission, CFP emission and YFP sensitised emission were quantitated throughout the Z-stack and averaged, as measurements were only preliminary proof of concept, using ZEN software. Percentage direct YFP emission, CFP emission and YFP sensitised emission increase and decrease were quantitated.

2.35 RFP Direct Excitation to Assess PKA Sensor Expression

Direct RFP excitation, using the settings described in table-12), was undertaken to confirm FLINC expression within well-spaced SOP neu-FLINC$^+$ cells and pnr-FLINC$^+$ epithelial cell clones. To visualise neu-FLINC$^+$ cells, a direct-RFP excitation Z-stack of the notum was obtained facilitating assessment of the expression pattern, accounting for the presence of apexes at different cell depths which could present a misleading picture of expression. A direct-RFP excitation 4x4 tile-scan of pnr-FLINC$^+$ cells was obtained, as cells are an epithelial sheet we could be sure that the apexes were located at the same cell depth.

Table 12- The confocal microscopy settings used for direct RFP excitation

Setting	***Parameter***	***Justification***
Main Beam Splitter	458/561	Recommended beam splitter for laser 561nm
Laser		561nm
Pinhole	2AU	Double optimal
Speed	6	Increase signal detected
Pixel Dwell Time	2.06 µsec	Increase signal detected
Averaging	2	Increase image quality
Frame Size	1024 x 1024	Compromise between image quality and file size
Image Bit Depth	16-bit	
Interval Between Slices	1um	
Track Used	2	GaAsP detector photomultiplier tube

		ideal for low signal samples
Wavelength Detected	598-754nm	Detection of RFP emission

2.4 Epifluorescent Microscopy

Visualisation of cells via epifluorescent microscopy was performed using an Upright Olympus Epifluorescent Microscope. CFP direct excitation was undertaken at 436 nm using an LED light source with 50% power where gain was set to 1, rate 100 MHz and an exposure time of 25 ms. Images acquired were of 8 bit-depth. The pupal case was pealed back to reveal the notum, as previously described, and pupae were affixed ventral side down to a 76 x 26mm slide using double sided tape. 200 µL of 1% room temperature PBS was applied to form a droplet atop the notum; this enabled us to use the X60 water immersion lens which must be immersed in liquid for use. For full details of the microscopy protocol see (Maiellaro et al., 2016, Maiellaro, 2022)

2.5 Image Processing and Generation of Sensitised Emission Ratios

2.51 Image Processing

CFP emission and YFP sensitised emission images from each experiment were opened in ImageJ. Images were immediately converted to 32bit to allow for the existence of non-whole integers following image division. The Z-stack was duplicated to equally exclude extraneous slices (the cuticle and any black images). A maximum intensity Z-projection was created and a ROI (Region of Interest) selected around the cell of interest and moved adjacent to the cell, so any measurement of background intensity were physiologically relevant to the environmental context of the cell. Exceptions to this rule included where extremely bright fat bodies were present, in which case the ROI was moved directly above or below the cell instead.

Background intensity was measured throughout the original cropped stack, within this ROI, using the 'Multimeasure' tool. The stack was split and each individual background value was subtracted from its corresponding slice; this was repeated for both channels. Different backgrounds were subtracted for different cells within the same image where background intensity was measured to be significantly different within the image, as a local threshold was not available in ImageJ for 16 bit or 32 bit images. Stacks were then reconstituted. Following this, images were equally cropped so only the cell of interest and related protrusions were visible.

Following background subtraction, a threshold was applied to images in order to fully exclude background and facilitate creation of a ratiometric FRET image. The optimal threshold value was determined for both CFP emission and YFP sensitised emission images by employing a Huang global threshold to both whereby 'Stack Histogram' was selected.

Selection of the ‘stack histogram’ option generated a more accurate threshold, calculated by using the whole stack histogram, making it applicable to each slice within the Z-Stack. Upon analysis of CFP emission and YFP sensitised emission image histograms, regions of much higher pixel intensity (background) and lower pixel intensity (cell of interest) were identified. Therefore, a Huang global threshold was selected due to its nuanced ability to distinguish between high and low intensity pixel intensity, allowing efficient cell outlines to be defined. Thresholds were applied to images according to their grouping, using the lowest threshold within the group so not as to exclude important pixel intensity. A ratiometric FRET image was generated using the ImageJ ‘Image Calculator’ function where YFP sensitised emission was divided by CFP emission (YFP/CFP). A fire LUT was applied to the resultant image, generating a ‘heat map’ of cAMP concentrations throughout the cell. Conversion to 32-bit, thresholding and ratiometric FRET image generation were automated through use of a Macro created in ImageJ Macro language.

2.52 Quantification Sensitised Emission FRET Ratios

Thresholded YFP and CFP images, in addition to the corresponding ratiometric FRET images, were opened for each experiment. Brightness of YFP threshold images was adjusted using the Brightness/Contrast function within ImageJ, but values were not applied so as not to alter pixel values. First, windows were synchronised and a line was constructed marking the beginning of the protrusion determined by eye, as there was no clear distinction in ratio suggesting differentiation between cell cytosol and protrusion. Due to ambiguity in some images regarding protrusion identification and conflation of protrusions with background fluorescence, only protrusions where protrusion pixels were present at the same spatial coordinates in both YFP and CFP channels were used. A circular ROI (area 0.172μm^2) was dragged to the base of the protrusion, to the middle of the protrusion (where possible) and protrusion tip. Intermediate lateral protrusions were quantified, as these were best visible, within the intermediate region (3-6μm below the apex). The optimal slice, where the full intermediate lateral protrusion was visible, was selected. Ratios were quantified in these ROIs via the 'Measure' tool in ImageJ (figures-17,18).

Within Neuralized pupae a line, 0.5μm in length, drawn perpendicular to the line indicating the protrusion beginning was constructed. A circular ROI 0.172μm^2 in area was drawn at the end of such line, termed the cytosol marker, and cytosolic ratio was quantified within this region. Whereas, in Pannier pupae, cytosolic ratio was quantified in a circular ROI, 0.172μm^2 in area, to the left of the line marking protrusion start. This was due to limited cytosol available for measurement 1μm from protrusion commencement. (figure-17).

2.521 Statistics

Outliers were identified using the ROUT method, which enables detection of multiple outliers at once. No outliers were detected for pnr-camps-epac1$^+$ clones or neu-camps-epac1$^+$ cells. A Shapiro-Wilk test for normality indicated that both data sets were normally distributed therefore parametric One-Way ANOVA was undertaken to assess differences in FRET ratio within the cell cytosol and protrusion base, middle and tip. In addition to ANOVA, Bartlett's test and the F test were undertaken to determine whether standard deviations were significantly different. An assumption of ANOVA is that standard deviations must not be statistically significantly different. Both the F-test and Bartlett's test indicated that standard deviations between the cell cytosol and protrusion base, middle and tip were statistically significantly different in both pnr-camps-epac1$^+$ clones or neu-camps-epac1$^+$ cells. Therefore, data was transformed using a logarithmic transformation (Log(Y)), to equalise standard deviations and parametric One-Way ANOVA was undertaken on transformed data. Statistical significance was set to $p<0.05$ and all statistical tests were undertaken using GraphPad Prism.

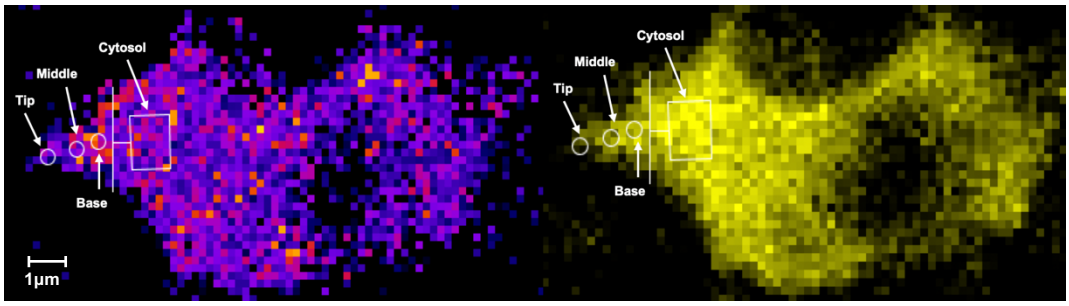

Figure 17- The position of ROIs to assess relative basal cAMP concentrations within the cell cytosol and protrusion base, middle and tip. *Slices derived from the 'intermediate' regions of neu-camps-epac1$^+$ cells or pnr-camps-epac1$^+$ clones were used to measure cAMP gradients by obtaining mean grey values within the ROIs shown in this figure.*

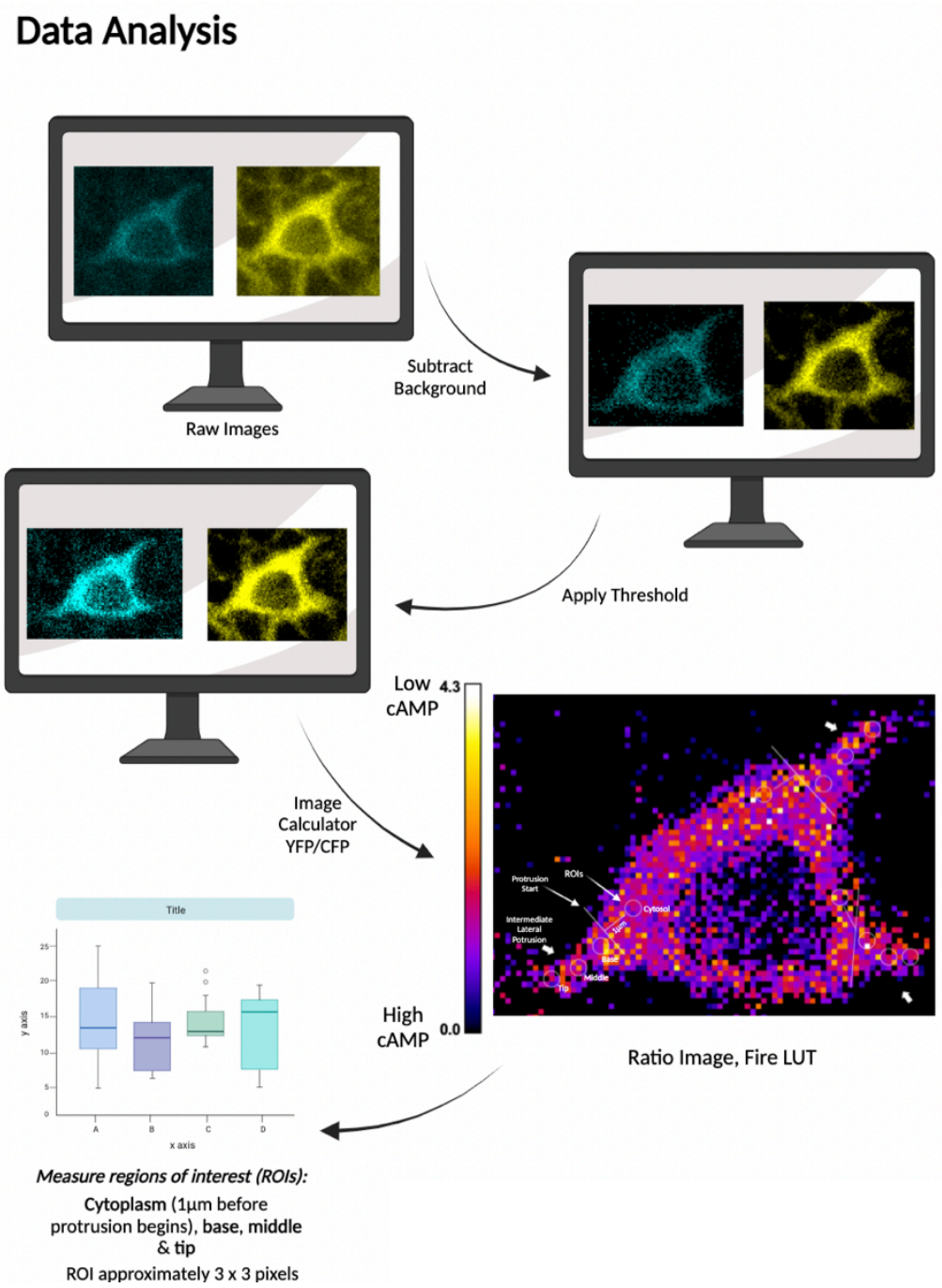

Figure 18- The data analysis and image processing workflow for confocal microscopy sensitised emission FRET data generated using the genetically encoded cAMP FRET biosensor. *Following conversion to 32-bit, images were background subtracted and a threshold applied. The YFP image (sensitised YFP emission) was divided by the CFP image (CFP emission) to generate a ratio image, which was encoded with a Fire LUT to show cAMP 'hot' areas. Mean grey values within the ratio images were extracted and graphed in different ROIs (cytosol and protrusion base, middle and tip).*

2.6 Protocol Optimisation

2.61 Troubleshooting Sensor Expression

2.611 YFP Excitation to Assess Sensor Expression

Expression levels of the genetically encoded cAMP FRET biosensor are temperature dependent. Furthermore, temperature also modulates the speed of *Drosophila* growth. Therefore, it was important to strike a balance between optimal sensor expression and imaging pupae at the correct age. In order to determine which incubation regime boasted best sensor expression in well-spaced SOP cells, neu-camps-epac1^{+} pupae were incubated for 14.5 hours using two different incubation regiments (table-13). At 14.5 hours, pupae were removed from the incubator and mounted as described in (Section 2.31 Pupae Mounting). Following removal from the incubator, pupae were kept and imaged at room temperature (approximately 22°C). In order to assess sensor expression, YFP was excited using only track two of the FRET configuration protocol. A 4x4 tile-scan (size 786.4 x 786.4µm) was undertaken at speed 6, where frame size was adjusted to 1024 x 1024. The cell depth where the greatest number of neu-camps-epac1^{+} cells were observed was selected for direct YFP excitation tile-scans. As the purpose of excitation was visualisation of sensor expression, gain was optimised for each sample to maximise the number of cells visible.

Table 13- Different incubation regimes tested. *The time pupae spent at 18 degrees and 25 degrees in each regime is indicated.*

Incubation Regime	Time Spent at 25°C	Time Spent at 18C°
Regime A	14.5	0 hours
Regime B	16 hours	5.5 hours

2.612 Testing Different Pupal Ages

Neuralized pupae were incubated at 25°C for 14.5 hours. Following removal from the incubator, pupae were kept and imaged at room temperature (approximately 22°C). Images were acquired in the same manner as detailed in. Images were analysed by eye to determine which regime produced optimal expression.

2.62 Optimisation of Image Processing Protocol

2.621 Background Subtraction Optimisation

A ROI, of the area 60.576μm^2, was created using the freehand drawing tool in Image J and applied to five different positions within 10 images (figure-19). The ROI area was selected to provide a representative average of the mean grey value within each area. Positions were selected as shown in figure-20, to provide information on average grey values in the top right-hand corner, top left-hand corner, bottom right hand corner, bottom left hand corner and middle of the image. ROIs were saved to the ROI manager, allowing them to be applied at the

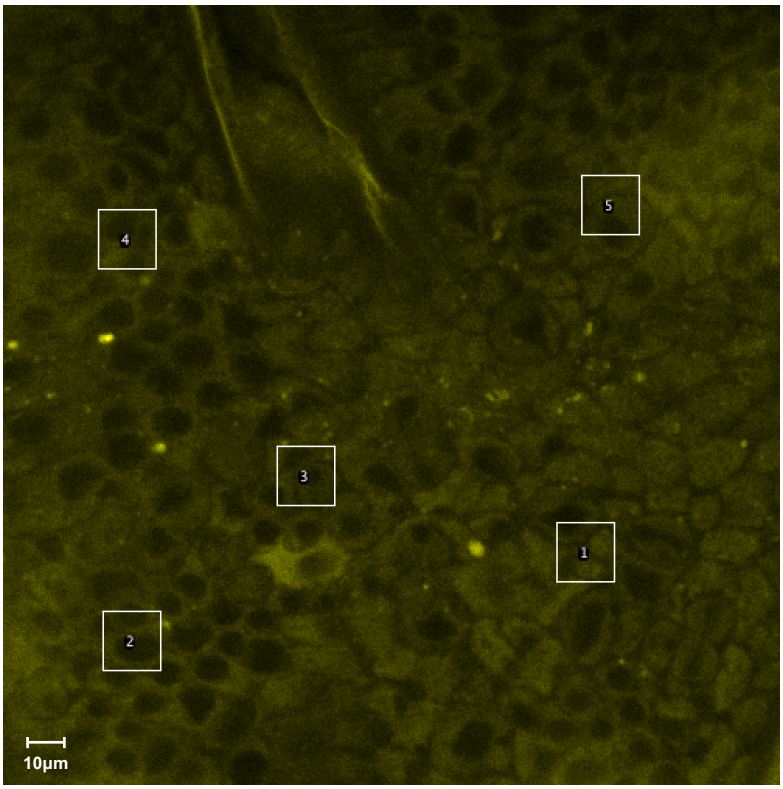

Figure 19- The ROIs applied to measure mean background grey values at five different positions within the image. *ROIs were kept in the same position for all measurements and had an area of area 60.576μm^2. Background measurements were undertaken within the intermediate region images of pnr-camps-epac1$^+$ clones or neu-camps-epac1$^+$ cells.*

same spatial coordinates in all images. Using the multi measure function, measurements at each position in each slice were obtained. Background intensities were plotted to determine whether background intensities were uniform throughout the image at different depths. All images included in the analysis possessed sensor expression driven by Neuralized as the sensor was expressed at lower levels within these cells, thus background subtraction was a more significant operation in comparison to Pannier driven cells, where expression was much higher.

2.612 Statistics

No outliers were detected within YFP images but as two outliers were identified within CFP images, values above 435 were eliminated from further analysis in CFP images. Following, this parametric Two-Way ANOVA was undertaken to assess mean background variability at different depths within the Z-stack and at different positions in the image.

2.622 Calculating Average YFP and CFP Thresholds

Using the ImageJ automatic global thresholding scheme, the optimal threshold for fifteen cells was calculated using the ImageJ Global Threshold function, where the stack histogram was employed. This ensured the optimal threshold calculated was appropriate for application to all slices within the stack, as it is inadvisable to split a stack and calculate an individual threshold for each slice. Before calculating the optimal threshold, cells were cropped to ensure background regions, of higher intensity than the cell of interest, were excluded. This prevented the generation of an inappropriate higher thresholds, which could lead to inaccurate measurements and decreased contrast within ratio image. Optimal threshold values were tabulated and averaged, producing an average CFP threshold value and average YFP threshold value. Different threshold values were calculated for YFP and CFP as mean YFP grey values were greater than mean CFP grey values; this prevented inappropriate penalisation of lower intensity CFP images. These average thresholds were subsequently applied to all corresponding images within the data set.

2.623 Discovering the Optimal Thresholding Scheme

The ‘Try All’ global threshold function was employed in ImageJ Automatic Thresholding to determine the ideal global thresholding for each data set. The application of the ‘Try All’ function created a compilation image, using the image histogram, in which each square depicted the image with a different threshold applied. Ticking the ‘Image Histogram’ created a single threshold which was applicable to the whole stack instead of a 2-dimensional threshold, optimised for a single slice which would not be applicable to all slices within the Z-stack. This was repeated for both YFP and CFP images, where sensor expression was driven by Neuralized in five images and Pannier in five images. The most accurate thresholds were judged by eye. Background subtracted images for CFP and YFP were compared to each threshold square and the optimal thresholds, most true to the background subtracted image, were judged. A list of the top three hits for Neuralized and Pannier driven images and the optimal threshold scheme selected based on which scheme worked best for both types of image.

2.624 Threshold Groupings

Background subtracted CFP and YFP images were opened in ImageJ and the global 'Threshold' window opened. The 'Stack Histogram' option was selected; this function considers the image histogram as a whole to produce the optimal threshold as opposed to calculating the optimal threshold for an individual slice and applying it to the whole stack. Thus, optimal threshold values were more appropriate and could be applied to the entire stack. The Huang threshold was applied and optimal threshold values recorded for each cell or image, where both the upper and lower threshold values were noted. In images obtained from flies expressing the cAMP sensor driven by *neu,* each cell within the image was equally cropped in the YFP and CFP channels to exclude higher intensity background structures which could skew optimal threshold measurements. Different cells within an image were treated as individual entities, in that individual optimal threshold readings were taken for each cell as opposed to one value for the image as a whole. However, in images obtained from pnr-camps(epac1)$^{+}$ clones, a single optimal threshold value was obtained for each image. This was due to the nature of pnr-camps(epac1)$^{+}$ images obtained; cells appear in patches of clones and it is difficult to differentiate and accurately crop individual cells, as opposed to well-spaced cells observed from *neu*-driven sensor expression. Furthermore, there was greater variation in pixel intensity within *neu*-driven sensor images in comparison to *pnr*-driven sensor images. Thus, treating each cell individually was more important within *neu*-driven images than *pnr*-driven images.

All threshold values were plotted in a scatter plot using Prism software, where Median and Interquartile Range (IQR) could be visualised on the graph. Optimal threshold groupings were determined using the scatter plot to identify clusters of thresholds. Each group possessed a range of approximately ten within Neu-driven images; this was to ensure the

range of each group was not too wide as to apply an inappropriate threshold to any image. Images were then sorted into their appropriate threshold groups and the lowest bound from each group was applied to all images within the group (Table-14, Table-15). Applying the highest value could exclude key pixel values from images falling within the lower bound of the group. Due to the small number and variation between thresholds within Pnr-driven images, a unique optimal threshold was applied to each image so as not to inappropriately penalise lower or higher intensity images. New ratiometric FRET images were then generated using the ImageJ Macro created by the author (2.627 Automating Image Processing).

Table 14- Threshold groupings applied to YFP and CFP background subtracted images, driven by neuralized. *Threshold groups were determined by measuring the optimal thresholds for all images within the data set in ImageJ, creating a scatter plot to visualise threshold distribution and creating groups with a range of ten*

Group Number	*YFP Threshold*	*CFP Threshold*
1	7.36	11.32
2	15.44-25.54	14.05-24.94
3	25.88-38.4	25.96-34.47
4	41.33-55.81	42.55-53.50
5	69.70-80.16	56.82-66.00
6	85.95-96.85	69.99-80.00
7	109.94-115.27	84.12-94.00

8	156.99-168.19	97.04-109.16
9	244.78	131.25-139.76
10	263.26	170.64-178.25
11	318.33	N/A

Table 15- Threshold groupings applied to YFP and CFP background subtracted images, driven by pannier. *Threshold groups were determined by measuring the optimal thresholds for all images within the data set in ImageJ, creating a scatter plot to visualise threshold distribution and creating groups with a range of ten*

Group Number	*YFP Threshold*	*CFP Threshold*
1	695.80	581.53
2	820.35	597.47
3	914.67	605.53
4	1539.01	1025.96
5	2172.62	1540.85

2.625 Testing the Thresholding Method

To assess the effect of threshold application on sensitised emission FRET ratio, mean grey values within the intermediate protrusions of ten Neuralized-driven cells were measured, before and after application of thresholds. Measurements were taken within the cytosol, base, middle and tip of intermediate-lateral membrane-based protrusions in CFP emission and YFP sensitised emission channels. ROIs were applied in the same manner. Mean grey values, in addition to ROI areas to rule out alteration of averages due to variations in total pixel number, were determined using the 'Measure' function in ImageJ. ROI spatial coordinates were maintained for all measurements within a family of images. Data was tested to determine outliers, none were detected, and a Shapiro-Wilk normality test undertaken to determine whether a parametric test should be employed. Upon discovering that data was normally distributed, parametric Two-Way ANOVA was applied to determine whether variation between un-thresholded images and thresholded images was statistically significant, where $p<0.05$ was considered statistically significant.

2.626 Application of Pixel Averaging Filters

First, ten Neuralized-driven background subtracted CFP emission and YFP sensitised emission images were converted to 32-bit. Background subtraction was undertaken. Next, the ImageJ 3x3 Smooth Pixel Averaging Filter was applied to both channels equally, using the 'Smooth' function within ImageJ. Smoothed ratio images were generated using the ImageJ 'Image Calculator' by dividing YFP sensitised emission by CFP emission. FRET ratios were quantitated within the cytosol and the base, middle and tip of intermediate-lateral membrane-based protrusions of smoothed images and their corresponding non-smoothed images, where all ROIs within an image family possessed the same spatial coordinates. Outliers were determined using the ROUT method and normality determined using the Shapiro-Wilk normality test, ideal for small samples. Analysis of variance between FRET ratios within ten smoothed images and the identical non-smoothed images was compared using Two-Way ANOVA, with Greenhouse-Geiser correction, where statistical significance was considered to be $p<0.05$.

2.627 Automating Image Processing

A MACRO was designed, using the ImageJ programming language, to convert images to 32-bit, apply thresholds and divide images (YFP sensitised emission/CFP emission) to create a ratio image. The accuracy of MACRO-ratio images was tested to determine whether the MACRO functioned as designed by measuring the FRET ratio within intermediate-lateral membrane-based protrusions in the cytosol, base middle and tip, of MACRO-generated and manually generated images. The MACRO was as follows:

```
selectWindow("CFP NB.czi");
run("32-bit");
setAutoThreshold("Huang dark stack");
setThreshold(x, 10000000000000000000000000000000.0000);
run("NaN Background", "stack");
selectWindow("YFP NB.czi");
run("32-bit");
setAutoThreshold("Huang dark stack");
setThreshold(y, 10000000000000000000000000000000.0000);
run("NaN Background", "stack");
imageCalculator("Divide create stack", "YFP NB.czi","CFP NB.czi");
selectWindow("Result of YFP NB.czi");
run("Fire");
```

2.63 Optimisation of Measuring cAMP Sensitised Emission FRET Ratios in ImageJ

First, the ratiometric FRET image and corresponding YFP background subtracted image were opened in ImageJ. Brightness/contrast were optimised for adequate visualisation of protrusions within the YFP background subtracted only. Adjusted brightness/contrast values were not applied to the image, as this function alters pixel values which could impact subsequent creation of ratiometric FRET images. The intermediate region, usually located 3-6μm below the apex, was identified within the Z-stack and the ratio and YFP background subtracted windows synchronised for ease of drawing ROIs(Couto et al., 2017). Intermediate lateral protrusions were the target of sensitised emission FRET ratio measurements as these protrusions experienced the most favourable sensor expression, thus were best visualised in comparison to apical microvilli-like protrusions and basal protrusions which were barely visible in most cells.

Identification of protrusion start was undertaken by eye; the ratiometric FRET image was examined to determine whether distinct contrasts in FRET ratio were present which could denote a clear separation between the cell cytosol and protrusion. A lower FRET ratio (and high cAMP concentration) was signified by blue/purple colours and a high FRET ratio (and low cAMP concentration) was indicated by red/orange colours. However, unfortunately in most images examined (both Neuralized and Pannier) such a clear distinction was not observable, in which case the protrusion start was classified as the intersection of the protrusion with the outer cell edge. Following identification of protrusion start, a line was constructed, separating the protrusion start from the cytosol, using the straight-line tool in ImageJ. All further ROI placements were undertaken using the YFP background subtracted image. This was due to ambiguity, within some ratiometric FRET images, as to protrusion tip location due to pixel loss during creation of ratiometric FRET images, due to the thresholding process. Protrusion

form and position was much clearer and easily visualised within YFP background subtracted images. A further line, 1μm in length, perpendicular to the line marking protrusion start and extending into the cell cytosol was constructed. A circle, of the area 0.388μm, was created and placed at the end of the line extending into the cytosol; this served as ROI for cytosol measurements for each protrusion. An area of $0.388\mu m^2$ was selected as it fit the width of most protrusions, allowing the circle to be placed, and measurements taken, at different points within the protrusion. Subsequently, the circle was placed at three different locations within the protrusion, the base (protrusion side of the protrusion start marker, ROIs were positioned so as to slightly touch the marker), middle (approximately halfway between base and tip) and tip (defined as the furthest point, within the protrusion, from the protrusion start marker) (figure-19). Mean grey values were recorded, via the 'Measure' function in ImageJ, for each circle along the protrusion and the cytosol to probe cAMP gradients and compartmentalisation of signals within the protrusion and adjacent cytosol. Mean grey values were chosen as a measurement to give a snapshot into the ratios within each region. Sheet-like protrusions within the intermediate region often extend throughout the Z-axis, that is to say they can appear in multiple slices within the Z-stack. Therefore, in these cases measurements of the protrusion throughout the intermediate region were taken, where ROIs were maintained in the same position where possible. In some instances, small shifts of the protrusion occurred throughout the Z-stack due to the long scan time (protrusions are dynamic therefore may move within the time taken to scan the cell). Where this was found to occur, ROIs were shifted slightly to accommodate.

2.631 Statistics

Data was grouped by slices, (i.e. slice four protrusions were grouped together etc.) and each slice was treated as a separate data set. Outliers were identified using the ROUT method; this allowed

identification and exclusion of multiple outliers at once. Following outlier exclusion, the Shapiro-Wilk test was applied to determine normality. Within slice three, outliers of or above 2.455 were excluded from further analysis. Within slice four, outliers of or above 2.659 were excluded from further analysis. Within slice five outliers of or above 3.668 were excluded from further analysis. All data was normally distributed, therefore parametric one-way ANOVA and Tukey's Multiple Comparisons were applied to determine statistical significance, where statistical significance was set to $p<0.05$. Sample size within slice six was too small to undertake statistical tests. Sample sizes for each depth and region are displayed in Table-16.

Table 16- Number of samples for each position at each cell depth.

Cell Depth	Cytosol	Base	Middle	Tip
3	23	21	13	22
4	20	20	11	20
5	15	14	8	13

2.7 Controls

2.71 Pixel Intensity Addition

To determine whether our protocol could successfully detect changes FRET raito, pixel values within a defined region of interest (ROI) of segmented YFP images were increased by 50% to simulate change in cAMP concentration. YFP emission was altered as YFP sensitised emission is liable to change more dramatically than moderate alterations in CFP intensity, upon an increase or decrease of cAMP). New ratiometric FRET images were created employing the altered segmented YFP images; ratios were quantitated and compared to the same ROI within normal ratiometric FRET images. Increases in YFP intensity should correspond with an increase in FRET ratio within the defined ROI in comparison to the rest of the cell, in which the FRET ratio should remain stable and match the original ratiometric FRET image.

First, YFP intensity was quantitated within the region of interest for all images involved. We found average pixel intensity was around 500 to 550 for all images, therefore we determined an increase of 50% pixel intensity would be sufficient to observe a change in FRET ratio. Segmented *neu/epac1(camps)* YFP images, where background was already subtracted as previously described, were opened and a ROI of the area 2.025 was selected within the cytosol. This area was used as it was large enough to provide a representative cytosol measurement within the small area adjacent to the protrusion. The same ROI was used for all images within a single replicate, however different ROIs were employed for different image families, although an area of 2.025 was consistent for all ROIs. Pixel intensity was quantitated for fifteen cells within the selected ROI in the intermediate region (slice four), so as to roughly match the depth ratios within intermediate lateral protrusions were quantified. Using this data, it was determined an

increase in pixel intensity of approximately 50% (200) was sufficient to observe a change in FRET ratio. The ‘Add’ function in ImageJ was employed to artificially increase YFP pixel intensity within this ROI and new ratios were created (YFP/CFP) using the artificially increased YFP image and the corresponding unaltered CFP segmented, background subtracted image, via the ImageJ ‘Image Calculator’. Ratios were quantified in unaltered ratiometric FRET images and new ratiometric FRET images, where pixel intensity was increased.

The Shapiro-Wilk test for normality was first undertaken, as this test can accurately detect normal distribution in smaller sample sizes. Outliers were identified using the ROUT method; one outlier in FRET ratio was detected within the ‘altered pixel intensity FRET ratios’ data set (ratio, 3.918) and excluded. As the data was non-normally distributed, the non-parametric two-tailed T-Test Wilcoxon-Matched Pairs Signed Rank Test was carried out with statistical significance set to $P<0.05$.

2.72 Cytosol Control

Cytosolic mean FRET ratios were quantitated within all slices of the intermediate region for Pannier-driven clones and Neuralized-driven cells containing sensor expression (usually 3-6um below the apex), using the 'Measure' function in ImageJ. ROIs possessed the same spatial coordinates for images within a family and ROI area remained consistent across all measurements. A ROI area of 1.939 was used as this was deemed large enough to give a representative measurement of cytosolic ratio, while also being small enough to fit within the cytosol at all cell depths. Cytosolic measurements within Pannier-driven clones was more difficult, as less cytosol was available for measurement and where cytosol was available, it was often difficult to distinguish which cell it belonged to. Furthermore, some Pannier clones did not possess measurable cytosol at deeper depths of the intermediate region. Ten Measurements were undertaken within ten pnr-camps(epac1)$^{+}$ clones and twenty neu-camps(epac1)$^{+}$ cells. Data was assessed to determine outliers using the ROUT method and ratios above 2.146 were excluded from further analysis in neu-camps(epac1)$^{+}$ cells. No outliers were identified within the Pannier clones data set. Next, data was tested for normality to, determine whether a parametric or non-parametric test was suitable, using the Shapiro-Wilk test for normality. Both data sets were found to be normally distributed, therefore parametric ANOVA with Tukey's Multiple Comparisons was undertaken on Neuralized data and an Unpaired T-test on Pannier data as n was too small for ANOVA. The aim was to determine whether variance between cytosolic ratios at different depths was statistically significant. $P<0.05$ was considered statistically significant.

Chapter 3: Protocol Optimisation

3.1 Taking Sensitised Emission FRET Measurements Using Wide-Field Epifluorescence Microscopy

Previously, studies making use of the cAMP FRET biosensor to study *Drosophila melanogaster* motor neurones successfully employed wide-field epifluorescence microscopy techniques to generate ratiometric sensitised emission FRET measurements using this cAMP FRET biosensor(Maiellaro, 2022). Indeed, historically epifluorescence microscopy was the optimal technique for undertaking these studies due to its ease of use and availability. Therefore, we set out to test the suitability of this approach through direct CFP excitation of cells to ascertain whether actin protrusions could be accurately visualised. Where sensor expression was driven by the promoter Neuralized, no epithelial cells containing the sensor were visible within the notum as visualised using widefield techniques, despite the presence of neu-epac1-camps^{+} cells being confirmed using an epifluorescent microscope. Furthermore, pupae were incubated at 25°C for the maximum amount of time eliminating the contribution of an un-optimised incubation protocol, although cells were not checked using a confocal microscope following visualisation using widefield techniques to ensure sensor-expressing cells could be visualised. High levels of auto fluorescence were observed and, although a slight brightening of the fluorescent field was detected upon excitation of CFP at the appropriate depth where one would expect the well-spaced epithelial cells to lie, any structures or cells were indistinguishable from the background fluorescence. Upon repeating this experiment using pupae where sensor expression was driven by the promoter Pannier, a similar effect was observed; fluorescence of any epithelial cells within the notum was undetectable (figure-20). Therefore, in all future

experiments confocal microscopy techniques were employed as they enjoyed greater spatial resolution.

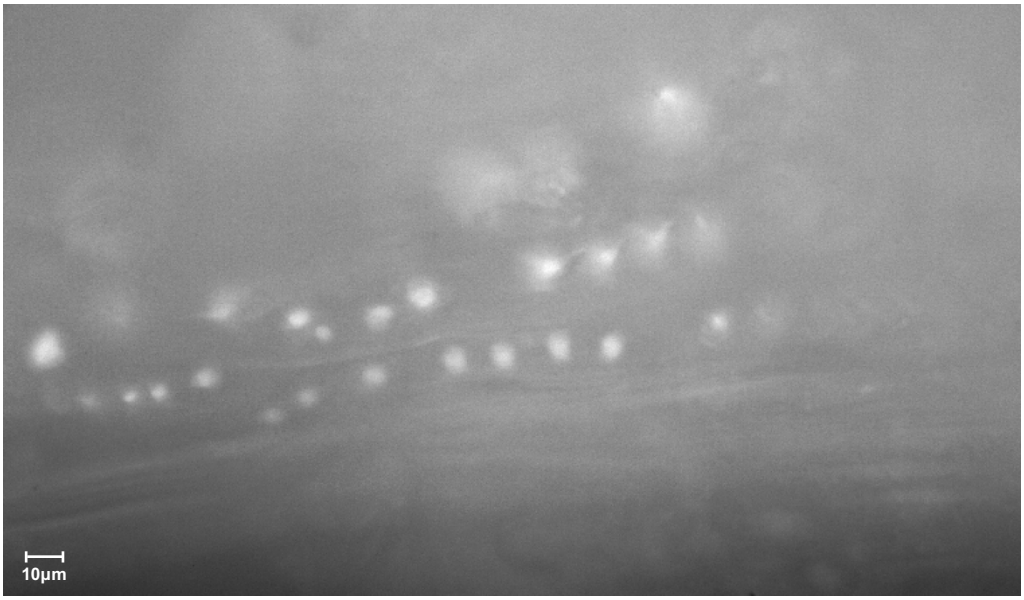

Figure 20- Epifluorescence microscopy image depicting cells at the location of the notum expressing the cAMP sensor. *Images were acquired using a Olympus upright Epifluorescence microscope by directly exciting CFP. It was unclear whether these cells were epithelial in origin as expression did not fit the expected pattern of epithelial cell expression in pnr-camps-epac1^{+} clones or neu-camps-epac1^{+} cells .*

3.2 Optimisation of Sensor Expression

Initially we undertook direct excitation of YFP to determine the level of sensor expression within the notum, to determine whether expression levels were sufficient to undertake sensitised emission FRET experiments. Direct YFP excitation is independent of cellular cAMP concentrations, as it was not dependent on transfer of energy from CFP to YFP which, in turn, is dependent on cellular cAMP concentrations. Thus, direct YFP excitation provides insight into whether poor sensor expression is due to low levels of cellular cAMP or weak promoter activity. Furthermore, direct excitation of YFP provided a second advantage as any photobleaching CFP fluorophores could compromise the integrity of sensitised emission FRET measurements by artificially decreasing the efficiency of energy transfer from the CFP fluorophore to YFP fluorophore. Additionally, as the YFP fluorophore is two to three times brighter than the CFP fluorophore, visualisation of sensor expression by eye was easier via direct YFP excitation(Börner et al., 2011).

Upon direct YFP excitation, we expected to observe a regular pattern of well-spaced cells expressing the sensor, as previously characterised, within Neuralized-driven pupae, where the actin-binding domain of *Drosophila* Moesin (Moe) was fused to GFP and expressed using the Gal4-UAS system to genetically label actin protrusions. This aided visualisation expression patterns and observation of the full range of membrane-based protrusions observed. Within Pannier driven pupae, a field of epithelial cells expressing the sensor covering the whole notum is observed (figure-21).

Following direct excitation of YFP in pupae where sensor expression was driven by Neuralized, we observed that the number of cells expressing the sensor was low, and in some cases no cells within the notum expressed the sensor, despite presence of sensor expression being confirmed using a GFPscope. Conversely pnr-camps(epac1)$^{+}$ cells within the notum displayed strong sensor expression, a field of cells within the notum expressing the sensor was observed in almost identical fashion to GFP-Moe images. These results indicate that

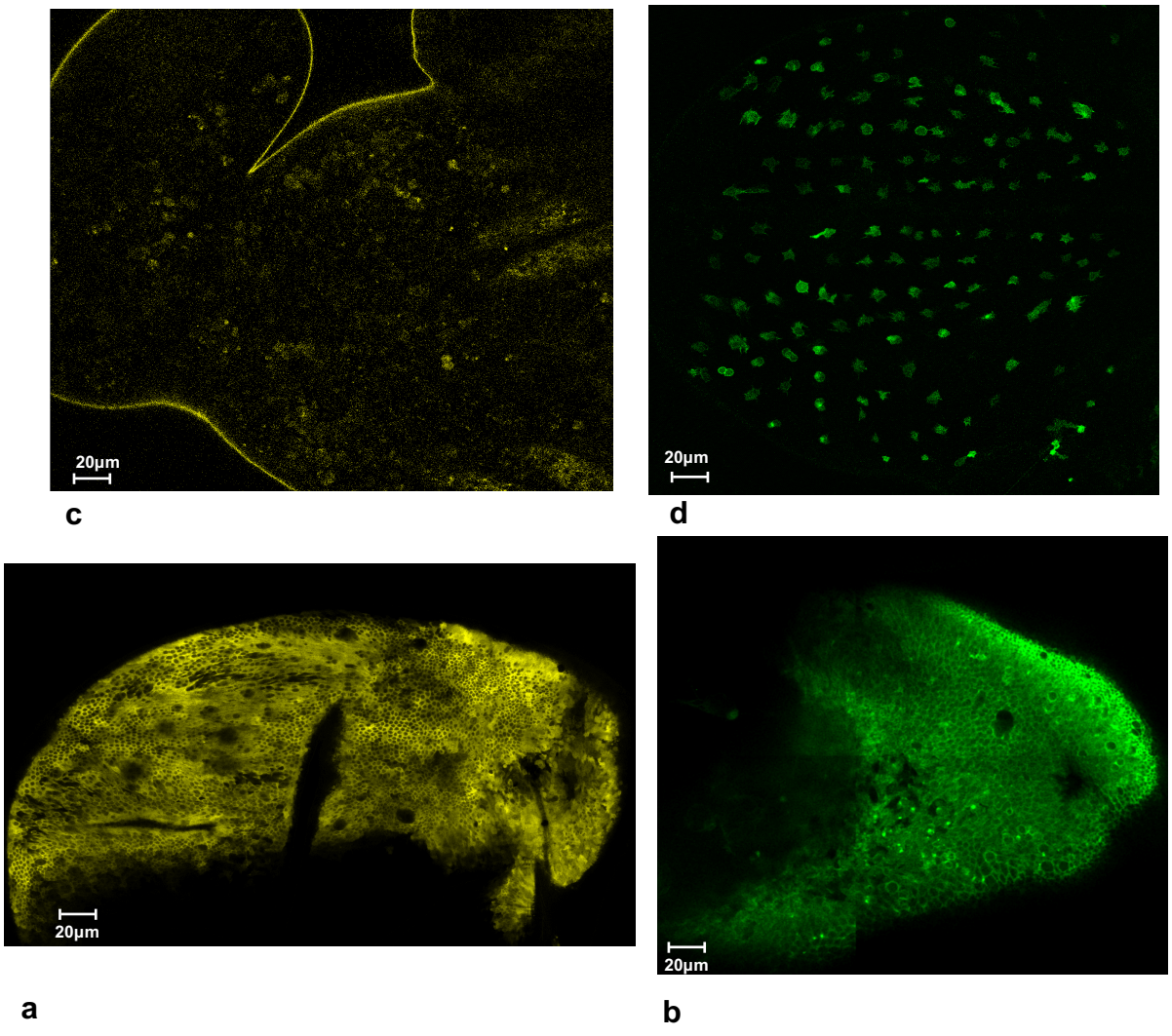

Figure 21- Expected and actual patterns of expression using the promoters Neuralized and Pannier, within the notum of Drosophila melanogaster*. A Pannier and Neuralized tile-scan were acquired using a ZEISS 880C confocal microscope. Expression of GFP-Moe was driven by tissue specific promoters Neuralized (d) and Pannier (b) to confine actin labelling to the notum. Direct YFP excitation of tile-scans of the notum were acquired where sensor expression was driven by the tissue specific promoter Neuralised (c) and Pannier (a). Tile-scans Images were smoothed and brightness/contrast adjusted for visualisation using ImageJ.*

Neuralized pupae possessed poor sensor expression within neu-camps(epac1)$^{+}$ cells and the pattern of expression did not match wild-type GFP-Moe images. Whereas Pannier pupae exhibited strong sensor expression and expression was almost identical to wild-type GFP-Moe images.

Having determined that Neuralized pupae were associated with weak sensor expression, we set out to optimise our protocols to increase sensor expression within neu-camps-epac1^{+} cells. Initially, we considered the notion that poor sensor expression could be due to the incubation protocols. Previously, the lab reported that Neuralized pupae driving expression of a different FRET sensor were transferred to 25°C from 18°C two hours prior to pupae imaging as it was estimated that protein folding would take approximately two hours and a short time at 25°C maximised fluorophore brightness. However, this incubation protocol was optimised for a different sensor. Therefore, we devised and tested two incubation regimes, where pupae were incubated at 25°C for 14.5 hours (regime A) or 18°C for 18 hours then transferred to 25°C for the final 5.5 hours (regime B).

Where pupae were incubated via regime A, a direct YFP excitation tile-scan showed very few cells expressing the sensor and, in some cases, no cells within the notum were recorded to be expressing the sensor. Pupae incubated using regime B experienced improved sensor expression, with a greater number of cells expressing the sensor, following a direct YFP excitation tile-scan in comparison to regime A (figure-22). Although improved sensor expression was achieved using incubation regime A, overall sensor expression was still poor. Therefore, we aimed to further optimise the protocol by adapting the confocal microscopy acquisition protocol to maximise sensor signal.

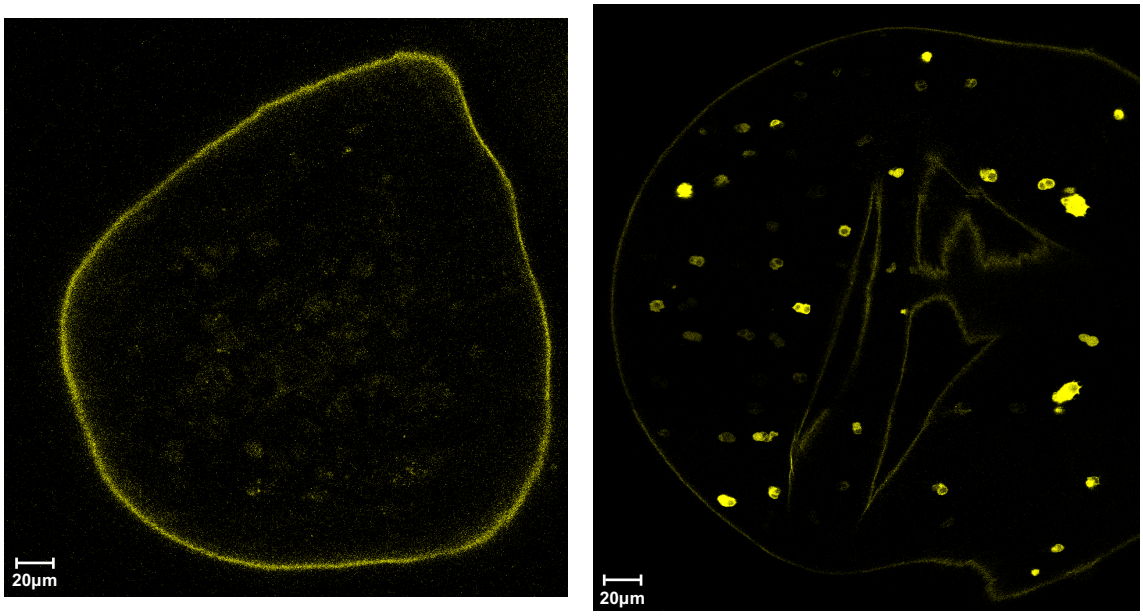

Figure 22- Tile-scans revealed sensor expression was improved where pupae were incubated by regime B*. Direct excitation YFP tile-scans were obtained, where cAMP sensor expression was driven by the tissue specific promoter Neuralized, to determine whether incubation regime A (a), where pupae were incubated at 18°C for 16 hours and 25 °C for 5.5 hours, or B (b), where pupae were incubated at 25 °C for 14.5 hours, maximised sensor expression.*

Although incubation protocol B was shown to be successful in increasing sensor expression, we were determined to further maximise this to increase the number of cells available for use in experiments and decrease the number of pupae used. Therefore, we set out to assess the effect of pupal age on sensor expression. We hypothesised that pupae incubated for a longer duration would display a greater number

of cells as the longer incubation time would allow increased protein folding of the sensor and more cells would be developed at later stages. It is important to image cells, in which sensor expression is driven by Neuralized, before the first cell division 16 hours APF and beyond, as prior to this, cells are well-spaced and representative of epithelial cells. Although previous work showed that the majority of SOP patterning was complete and SOP cells underwent cell division at 16 hours APF and beyond, incubators utilised to age pupae could be at lower temperatures than the display or different crosses could take different lengths of time to reach the same developmental stage. Therefore, using incubation regime B, tile-scans of the notum were

undertaken at different pupal ages: 14 hours APF, 15 hours APF, 15.5 hours APF and16+ hours APF to determine whether this was the case.

Upon examining direct YFP excitation tile-scans of the notum at different ages, it was revealed that 14 hours APF pupae expressed the sensor in very few/no cells (figure-23). Furthermore, expression was

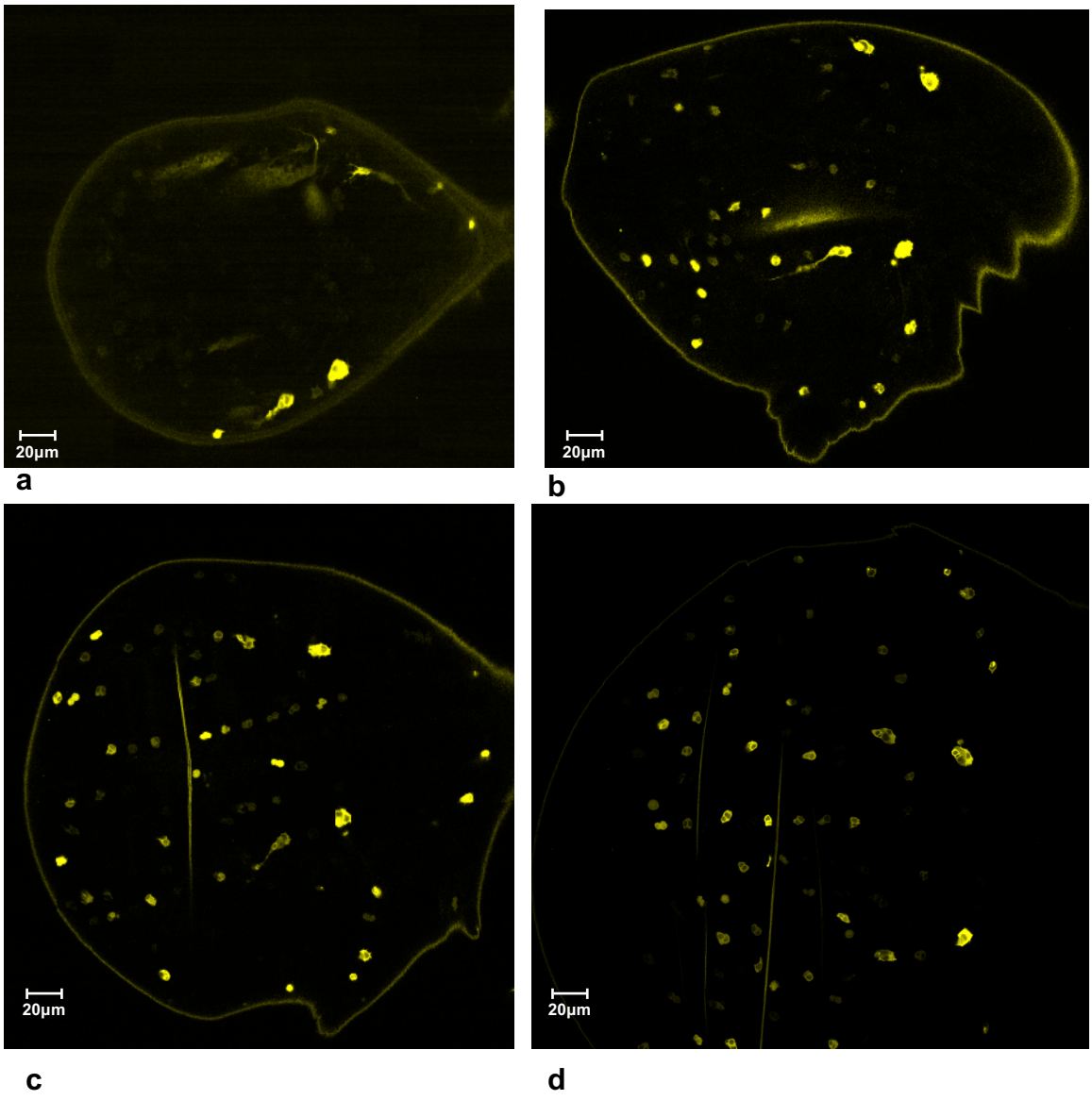

Figure 23- Direct YFP excitation of the Drosophila melanogaster notum expressing cells containing the sensor driven by promoter Neuralized at different ages. *TL 14hrs (a), TR 15hrs (b), BL 15.5hrs (c), BR 16hrs (d). At 14 hours APF, sensor expression was poor, with only the neurone expressing the sensor. More cells expressing the sensor were observed at 15 and 15.5 hours APF, but cell division meant pupae were unsuitable for use in experiments past 16 hours APF. White triangles mark the type-I neurone which innervates the sensory organ macrochaete cells (Huang et al., 1991)*

very weak, although sensor expression within the macrochaetes and

neurone innervating the notum was strong. At 15 hours APF, sensor expression was greatly improved with an increased number of cells expressing the sensor, albeit at low levels. 15.5 hours APF seemed to be the optimal age for maximal sensor expression with a more complete SOP cell pattern within the notum. Sensor expression, by eye, appeared brighter however there was an increased presence of dividing cells experiencing brighter sensor expression, which cannot be utilised for FRET experiments as neu-camps(epac1)$^{+}$ cells must be imaged before the first cell division and before they commit to their cell fate (figure-23). Pupae imaged at 16 hours APF and beyond were unsuitable for FRET experiments; the majority of cells were dividing and had taken on bristle cell fate.

To determine whether the sensor was well expressed at different cell depths and within membrane-based protrusions, direct YFP excitation Z-stacks were obtained using pupae where sensor expression was driven by Neuralized and Pannier. These experiments revealed direct YFP sensor was expressed well expressed within the following protrusions in cells driven by both promoters: apical microvilli-like protrusions, intermediate lateral protrusions and basal protrusions. It was observed that at all cell depths, the sensor enjoyed good expression within the cell body and cytosol as expected (figure-24).

However, within the basal regions, sensor expression was weaker towards membrane-based protrusion tips.

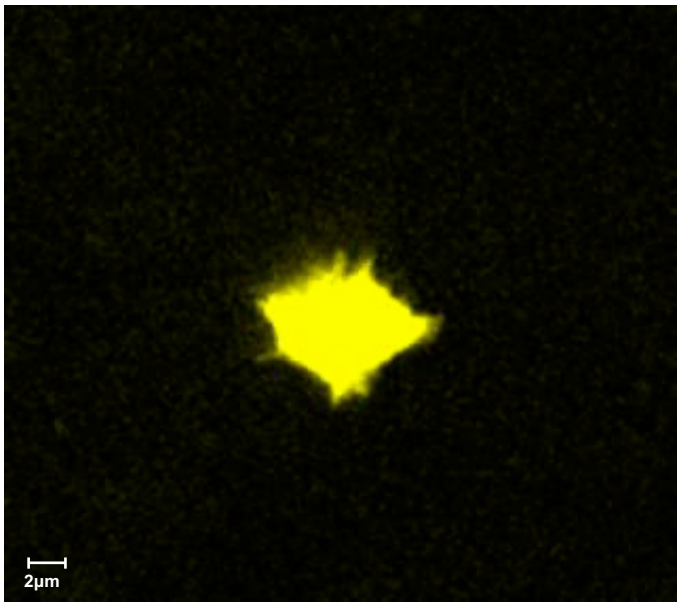

Figure 24- The cAMP sensor was well-expressed within membrane-based protrusions- apical microvilli-like protrusions, intermediate-lateral protrusions and basal protrusions. *(should I distinguish between the different types i.e. filopodia etc). Direct YFP excitation was performed using confocal microscopy. Brightness and contrast were adjusted using ImageJ to aid visualisation.*

3.3 Sensitised Emission FRET Acquisition Protocol Optimisation and Preliminary Sensitised Emission FRET Measurements

Following optimisation to maximise sensor expression, we undertook preliminary FRET measurements. FRET snapshots were acquired whereby CFP was excited and CFP emission and YFP sensitised emission were collected, to verify the presence of a FRET reaction (figure-25). The presence of a FRET reaction could not be confirmed where sensor expression was driven by Neuralized as no cells

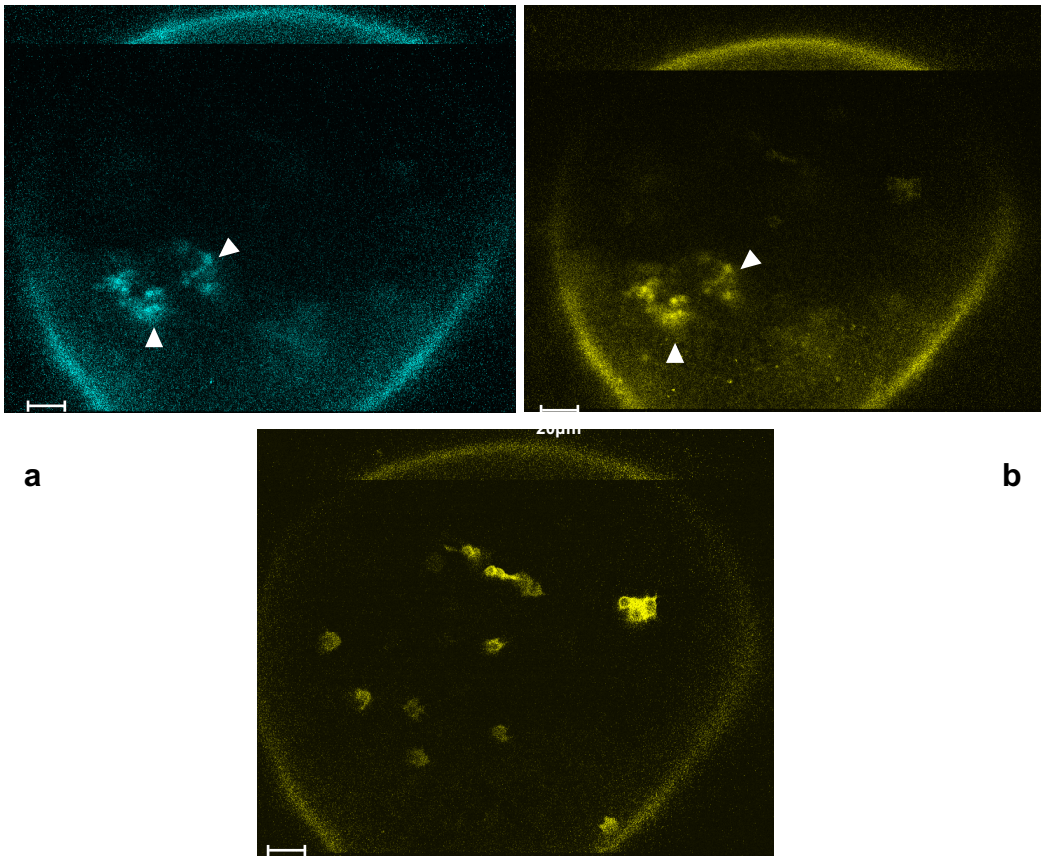

Figure 25- The presence of a FRET reaction could not be confirmed within Neuralized-driven cells. *A snapshot of CFP emission (a) and YFP (b) sensitised emission revealed no neu-camps(epac1)$^{+}$ cells could be visualised. However, a snapshot upon direct YFP excitation (c) acquired in the same field of view revealed the sensor was expressed within some neu-camps(epac1)$^{+}$ cells in the notum. Note the presence of a cluster of bright fat bodies (marked by white triangles) within the CFP emission and YFP sensitised emission images, but not the direct YFP excitation image.*

containing the sensor were visible. Following excitation at the CFP wavelength, CFP emission and YFP sensitised emission were undetectable (figure-25). However, upon performing direct YFP excitation in the same cells within the same field of view after YFP emission was detected, confirming sensor expression within neu-camps(epac1)$^{+}$ cells. It was unclear whether the reason for the absence of a FRET reaction was due to low cAMP concentrations within epithelial cells or further optimisation of the acquisition protocol was required to detect poor sensor expression driven by the weak Neuralized promoter. When the same FRET measurements were undertaken in cells where sensor expression was driven by Pannier, the presence of a FRET reaction was confirmed. Upon excitation of CFP, CFP emission and YFP sensitised emission was detected both in snapshots and within a Z-stack, confirming FRET could be successfully detected throughout the cell in Pannier-driven cells.

The next step was to optimise our acquisition protocol to undertake sensitised emission FRET measurements within cells where sensor expression was driven by Neuralized. In order to maximise the amount of signal detected, we increased pixel dwell time to increase the number of photons detected by halving acquisition speed from 6 to 3. This increased pixel dwell time to 32.97usec. Furthermore, the frame size was decreased from 1024 x 1024 to 512 x 512 and the wavelengths of CFP and YFP detection were broadened to further amplify signal detected.

Upon CFP excitation FRET snapshots recording CFP emission and YFP sensitised emission were obtained, to determine whether the presence of a FRET reaction could be confirmed. CFP emission and YFP sensitised emission were successfully recorded in Neuralized driven pupae; upon direct CFP excitation, CFP emission and YFP sensitised emission were successfully recorded. Next to confirm the optimised protocol could be used to detect the presence of a FRET

reaction throughout the whole cell and within membrane-based protrusions, FRET Z-stacks were acquired as snapshots were unrevealing regarding the presence of FRET within membrane-based protrusions found at different cell depths. This exposed that CFP emission and YFP sensitised emission were very weak within the basal region of Neuralized-driven cells. In particular this impacted the basal protrusions, which were not observed in most Neuralized-driven cells, and intermediate lateral protrusions, which were markedly shorter than they appeared during YFP excitation. Although low signal was still observed within intermediate lateral protrusions, this signal was still decidedly improved in comparison to basal protrusions. Therefore, we decided to focus our attention on taking sensitised emission FRET measurements specifically within the intermediate lateral protrusions in Neuralized-driven cells and whole-cell measurements within Pannier-driven cells, as emission signal for both YFP and CFP were very high within Pannier-driven cells throughout the Z-stack (figure-26,27).

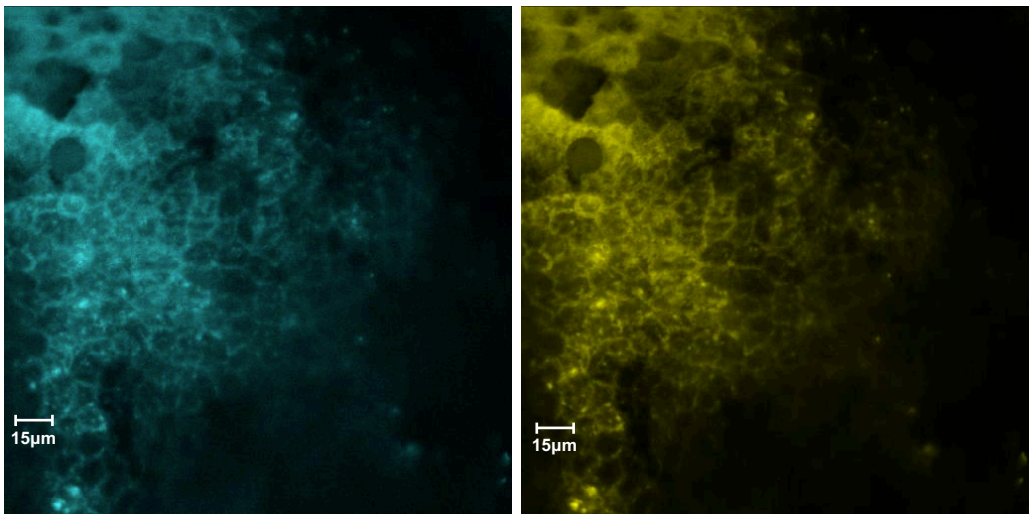

Figure 26- The presence of a sensitised emission FRET reaction was successfully confirmed where sensor expression was driven by the tissue-specific promoter Pannier. *CFP emission (a) and YFP sensitised emission (b) were both successfully recorded throughout the cell, via Z-stack acquired by confocal microscopy. Note the presence of bright fat bodies towards the end of the Z-stack in both the CFP emission and YFP sensitised emission Z-stacks, characterised by bright circles. Brightness and contrast were adjusted using ImageJ to facilitate visualisation*

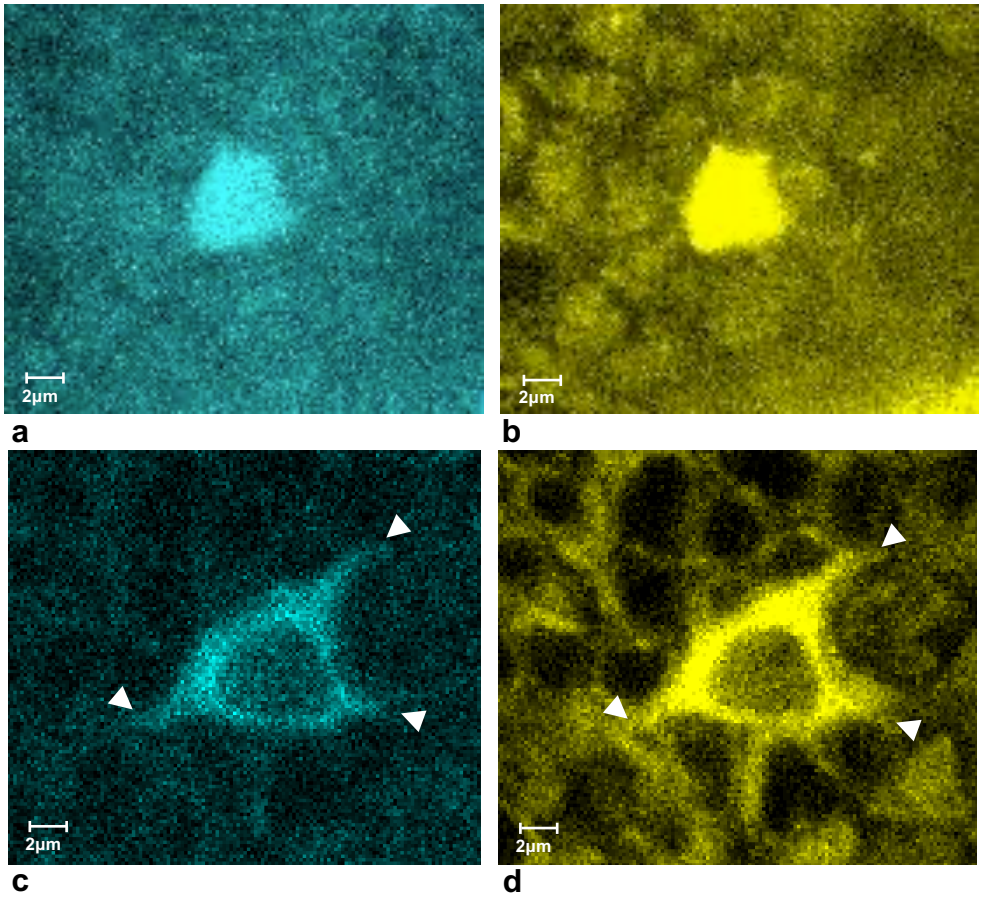

Figure 27- FRET Z-Stacks were limited by high levels of background fluorescence but intermediate-lateral protrusions could be clearly distinguished. *Confocal microscopy Z-stack showing CFP emission (a) and YFP sensitised emission (b) within a neu-camps(epac1)⁺ cell in the notum. Note that it was difficult to distinguish protrusions within the basal region. Intermediate-lateral protrusions (indicated by white triangles) were clearly visible in CFP emission (c) and YFP sensitised emission (d) channels. Brightness and contrast were adjusted using ImageJ to aid visualisation as fluorescence was low intensity.*

However, improved sensor expression was at the cost of elevated background signal within Neuralized-driven cells. Increased pixel dwell time not only increased the amount of signal originating from the cells of interest, but background fluorescence too. Within Neuralized-driven images, the mean grey value of background intensity was roughly 50% of the mean grey value recorded for CFP emission and YFP sensitised emission within neu-camps(epac1)⁺ cells, making distinguishing of membrane-based protrusions from high background noise difficult. The issue of high mean background grey values impacted Pannier-driven cells to a lesser extent as, at a 2 times optical zoom, the whole field of

view contained cells expressing the sensor, therefore little or no background was visible.

Contributing to this elevated background noise, we observed the presence of intense aberrant fluorescence present originating from fat bodies located beneath the epithelial sheet, which was not observed upon direct excitation of YFP but was present upon direct CFP excitation. We therefore concluded that this phenomenon was due to fat body autofluorescence following excitation with a 405 laser- the laser used for CFP excitation. This issue was prevalent within Neuralized-driven images, where cells could be consumed by the bright intensity of fat bodies part way through the Z-stack, making measurement and visualisation of membrane-based protrusions within the basal region impossible. Such bright fat bodies were also present where sensor expression was driven by Pannier, although their presence impacted measurements to a lesser extent as they were not visible in most images (figure-28).

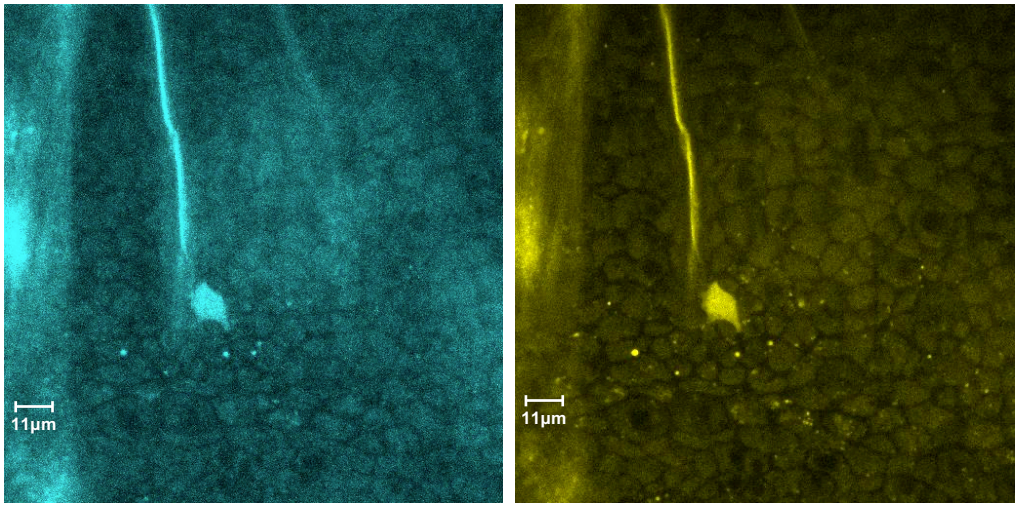

Figure 28- Bright fat bodies were visible within the plane of neu-camps(epac1)⁺ cells where sensor expression was driven by Neuralized. *Fat bodies are visible as bright spheres located towards the end of the Z-stack in both CFP emission (a) Z-stacks and YFP sensitised emission (b) Z-stacks acquired via confocal microscopy. Brightness and contrast were artificially adjusted to aid visualisation in ImageJ.*

Therefore, we continued protocol optimisation to reduce the impact of fat body autofluorescence. CFP can also be excited using a 456 laser but trial of this adaptation yielded low CFP emission therefore was not appropriate for use in FRET experiments. Narrowing of the CFP wavelength to 470-510nm was also unsuccessful; such reduction sacrificed signal compromising emission detection. Despite this continued optimisation, fat body autofluorescence seemed unavoidable. Therefore, the protocol was reverted and care was taken when selecting cells for further experiments to avoid contamination of images by any fat body autofluorescence.

Following optimisation of background subtraction, we used the MARCM system to create clones containing the sensor, driven by the tissue specific promoter Pannier (figure-29). The aim of this was to create

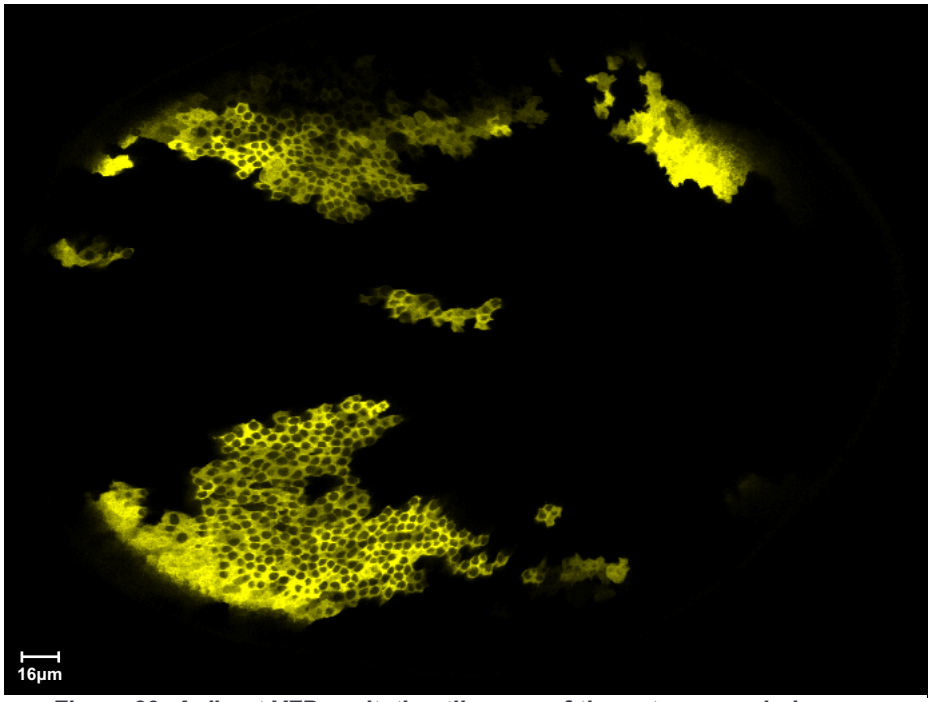

Figure 29- A direct YFP-excitation tile-scan of the notum revealed sensor expression conformed to the expected distribution. *Sensor expression was driven by the tissue specific promoter Pannier, using the MARCM/FLP/FRT system, to create patches of clones expressing the sensor. Images were acquired using confocal microscopy and brightness/contrast were adjusted in ImageJ to aid visualisation.*

patches of tissue expressing the sensor, leaving room for quantitation of mean background grey values aiding background subtraction. Furthermore, generation of clones meant protrusions at edge clones were unobstructed facilitating sensitised emission FRET measurements within membrane-based protrusions. This could be used to corroborate the accuracy of sensitised emission FRET measurements within Neuralized-driven cells. Following generation of clones driven by Pannier, a direct excitation YFP tile-scan was undertaken to confirm the expression pattern which revealed the correct mosaic expression was observable and overall sensor expression was good (figure-29). The presence of a FRET reaction was confirmed by undertaking a FRET Z-stack where CFP was excited and CFP emission and YFP sensitised emission was recorded (figure-30). This revealed the sensor was well expressed throughout the Z-stack, within apical microvilli-like protrusions, intermediate-lateral protrusions and even protrusions found within the basal region, unlike Neuralized-driven cells, albeit at low intensities (figure-31). Furthermore, mean grey values within the clones were one hundred times those within neu-camps(epac1)$^{+}$ cells where sensor expression was driven by Neuralized. Although, mean background values were similar to Neuralized images, this made little difference to the detection of CFP emission and YFP sensitised emission as mean background intensities were approximately 13.3 times greater within clones in comparison to background. Additionally,

the presence of fat body was confirmed but as the clones were much brighter, this made little difference.

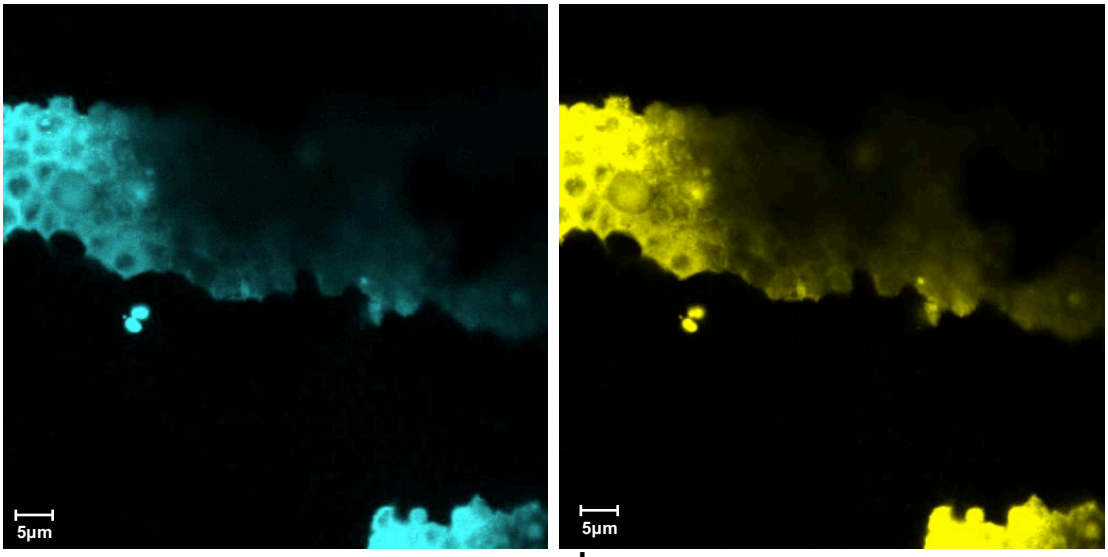

Figure 30- A Z-stack revealed the presence of a FRET reaction throughout the cell in Pannier clones*. The sensor was well-expressed within intermediate-lateral and basal (not visible) membrane-based protrusions. Images were acquired by exciting CFP and recording CFP emission (a) and YFP sensitised emission (b) via confocal microscopy. Brightness and contrast was adjusted to aid visualisation using ImageJ.*

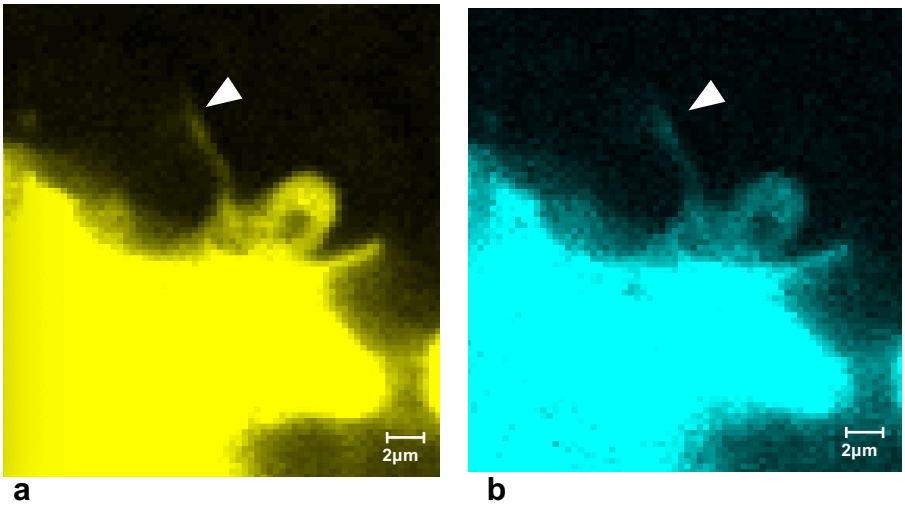

Figure 31- Basal protrusions were visible in Pnr-camps(epac1)$^{+}$ clones. *CFP emission (b) and YFP sensitised emission (a) were recorded following CFP excitation. Basal protrusions are marked with a white triangle. Brightness and Contrast was adjusted using ImageJ to aid visualisation in this figure.*

3.4 Optimisation of Data Analysis and Image Processing Protocol

Following successful optimisation of the sensitised emission FRET acquisition protocol, attention turned to analysis of images generated and extraction of ratiometric FRET measurements. An established protocol, as outlined by Couto et al., was employed and optimised (as described the following sections) to generate a method specifically suited to the data produced from sensitised emission FRET experiments.

3.41 Background Subtraction

One of the biggest barriers to the reproducibility and accuracy of ratiometric sensitised emission FRET measurements is incorrect background subtraction. Given the nature of the low intensity changes of fluorophore emission, correct background subtractions are even more important to either avoid loss of signal or aid differentiation of signal from high background levels. Therefore, we aimed to optimise an accurate protocol for background subtraction for Neuralized-driven and Pannier-driven images.

Initially during background subtraction, images were cropped to remove extraneous slices, not containing the cell of interest. A background ROI was generated by creating a maximum intensity Z-projection and tracing the cell outline. Originally, the background ROI was placed in a consistent position in every image, the top righthand corner, to reduce bias and a single average background value calculated for each channel. This value was subsequently subtracted from each slice in the corresponding channel. However, following background subtraction, Neuralized images were plagued by pixel loss within the cell of interest, suggesting a flaw within the background subtraction procedure. This

raised two questions: is it appropriate to apply a mean background grey value to every slice within the Z-stack and are mean grey values in the top righthand corner physiologically relevant background grey values surrounding the cell of interest? In order to resolve these pressing concerns, we measured five ROIs at different positions within the image, throughout the Z-stack, to determine whether subtracting a single average value measured in a consistent position was appropriate.

We found variance between different ROIs within Neuralized images was a statistically significant effect (YFP $p<0.0243$, CFP $p<0.0001$), indicating significant difference in mean grey values at different positions within each slice. Furthermore, variance between different depths of Neuralized Z-stacks was also found to be a statistically significant effect (YFP $p<0.0001$, CFP $p<0.0008$). Additionally, upon comparing the graphical trend of mean background grey values, in each image, between YFP and CFP emission images, it appeared trends followed markedly different patterns (figure-32).

These results demonstrate that mean background grey values vary significantly at different positions within the image and at different cell depths. Therefore, adaptations were made to the background subtraction process. Background ROIs were placed as close to the cell of interest as possible, avoiding bright fat bodies which could give a false background reading, in order to ensure background subtractions were physiologically relevant to the cell of interest. Where mean background grey values were found to significantly vary within an image, different background values were subtracted for different cells within the same image. This was in lieu of a local threshold, which is currently only supported for 8-bit images within ImageJ. Furthermore, mean background grey values were measured throughout the stack and the corresponding mean grey value subtracted at each slice,

instead of an average value subtracted from all slices, as described by (Couto et al., 2017).

Where this was replicated in cells where sensor expression was driven by Pannier see difficulty in background subtraction was encountered as there were no regions within the image where no cells were present. Therefore, background could not be measured or subtracted. Thus, it was decided that the MARCM system should be employed to create a mosaic of clones expressing the sensor. This would leave ample space where no cells containing the sensor were present to facilitate accurate background quantification and subtraction. As mean background intensities were approximately 13.3 times lower than clone fluorescence, background subtraction was of lower significance. Therefore, the background ROI was placed as close to clones as possible without impinging on protrusions.

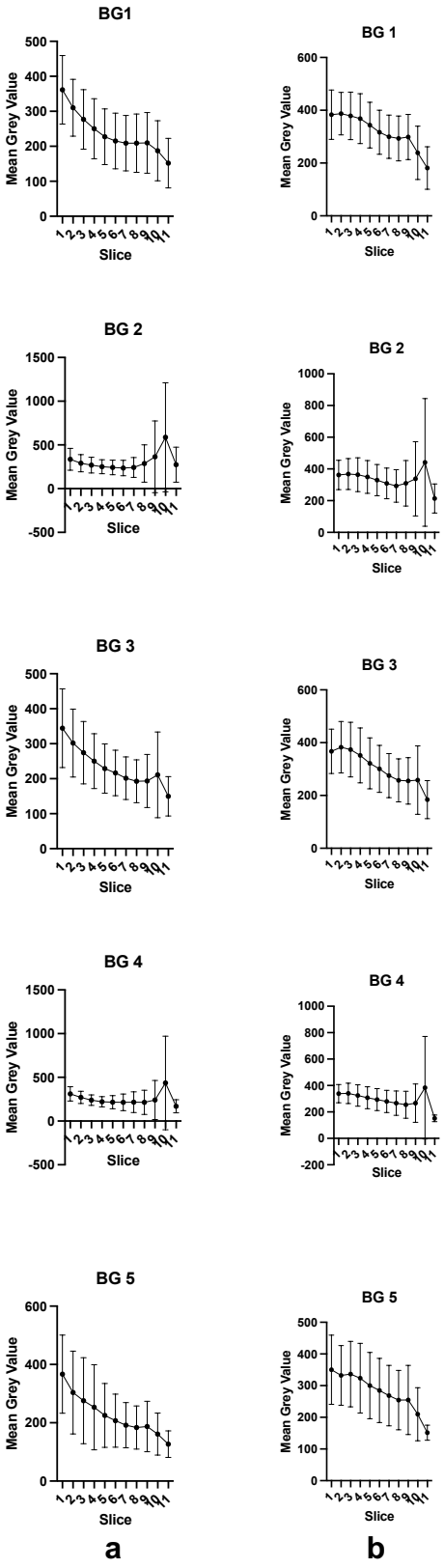

Figure 32- Variation in mean background intensity at different cell depths and at different positions within the image was statistically significant. *Mean background grey values were quantitated throughout the Z-stack at five different positions within Neuralized-driven cells in the CFP emission (a) and YFP sensitised emission channels (b). Average background values are plotted. Two-Way ANOVA revealed statistically significant variation between background position (YFP p<0.0243, CFP p<0.0001) and at different points within the Z-stack (YFP p<0.0001, CFP p<0.0008). n=10 where p<0.05 was considered*

3.42 Calculating Optimal Thresholds

The next challenge faced within the image processing procedure was regarding thresholding. Application of a global threshold using the 'Threshold' tool in ImageJ, maintains the integrity of any signal within the cell of interest and protrusions, while minimising background. Although a background subtraction was undertaken to remove noise, it is impossible to remove all background fluorescence from an image. Consequently, the cell of interest was not visible within the subsequent ratio image, created by dividing the YFP sensitised emission image by the CFP emission image, making measurement of FRET ratios impossible. Therefore, setting a global threshold around the cell of interest, outside which all pixels are converted to NaN (Not a Number, where pixels have no assigned numeric value therefore appear as black), allows visualisation of the cell of interest and facilitates measurement of FRET ratios within membrane-based protrusions. Therefore, it was important to determine a specific threshold method which enabled accurate and reliable outlining of the cell of interest. Initially, the automatic global thresholding scheme within ImageJ was selected and used to generate separate average YFP and CFP threshold values. Upon analysing the resultant images, it was clear that applying average threshold values to cells of differing intensities was a flawed approach. Where cells were of a higher intensity, too little background fluorescence was removed complicating protrusion identification. The inverse was true for lower intensity cells; the removal of too much background fluorescence compromised protrusion fluorescence. As cells driven by Neuralized possessed varying levels of fluorescence intensity, we decided that a different approach was required. Furthermore, images in which sensor expression was driven by Pannier also experienced varying fluorescence intensity between images. This issue was less pronounced between individual cells in Pannier images and Pannier was a more reliable promoter and appeared to drive consistent sensor expression between cells. This

prompted us to adapt our approach. Thus, a single threshold was applied for each pupa where optimal threshold value of the lowest intensity cell within the image was applied, so as not to unfairly penalise lower intensity cells. However, this approach was also unsound as too little background fluorescence was excluded from high intensity cells, making protrusion identification difficult.

In addition to altering the thresholding approach, we also investigated the use of different thresholding schemes. Using the 'Try All' global threshold function in ImageJ to generate a compilation of the different thresholds available, we tested ten images (five where sensor expression was driven by Neuralized and five where sensor expression was driven by Pannier) to determine the optimal thresholding scheme for our data set (figure-33, figure-34). Based on this analysis, the top

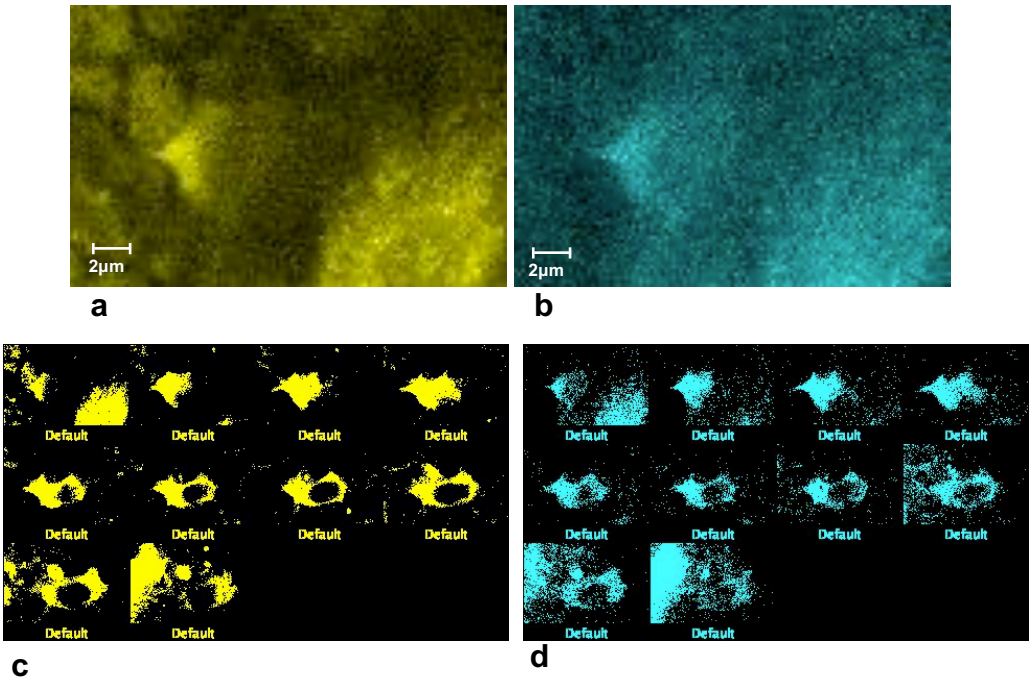

Figure 33- The three optimal thresholds for background subtracted Neuralized YFP sensitised emission and CFP emission images were determined to be Huang, Mean and Li. *Image compilations were generated using the 'Try All' function within ImageJ Automatic Thresholding showing computed thresholds at each slice for each scheme, thresholds were determined using the stack histogram. The most accurate thresholds were determined by comparing each threshold compilation to the original YFP sensitised emission (c) and CFP emission images (d). Original YFP sensitised emission (a) and CFP emission (b).*

three thresholding schemes for both Pannier and Neuralized driven sensor expression were revealed to be Mean, Li and Huang (table-17). Ultimately, the Huang thresholding scheme was selected due to its ability to distinguish objects within images where fluorescence intensity is greatly varied i.e. where there are objects of low intensity and high intensity. This was ideal for our dataset as, in Neuralized-driven images, cells were of much lower intensity than background fluorescence and vice versa in Pannier-driven images.

Table 17- The top three optimal thresholding schemes for Neuralized and Pannier pupae.
Optimal thresholding scheme was determined using the 'Try All' Threshold function in ImageJ. The top best fitting threshold was selected for Pannier and Neuralized. n=5 pupae.

Pannier		**Neuralized**	
Huang	Mean	Mean	Mean
Mean	Huang	Li	Huang
Li	Li	Huang	Li

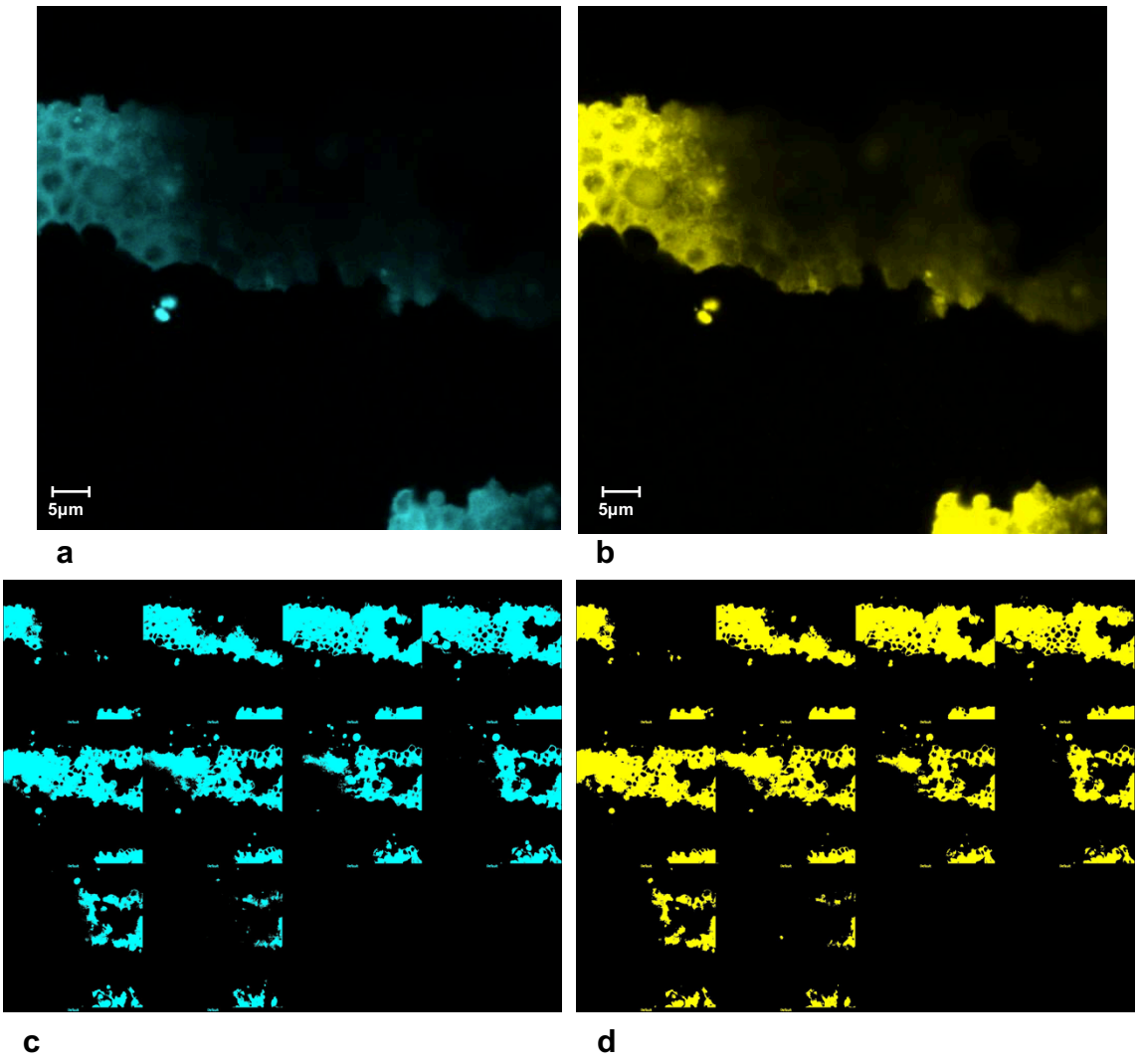

Figure 34- The three optimal thresholds for background subtracted Pannier YFP sensitised emission and CFP emission images were determined to be Huang, Mean and Li. *Image compilations were generated using the 'Try All' function within ImageJ Automatic Thresholding, thresholds were determined using the stack histogram. The most accurate thresholds were determined by comparing each threshold compilation to the original YFP sensitised emission (c) and CFP emission images (d). Original CFP emission (a) and YFP sensitised emission images (d).*

Therefore, it was imperative that we discover a methodology which did not penalise lower intensity cells based on threshold values skewed by higher intensity cells. Therefore, using the global thresholding tool within ImageJ, optimal threshold values were computed for all images and used to split images into groups. A single, more relevant threshold value was applied to all images within the group with the aim of creating more accurate thresholds (figure-35, figure-36).

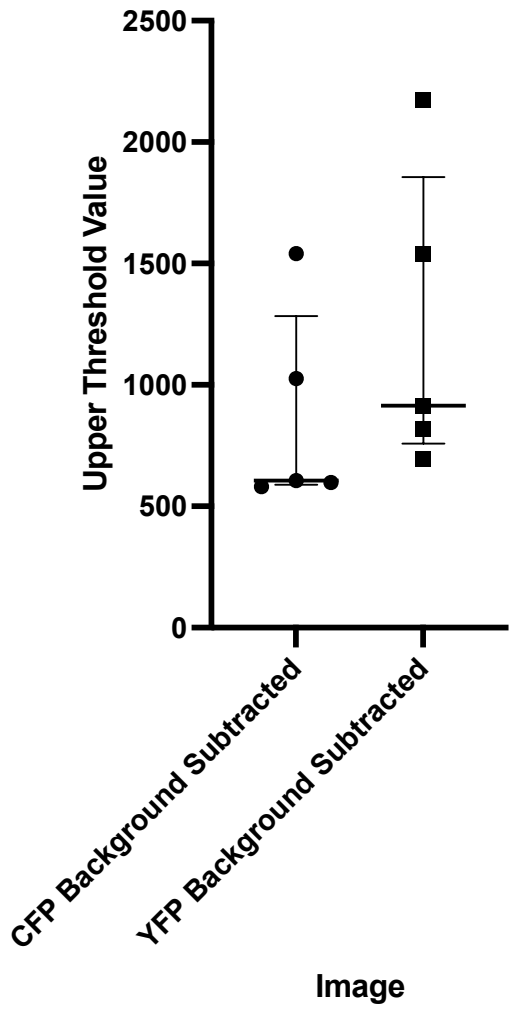

Figure 35- The optimal Huang thresholds for Pannier-driven clones containing the sensor. *Optimal thresholds were determined using the stack histogram to generate a global threshold via the ImageJ 'Threshold' function in CFP emission and YFP sensitised emission images. Sensor expression was driven to the notum using the tissue specific promoter Pannier using the MARCM/FLP/FRT system.*

Visually, an improved contrast was observed within ratiometric FRET images generated using the new threshold groupings. New threshold groupings proved, in general, better at accentuating differences in high and low cAMP concentrations within the cell and protrusions in the subsequent ratiometric FRET images, when encoded with a 'fire' LUT. Furthermore, in some images pixel ratio information loss was reduced,

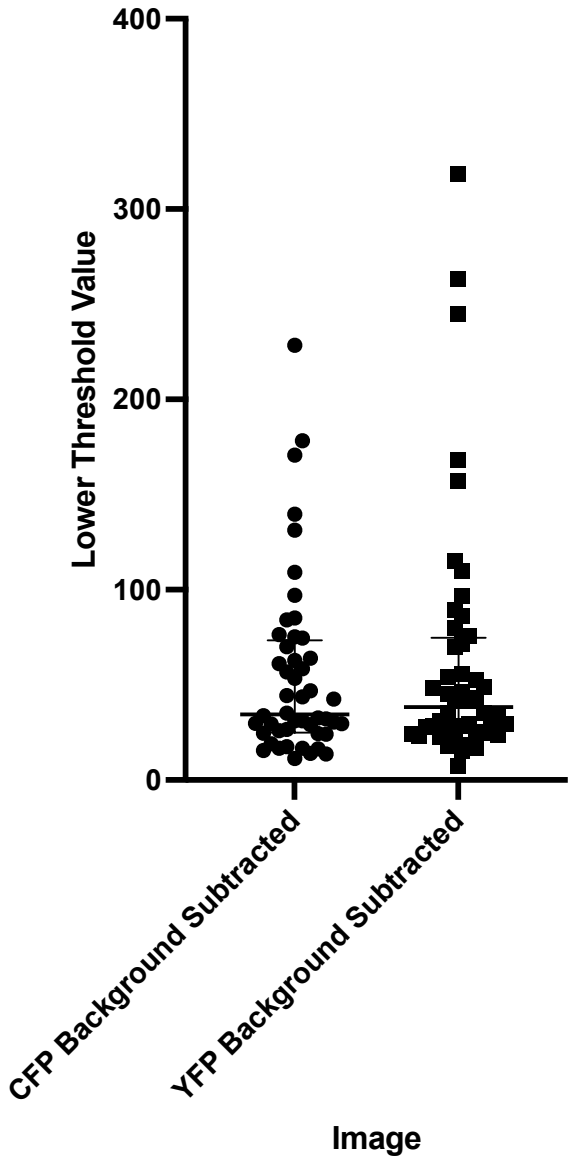

Figure 36- The optimal Huang thresholds for neu-camps(epac1)$^{+}$ cells containing the sensor. *Optimal thresholds were determined using the stack histogram to generate a global threshold via the ImageJ 'Threshold' function in CFP emission and YFP sensitised emission images. The sensor was expressed using the GAL4-UAS system and sensor expression to the notum driven by the tissue specific promoter Neuralized.*

although this problem still persisted in other images. Upon further investigation, it was discovered that pixels present within the CFP channel with no corresponding pixel present in the YFP channel at the same spatial coordinates, were automatically set to NaN in the ratiometric FRET image by ImageJ following image division. Thus, we

pinpointed ratio pixel loss within protrusion tips to over-thresholding of the YFP channel.

Despite adaptations to the thresholding process as described above, the issue of key pixel exclusion at protrusion tips remained in some ratiometric FRET images. Upon further inspection of images where a threshold had been applied, it was discovered that CFP images appeared to possess a greater number of pixels which were not present at the corresponding spatial coordinates within their accompanying YFP image or ratiometric FRET image. This led us to consider the prospect that an absence of pixels within the tips in a single channel could be the reason underpinning pixel loss within protrusion tips of ratiometric FRET images. As changes in YFP sensitised emission are much greater than alterations in CFP emission, overthresholding of YFP could lead to underestimation of FRET ratios. Thus, to combat these two issues, we created ratio images where a threshold was only applied to the CFP image. Quantification of FRET ratios within the same ROIs as measured in revealed no alteration in ratio in comparison to images where both a CFP and YFP threshold was applied. Additionally, application of only a CFP threshold did nothing to solve the issue of pixel loss within the protrusion tip.

Subsequent digital investigation revealed that a lack of pixels in the CFP channel where pixels in the corresponding position were present in the YFP channel was the cause of pixel loss within protrusion tips. In fact, this issue was only prevalent in two images. However, it was unclear whether the presence of additional pixels in the YFP channel was due to background or lack of signal in channel CFP. Therefore, the protocol was adapted to accommodate this fact. The protrusion had to be present in both the CFP and YFP channels to satisfy inclusion within the data set.

Next, to identify whether the application of thresholds according to our method led to distortion of FRET ratios, mean grey values were measured within all intermediate-lateral protrusions of ten Neuralized-driven cells before and after threshold application. The aim of this was to determine whether mean grey values within CFP emission and YFP sensitised emission images remained the same after threshold application, thus giving an indication whether thresholding was accurate and reliable. Following measurement of mean grey values within the cytosol, base, middle and tip of intermediate-lateral protrusions, minimal differences in FRET ratio were recorded. In fact, Two-Way ANOVA revealed no difference between column means and indicated that variation between mean grey value within the cytosol, base, middle or tip before and after threshold application was not statistically significant (figure-37). Nevertheless, slight difference in mean grey

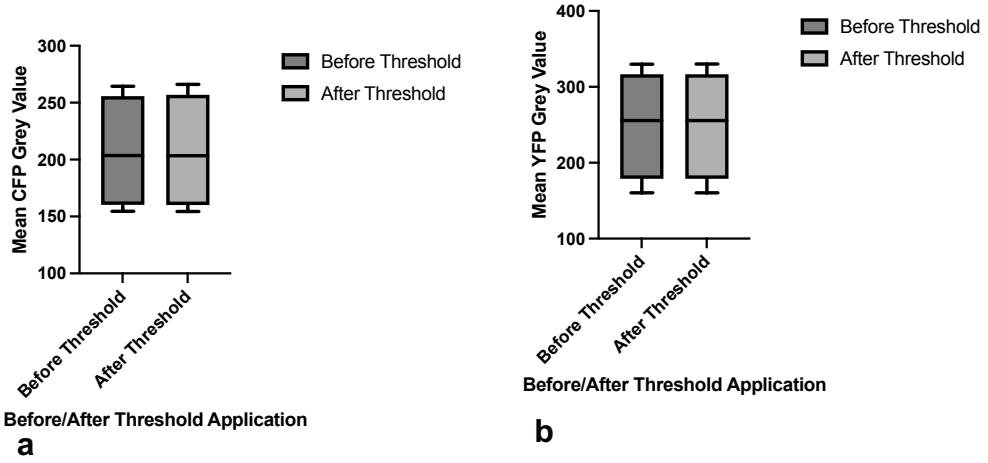

Figure 37- There was no difference in mean grey value within the cytosol, base, middle or tip of CFP emission (a) and YFP sensitised emission (b) images following threshold application. *Mean grey values were quantitated within the cytosol, base, middle and tip of intermediate-lateral protrusions in Neuralized-driven images before and after threshold application, using ImageJ. Two-Way ANOVA revealed no statistically significant difference between column means or between row values before and after threshold application (n=10, where statistical significance was set to p<0.05).*

value was recorded within the cytosol of two images, although differences were very small. Subsequent investigation of this effect exposed that differences in ROI area were responsible for such differences. As this conveyed only very minimal differences in cytosolic

mean grey value within a small number of images, we decided not to adapt the thresholding method further.

3.43 Filtering

Noise corruption in fluorescent microscopy images is a well-documented issue present in every image. Within the image, there are two types of noise: photon noise originating from emission and detection of fluorescence, and read noise caused by errors in photon quantification. Thus, we aimed to correct for any noise within images by applying a 3x3 smoothing filter as recommended by Couto et al(Couto et al., 2017). A 3x3 smoothing filter works by averaging the pixel value within the neighbouring 3x3 area. The effect of this is noise reduction, with only small losses in spatial information. We applied a 3x3 smooth filter, using the ImageJ ‘Smooth’ function, and quantitated FRET ratios within a defined ROI before and after filter application.

Upon analysis of the trend, it appeared quite similar between smoothed and non-smoothed images from cytosol to middle. However, the decrease from middle to tip was more pronounced within non-smoothed images in comparison to smoothed images. Furthermore, Two-Way ANOVA revealed a statistically significant difference in FRET ratios between smoothed and non-smoothed images (**p=0.0045) within ten Neuralized cells (figure-38). This indicates that application of a smooth filter could drastically alter FRET ratios quantitated, suggesting that such a filter, while correcting for noise, could lead to inaccurate characterisation of FRET ratio gradients within cells of interest. Therefore, we decided not to apply any filters to prevent inaccuracies in quantification of ratios.

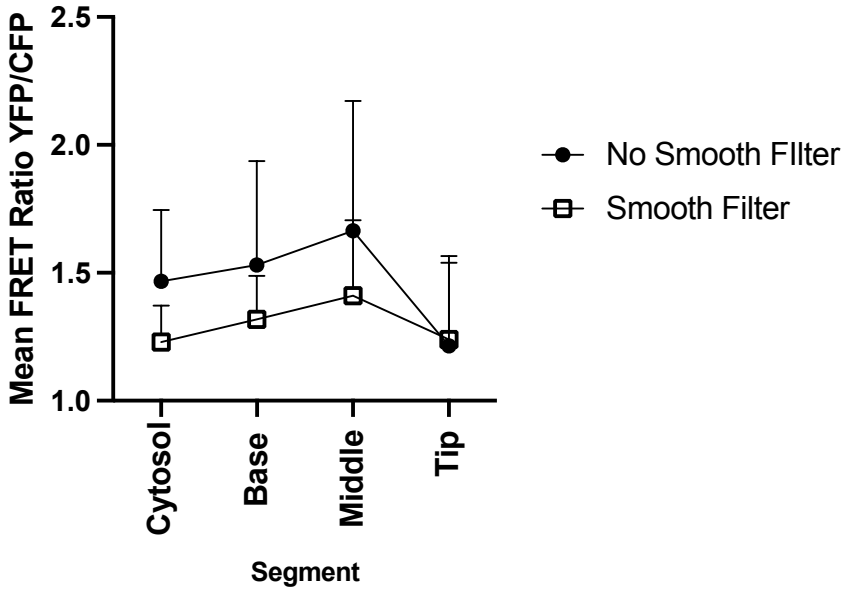

Figure 38- Mean FRET was significantly different between ratio images between smoothed and non-smoothed images. *FRET ratios were quantitated within the cytosol, base, middle and tip of smoothed and non-smoothed images, using a 3x3 smooth filter within ImageJ. Ratios were quantitated using the measure function, also within ImageJ. Although the trend from cytosol to middle appeared the same, the decrease between middle and tip was more pronounced where no smooth filter was applied in comparison to smoothed images. A statistically significant difference was detected between smoothed ratios and non-smoothed ratios (n=10, **p=0.0045) using Two-Way ANOVA, where p<0.05 was considered statistically significant.*

3.44 Automation of Ratio Image Generation

Having established the basic image processing protocol to generate a ratiometric FRET image, attention turned to automation. As the process was quite involved, we aimed to develop an ImageJ Macro to generate ratio images quickly. It proved too complicated to create a Macro which undertook background subtraction. Therefore, we focussed our attention on creating a Macro which undertook image conversion to 32-bit, threshold application, creation of ratio image and encoding of pixels with a fire LUT to aid visualisation.

In order to validate our method, we compared FRET ratios within the cytosol, base, middle and tip of ratio images generated using the MACRO and ratio images created manually. We found no difference in ratio at any point, within the membrane-based protrusion or cytosol, between the Macro ratiometric FRET image and manual ratiometric FRET image. All ratios were completely identical at all points. Thus, we successfully demonstrated our Macro could be employed to create ratiometric FRET images.

3.45 Taking FRET Ratio Measurements in ImageJ

To assess FRET ratios gradients within intermediate-lateral membrane-based protrusions, mean FRET ratios were assessed at different points within the protrusion: the base middle and tip. These measurements were compared to the cytosol, to assess the compartmentalisation of cAMP signals within the cell. This was only undertaken for cells where sensor expression was driven by Neuralized. As protrusions extended throughout multiple slices, FRET ratios were grouped based on cell depth within the intermediate regions and, where protrusions extended throughout multiple slices, each slice was treated as individual replicate. Analysis revealed there statistically significant variance between the base and tip (p=0.0339) and between the middle and tip (p=0.0408) at 4um cell depth, indicating an increased cAMP concentration (figure-39). Additionally, statistically significant variance

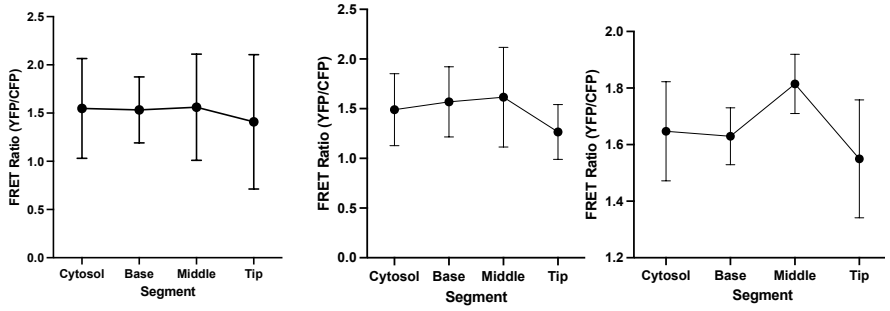

Figure 39- The trend in FRET ratio within different compartments at different slices in neu-epac1(camps)⁺ cells. *FRET ratios were quantified in the cell cytosol, and protrusion base, middle and tip of neu-epac1(camps)⁺ cells within intermediate-lateral protrusions at slice 3 (a), slice 4 (b) and slice 5 (c). There was a statistically significant higher relative basal cAMP concentration between the tip vs base in slice 4 (0.0339*), middle vs tip in slice 4 (0.0408*) and middle vs tip in slice 5 (0.0407*) using One-Way ANOVA. Statistical significance was set to p<0.05. See methods for samples sizes.*

was detected between the middle and tip at 5um (p=0.0407). Overall, the trend at slice three showed little increase or decrease in FRET ratio along the membrane-based protrusion and in comparison to cytosol ratios. This was also true at 4um cell depth and, although a slight decrease of FRET ratio within the tip was observed, this was not statistically significant. At 5um cell depth, FRET ratio within the middle

of the membrane-based protrusion was increased, indicating a decreased cAMP concentration. However, variance in ROI area was also detected throughout the protrusion. Upon investigation, it was discovered that this was due to pixel loss within the protrusions decreasing the areas. Furthermore, upon inspection of the ratio images, there appeared to be great variability within the cytosol ROI. Therefore, the decision was taken to increase the ROI area within the cytosol to increase the accuracy of the measurements. Additionally, ROIs within the membrane-based protrusions were decreased to 0.172μm^2; this new area was approximately the width of the protrusions preventing ROI area variance. Moreover, upon closer inspection of images, the membrane-based protrusion tip in many images was not present in every slice, leading to inaccurate measurements. Protrusions were grouped based on how far below the apex protrusions were situated i.e. protrusions 3μm below the apex were grouped together, protrusions found 4μm below the apex were grouped together. Given that protrusions can extend throughout multiple slices and begin at different depths, this is not appropriate method of grouping as measurements are incomparable(Couto et al., 2017). Furthermore, sometimes protrusions can appear to be overlapping in the Z-axis, therefore it is difficult to identify whether a protrusion extends throughout several slices in the Z-dimension or separate protrusions are detected. Accordingly, the method was adapted so FRET ratios were only quantitated within the slice where the protrusion tip was visible. This prevented misattribution of the FRET ratios to the tip and ensured that each protrusion was treated as an individual replicate.

Chapter 4: Preliminary Results

4.1 cAMP Gradients

The differential activation of small GTPases of the Ras superfamily, specifically Rac, Cdc42 and RhoA, is known to modulate protrusion dynamics in living cells(Davidson and Wood, 2016, Etienne-Manneville and Hall, 2002, Georgiou and Baum, 2010, Hall, 1998, Kadzik et al., 2020). cAMP is a second messenger which may mediate the spatial and temporal specificity of signals derived from Rac, Rho and Cdc42 activation via downstream effectors PKA and EPAC. Previous studies have correlated the inhibitory effect of PKA phosphorylation of RhoA with distinct changes in cellular morphology, including cell body rounding(Soriano et al., 2021). Moreover, PKA phosphorylation of adaptor protein CIP4 was correlated with increased actin-based migration(Lin et al., 2003). What remains unclear is the precise locality of these signalling events within membrane-based actin protrusions and spatial correlation with subcellular cAMP gradients. Therefore, we aimed to measure relative cAMP concentrations in the cytosol and within the protrusion base, middle and tip, to determine whether a cAMP gradient was present within the intermediate-lateral membrane-based protrusions. Therefore, we took advantage of a FRET-based cAMP biosensor to undertake ratiometric sensitised emission FRET measurements with high spatial resolution, in a polarised 3D epithelial sheet. This provided real-time information regarding cAMP gradients within membrane-based protrusions.

4.11 cAMP Gradients Within neu-camps(epac1)$^{+}$ Cells of the Notum

The Neuralized promoter was utilised to drive sensor expression to well-spaced epithelial cells within the notum, facilitating the

measurement of cAMP gradients within unobstructed intermediate-lateral membrane-based protrusions. Quantification of ratios revealed a statistically significant decrease in FRET ratio from the protrusion middle to protrusion tip (p=0.0004 ***) and from the protrusion base in comparison to protrusion tip (p=0.012 **), within 43 protrusions of 18 animals, as assessed by parametric One-Way ANOVA with Tukey's Multiple Comparisons (figure-40). Such a decrease in FRET ratio

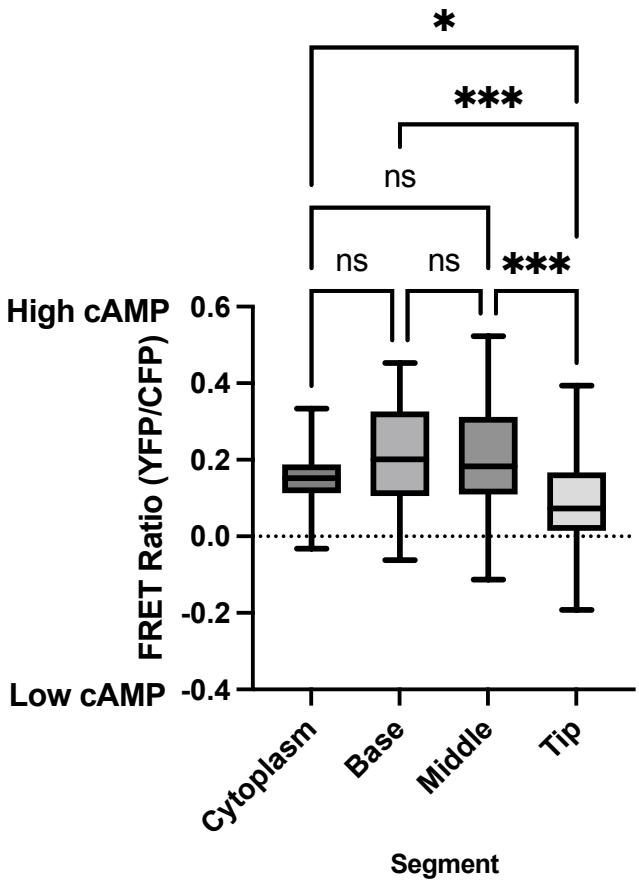

Figure 40- There is a decrease in FRET ratio indicating an increase in cAMP from the base to tip of intermediate-lateral membrane-based protrusions. *Sensor expression was driven to SOP cells in the notum by tissue specific promoter Neuralized. FRET ratios were quantitated in the base, middle, tip and cytosol, where a low FRET ratio indicated a high cAMP concentration. Parametric One-Way ANOVA was undertaken with Tukey's Multiple Comparisons, where statistical significance was set to p<0.05. (Base vs tip p = 0.0012 **, middle vs tip p = 0.0004 ***) (n = 20 cells, 43 protrusions, 43 tip measurements, 30 middle measurements, 42 base measurements, 43 cytosol measurements, 18 animals)*

corresponded to an increase in relative cAMP concentration; a higher cAMP concentration was detected within the protrusion tip vs middle and within the protrusion tip vs base. These results indicate that cAMP gradients could be present within intermediate-lateral membrane-based protrusions, with the highest relative cAMP concentrations recorded in the protrusion tip.

4.12 cAMP Gradients Within Epithelial Cell Clones

Following the discovery that relative cAMP concentration was elevated in the tip of membrane-based intermediate lateral protrusions, we took advantage of the FLP/FRT/MARCM system to generate clones containing sensor expression driven by the tissue specific promoter Pannier. This facilitated creation of patches of clones, where edge clones possessed unobstructed intermediate-lateral membrane-based protrusions, in which ratiometric FRET measurements could be taken to determine whether such cAMP gradients were also present within these cells. Quantification of FRET ratios within the cytosol and protrusion base, middle and tip demonstrated that there is no detectable change in FRET ratio between any segment of 25 intermediate-lateral membrane-based protrusions within 5 animals, as assessed by parametric One-Way ANOVA with Tukey's multiple comparisons (figure-41). In fact, FRET ratios remained relatively constant throughout protrusions and comparatively to cell cytosol. This indicated that relative cAMP

concentrations remained constant throughout membrane-based intermediate lateral protrusions, an observation also true in comparison to cell cytosol. These results show a distinct dissonance from results obtained within neu-camps(epac1)$^{+}$ cells, where sensor expression was

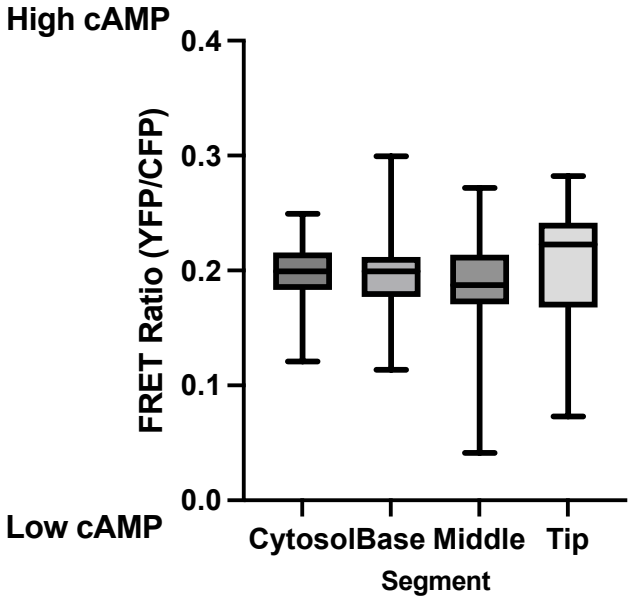

Figure 41- There is no change in FRET ratio, therefore no significant change in cAMP concentration throughout the protrusion and compared to cytosolic FRET ratio. *Sensor expression was driven to clones in the notum by tissue specific promoter Pannier using the FLP/FRT/MARCM system. FRET ratios were quantitated in the base, middle, tip and cytosol, where a low FRET ratio indicated a high cAMP concentration. Parametric One-Way ANOVA was undertaken with Tukey's Multiple Comparisons, where statistical significance was set to $p<0.05$. (n = 22 cells, 25 protrusions, 43 tip measurements, 30 middle measurements, 42 base measurements, 43 cytosol measurements, 5 animals*

driven by the tissue specific promoter Neuralized, and indicate relative cAMP levels remain constant throughout the protrusion and in comparison to the immediate cell cytosol.

4.2 Controls

4.21 Pixel Intensity Addition

Differences in FRET ratio in well-spaced epithelial cells (driven by Neuralized) between the protrusion tip and cytosol appeared promising. However, it was unclear whether such FRET ratio alterations were not an artefact of the image processing process. We artificially increased YFP intensity and created new ratio images. An increase in YFP intensity should be accompanied by a corresponding increase in FRET ratio, thus demonstrating that our methodology could successfully detect changes in FRET ratio and that alterations in FRET ratio were not an artefact of image processing.

We found that FRET ratio within ratiometric FRET images created using the altered pixel values did indeed increase substantially in comparison to original ratios quantitated within the same defined ROI using a Wilcoxon Matched Pairs Signed Rank test (n=10, p=0.0001***) (figure-42). This finding provides validation that our image processing and ratio quantification does in fact allow changes in cAMP to be detected and further corroborates the notion that any changes in FRET ratio are due to differences in cAMP concentration, rather than an artefact of data analysis protocols.

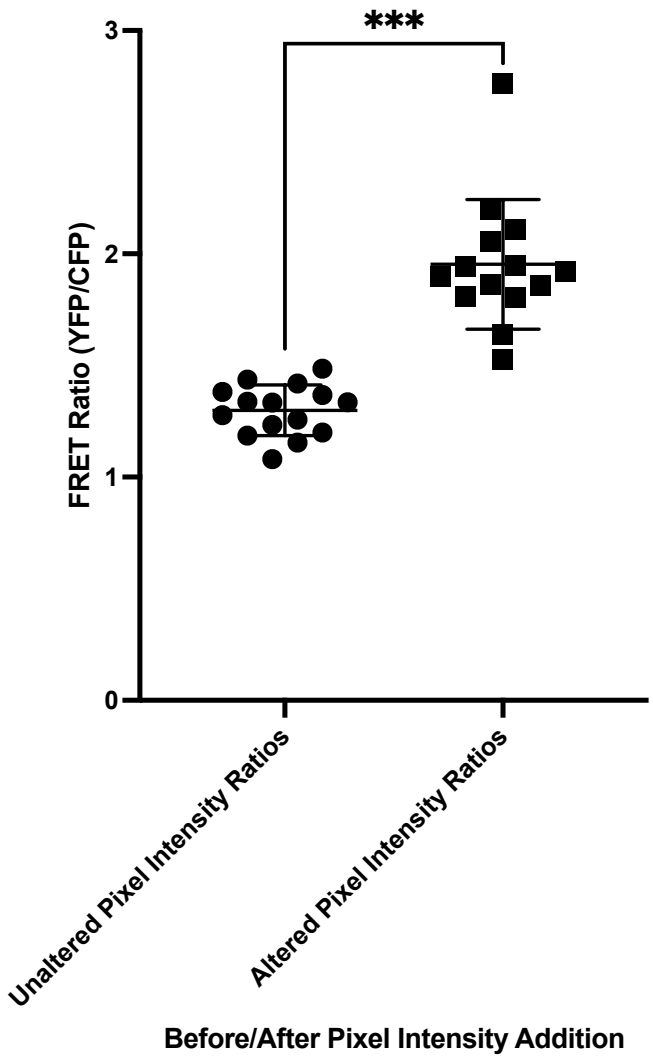

Figure 42- Artificial addition of YFP pixel intensity increases FRET ratio. FRET ratios quantified within the same defined ROI in normal ratiometric FRET images and ratiometric FRET images where YFP pixel intensity was artificially increased using ImageJ. n = 15 cells from y animals. Two-tailed Wilcoxon-Matched Pairs Signed Rank Test was undertaken to ascertain statistical significance and P values are indicated on the graph. P>0.05 was considered not statistically significant, *P<0.05, **P<0.01, ***P<0.001, ****P<0.0001.

4.22 Photobleaching Control

One of the biggest limitations of confocal microscopy is the effect of photobleaching. As this technique employs high intensity lasers, signal degradation can occur over time, especially if scan times are longer. Total scan times in some cases reached up to eighteen minutes, therefore, the possibility of photobleaching compromising signal integrity and creating misleading sensitised emission FRET ratios was concerning. If photobleaching is found to be a statistically significant effect, corrections can be undertaken to minimise the impact on ratiometric FRET measurements(Börner et al., 2011).

In order to determine whether photobleaching was exerting a statistically significant effect on ratiometric FRET measurements, we quantitated FRET ratios within a defined cytosolic ROI throughout the intermediate region. As our overall aim was to quantitate cAMP gradients within intermediate-lateral protrusions, cytosol measurements were only undertaken within the intermediate region to examine the effect of photobleaching upon any measurements undertaken at this cell depth. As YFP is more vulnerable to photobleaching than CFP, we examined the effect of photobleaching upon YFP sensitised emission(Börner et al., 2011). Cytosolic FRET ratio should remain relatively constant throughout the Z-stack, therefore any alterations in ratio could indicate photobleaching is occurring within samples. It can be assumed that the effect of photobleaching is equal at different positions within the image at a particular plane, we concluded that the effect of photobleaching in the cytosol would be identical to the effect within the actin membrane-based protrusions within a particular plane. Additionally, depending on the image acquisition (i.e. top to bottom or bottom to top), some slices could be exposed to the intense laser for longer periods than other slices increasing the effect of photobleaching at that particular plane. As our images were acquired from top to bottom, this was deemed to not be a consideration.

After measuring mean cytosol grey throughout the intermediate region, no statistically significant difference in FRET ratio between any slices was detected, where sensor expression was driven by Neuralized or Pannier. Tukey's multiple comparisons, undertaken on Neuralized data, and an Unpaired T-Test, undertaken on Pannier data, revealed no statistical significance (table-18).

Table 18- Significance P values upon Tukey's Multiple Comparisons between cytosolic cAMP ratios at different depths of the intermediate region. *Significance was set to p<0.05, there was no statistically significant difference in cytosolic cAMP FRET ratios between any Z-stack slices in the intermediate region.*

Comparison	***Neuralized P Vale***	***Pannier P Value***
Slice 1 vs Slice 2	0.9947	0.0903
Slice 1 vs Slice 3	0.0909	N too small
Slice 1 vs Slice 4	0.1521	N too small
Slice 2 vs Slice 3	0.1151	N too small
Slice 2 vs Slice 4	0.0641	N too small
Slice 3 vs Slice 4	0.9999	N too small

Where sensor expression was driven by Neuralized, cytosolic ratios remained quite constant throughout the intermediate region, although Pannier-driven clones experienced a slight increase in variation (figure-43, figure-44). It should be noted that insufficient sample size limited comparison to the first two slices of the intermediate region within Pannier clones.

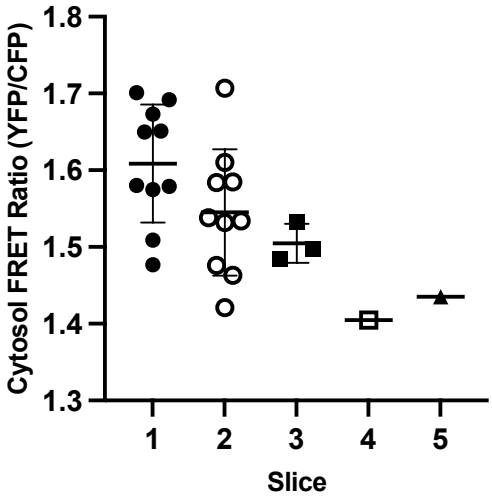

Figure 43- There no statistically significant difference in FRET ratio within the cytosol at different cell depths where sensor is expressed in clones. *FRET ratio within the cytosol was quantitated at different slices throughout the Z-stack using the 'Measure' function in ImageJ. Expression was driven by Pannier using the FLP/FRT/MARCM system to create clones expressing the sensor. Parametric paired ANOVA with Geisser-Greenhouse correction, (multiple comparisons) where statistical significance is set to $p<0.05$. ($n = 10$ cells)*

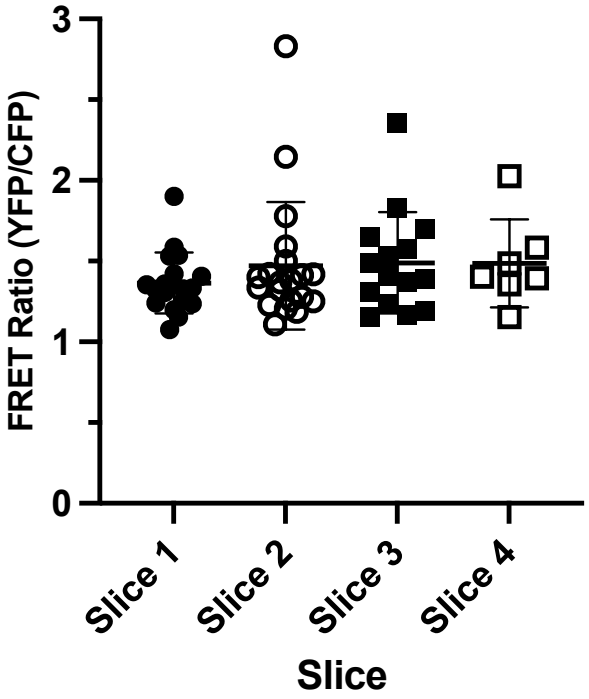

Figure 44- There no statistically significant difference in FRET ratio within the cytosol at different cell depths where sensor expression was driven by promoter Neuralized. *FRET ratio within the cytosol was quantitated at different slices throughout the Z-stack using the 'Measure' function in ImageJ. Expression was driven to the notum by promoter Neuralized by the GAL4-UAS system. Parametric paired ANOVA with Geisser-Greenhouse correction, (multiple comparisons) where statistical significance is set to $p<0.05$. ($n = 20$ cells)*

4.23 Acceptor Photobleaching

Having successfully detected cAMP gradients within intermediate-lateral membrane-based protrusions, we needed to confirm that any alteration was due to a FRET reaction occurring and not as a result of CFP spectral bleedthrough. YFP sensitised emission could be recorded as artificially higher due to cross-detection of CFP emission, creating larger misleading ratiometric FRET measurements. Furthermore, it has been recorded that 50-90% of CFP emission will also be recorded within the YFP sensitised emission channel, indeed there is cross-excitation of YFP by 436nm light of 5-10%, thus artificially inflating 'true' YFP sensitised emission (Börner). Therefore, preliminary acceptor photobleaching experiments were undertaken. The aim of these experiments was to bleach the acceptor (YFP) to 90% and observe any alterations in CFP emission and YFP sensitised emission, as residual fluorescence would be due to spectral bleedthrough of CFP into the YFP channel, not the presence of a FRET reaction. As YFP underwent extensive photobleaching, it should no longer be able to act as the acceptor. Therefore, CFP emission should increase, as it can no longer transfer its energy to excite YFP, and YFP sensitised emission should decrease accordingly. Any remaining YFP sensitised emission is due to spectral bleedthrough of CFP, as there is spectral overlap between YFP and CFP wavelengths.

The first step was to establish a photobleaching protocol using confocal microscopy. Initially, two Z-stacks using Pannier-driven cells were undertaken prior to acceptor photobleaching to determine average baseline values for YFP emission, CFP emission and YFP sensitised emission. However, given that averaging was set to two, this was deemed to be unnecessary therefore the number of Z-stacks prior to photobleaching was dropped to one. During the first preliminary experiments, iterations (i.e. the number of bleaching scans) were set to three. However, this was not strong enough to bleach the acceptor.

Therefore, iterations were increased to ten. This was not strong enough to induce sufficient photobleaching. An increase of iterations to 40, in combination with an increase in pixel dwell time to 32.97usec and laser power to 100%, was strong enough to induce a 96.71% decrease in YFP emission (figure-45). However, such strong laser power was uncomfortable for the pupae and consequently measurements were hindered by pupal movement. Given that the area selected for photobleaching only contained 5 cells, this proved to be a big hinderance to undertaking acceptor photobleaching experiments.

The initial result using this protocol were very promising. Following photobleaching of the acceptor (YFP), YFP emission decreased by 96.71%, exceeding the target of 90% reduction in YFP emission. This corresponded to an increase in CFP emission by 69.00% and a decrease in YFP sensitised emission by 54.52%. Measurements emission at the five subsequent time points following photobleaching indicated no recovery of fluorescence. In fact, emission in all three measurements continued to decrease, albeit only marginally. This

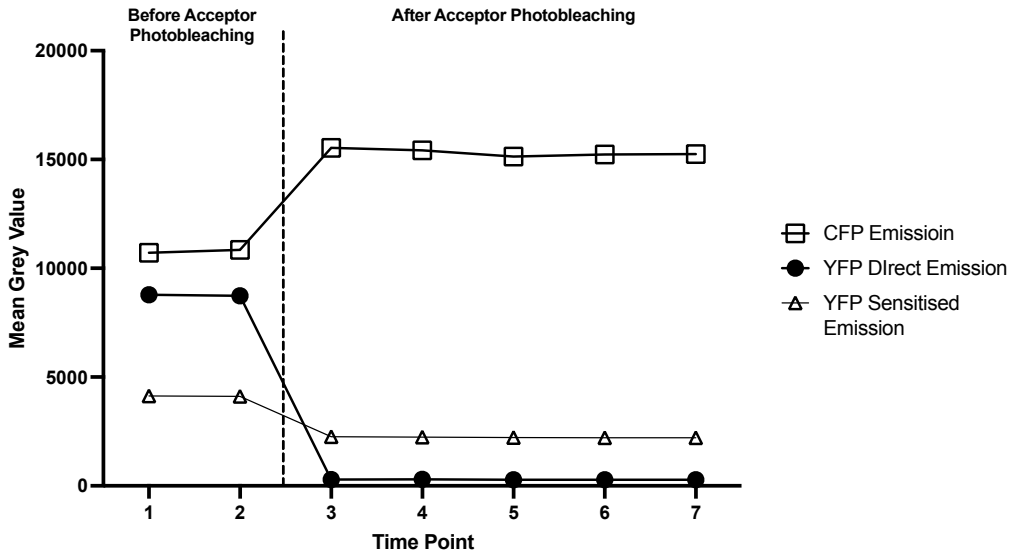

Figure 45- An increase in CFP emission and corresponding decrease in YFP sensitised emission was detected upon over 90% bleaching of the acceptor, YFP. *Direct YFP emission, CFP emission and YFP sensitised emission were recorded before and after acceptor (YFP) photobleaching within a five-cell radius at all planes, using confocal microscopy. A 69.00% increase in CFP emission and a decrease in YFP sensitised emission by 54.52% was recorded. n=1, 1 animal*

provides preliminary indications that our protocol could be successfully utilised to undertaken acceptor photobleaching control experiments.

4.3 PKA Sensor Expression

Having detected cAMP gradients within the sheet-like actin-based membrane protrusions within the intermediate region of *Drosophila* epithelial cells, we wondered whether these increased cAMP concentrations were correlated with localisation of its one of its secondary effectors PKA. A putative mechanism for cAMP signalling through PKA in actin cytoskeleton regulation is through the downregulation of RhoA signalling. Therefore, it would be interesting to determine the expression pattern of PKA at different localities, such as the apical or basolateral domain, and its distribution throughout the range of actin membrane-based protrusions found within the cell. Thus, we took advantage of a FLINC-based PKA sensor to measure the distribution of PKA within these structures. Our aim was to establish and optimise a protocol for the use of this sensor, however due to time constraints, only direct excitation work to confirm sensor expression was undertaken. Upon direct RFP excitation, we determined that Pnr-FLINC^{+} cells were well-expressed throughout the notum and the expression pattern conformed to that observed in GFP-Moe-Pnr^{+} (figure-46). Although this appeared promising, RFP excitation of Neu-FLINC^{+} cells within the notum revealed that no Neu-FLINC^{+} cells could be detected.

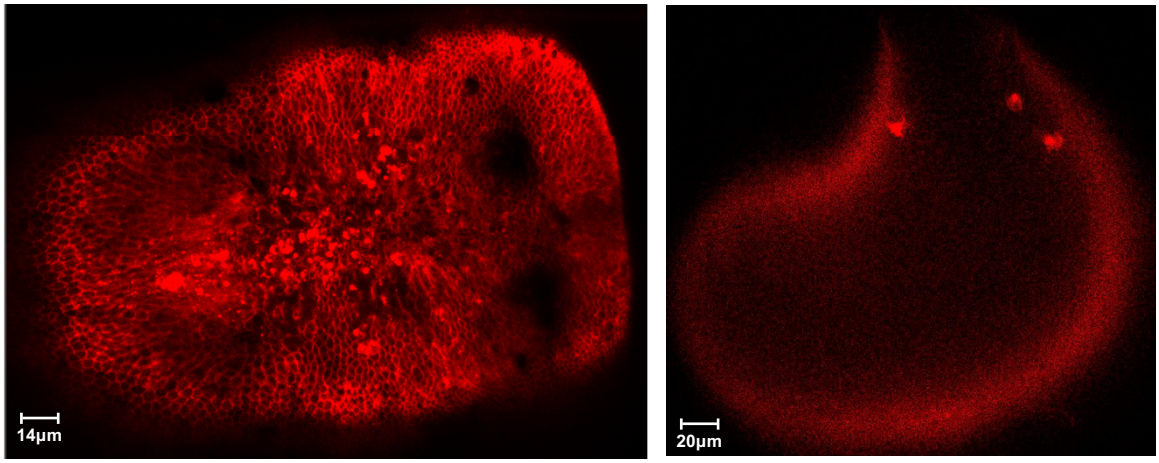

Figure 46- The FLINC PKA sensor is well expressed when driven by the tissue specific promoter Pannier, but boasts poor expression where driven by tissue specific promoter Neuralized. *Note that no Neu-FLINC^{+} cells were observed. Direct RFP excitation was undertaken using a 561 laser. A tile-scan was undertaken (left) where sensor expression was driven by Pannier, and a Z-stack was undertaken where sensor expression was driven by Neuralized to determine expression pattern. Brightness and contrast were adjusted using ImageJ to aid visualisation.*

Chapter 5: Discussion

5.1 cAMP Was More Highly Concentrated Within Intermediate-Lateral Protrusion Tips Compared to the Base, Middle or Cell Cytosol in Well-Spaced Epithelial Cells

This project aimed to establish and optimise a protocol for the measurement of intracellular cAMP gradients, using a genetically encoded FRET-based cAMP biosensor, within the actin membrane-based protrusions of *Drosophila melanogaster*. Early work quantifying cAMP gradients and concentrations within the cell relied on the extraction of purification of cAMP from cellular fractions. Experiments employing this methodology were revealing regarding cAMP compartmentalisation within the cell; many studies involved relied on measuring cAMP concentrations under various states of knockdown of key components of the signalling pathway, such as PKA, PDEs and AKAPs. Although early studies were significant and provided early weight to the notion of cAMP compartmentalisation, a great limitation of this methodology was the fact that cAMP concentrations were neither physiologically relevant nor measured within the cellular environment, limiting the reliability of measurements. The advent of FRET-based cAMP biosensors was revolutionary to the field; for the first time, scientists could undertake cAMP measurements within the cell which gave a much greater and more relevant understanding of the complexities of cAMP compartmentalisation. Experiments employed both simple (HEK293 cells) and more complex (cardiac fibroblasts) cell lines making findings more robust. Moreover, cAMP could be stimulated (using agonists) and other components of the signalling pathway could be inhibited using antagonists or knockdown. This gave

a much better idea of the significance of different components of the signalling pathway and their role in cAMP compartmentalisation. More recent work employs the use of updated tools, such as fluorescent cAMP analogues and molecular rulers to measure the extent of cAMP nanodomains and compartmentalisation of GPCR signalling. While this work has been undertaken in cell lines, logically the next step in the advance of information regarding the spatiotemporal regulation of signalling pathways is undertaking measurements in live animals. To this end, we took advantage of a genetically encoded cAMP-based FRET biosensor which we expressed within the epithelial cells of model organism *Drosophila melanogaster* to study cAMP gradients within actin-based protrusions. cAMP is a second messenger which may mediate the spatial and temporal specificity of signals derived from small GTPases Rac, RhoA and Cdc42 which play a key role in modulating actin cytoskeleton remodelling. What remains unclear is the precise locality of these signalling events within actin membrane-based protrusions and spatial correlation with subcellular cAMP gradients.

The Epac-based version of the sensor was selected due to its increased FRET efficiency and preferable signal to noise ratio (SNR) in comparison to PKA-based cAMP sensors. Furthermore, Epac-based sensors have been shown to be superior in their activation kinetics and dynamic range when compared to sensors based on other molecules. The final protocol engaged confocal microscopy techniques to obtain 3D measurements of cAMP gradients using sensitised emission FRET. We successfully employed our protocol in the measurement of cAMP gradients within intermediate-lateral protrusions of well-spaced neu-epac1camps^{+} epithelial cells via the GAL4-UAS system, in addition to pnr-epac1camps^{+} epithelial cell clones generated using the MARCM system. We detected statistically significant elevated cAMP concentrations within protrusion tips in comparison to the cell cytosol and protrusion base and middle within neu-epac1camps^{+} cells. This suggests that cAMP is highly concentrated in the tip of intermediate-

lateral actin protrusions in neu-epac1camps^{+} cells. To our knowledge, this is the first report of localised cAMP gradients within actin-based protrusions in *Drosophila*.

The finding that cAMP is elevated within the tip of neu-epac1camps^{+} cells is interesting. Previous work in the *Dictyostelium discoideum* has demonstrated the importance of cAMP gradients in chemotaxis(Garcia et al., 2013). Experimental evidence showed that *Dictyostelium discoideum* could sense cAMP secreted by other *Dictyostelium discoideum* cells which, in turn, provoked that cell to begin producing cAMP too(van Haastert et al., 2007). Increases in cAMP within the tips of filopodia or lamellipodia protrusions was also correlated with an increase in actin polymerisation. However, this notion was contradicted by further experiments which postulated the idea that oscillatory cAMP signalling is not required for collective cell migration but instead chemotaxis is regulated by PLC via intracellular Ca^{2+} concentrations, not cAMP(Hashimura et al., 2019). Furthermore, given that PKA inhibition has been correlated with decreased expression of Notch target gene products and decreased junction cadherin expression in vascular endothelial cells, there could be convergence between cAMP and Delta-Notch signalling pathways in some cell types(Boardman et al., 2019). Therefore, it is intriguing that relative cAMP concentrations were found to be elevated with protrusion tips considering that previous work in *Drosophila* has established basal filopodia engage in cell-cell communication via Delta/Notch signalling(Cohen et al., 2010). However, as interesting as this idea is, the fact remains that relative increased cAMP concentration was detected within the tips of intermediate-lateral protrusions, which thus far have not been implicated in cell-cell communication via Delta/Notch signalling. Furthermore, although convergence of Delta/Notch and cAMP signalling has been implicated in vascular endothelial cells, often the end result of signalling pathways is ligand and cell-type specific. Therefore, while this evidence demonstrates the possibility of signalling

convergence between the two pathways, it does not demonstrate convergence in the context of actin protrusions within the epithelial cells of *Drosophila*. Nevertheless, the quantification of cAMP gradients within basal filopodia could be an interesting experimental avenue.

Furthermore, our results are in harmony with evidence implicating the role of the secondary effectors in the cAMP signalling pathway PKA and Epac1 in actin cytoskeletal organisation. Experimental evidence supports the idea that Epac1 is required for actin cytoskeletal organisation; Epac1 inhibition in bladder cancer cells was correlated with a decrease in actin-based migration(Ichikawa et al., 2018). Furthermore, PKA has been shown to inhibit RhoA signalling by creating a stable RhoA-GDP-RhoGDIa complex, promoting re-localisation to the cytosol(Oishi et al., 2012). This could decrease MLCK-based filament contraction. Furthermore, treatment of mESCs with a cAMP analogue was found to increase Arp3, TOCA, PAK and N-WASP protein concentrations, all of which are important for actin nucleation and protrusion formation(Tonucci et al., 2019). Additionally, CIP4 phosphorylation by PKA has been linked with increased cell migration; experiments revealed that CIP4 resistant to PKA phosphorylation decreased migration. Adding to this, PKA activity maps have pinpointed increased PKA localisation at the plasma membrane of basal protrusions and within filopodia of migrating α4CHO cells(Mo et al., 2017). This seemingly implicates cAMP action in protrusion formation, morphology and regulation of protrusion dynamics. This could justify an increased cAMP concentration within protrusion tips.

However, as migration involves basal filopodia it is unclear whether this is also true for intermediate protrusions, which are not present in front-rear polarised migrating cells and possess an unknown role within the cell. Another important consideration is the point that the images we obtained were static. Actin based protrusions are continually in a state of retraction and extension, therefore it is unclear whether protrusions

were imaged in a state of retraction or extension which could conceivably involve different concentrations of cAMP to induce different effects. Therefore, acquiring time-lapses to visualise how cAMP changes during these retraction and extension cycles would provide additional spatiotemporal information regarding cAMP signalling.

Inhibition of the cAMP secondary effector Epac1 in different cell lines was correlated with activation of RhoA and the MLCK pathway, inducing actin filament contraction seemingly contradicting the role of PKA in RhoA sequestration to induce cell rounding(Kumar et al., 2017). This could be because, RhoA signalling is also linked with actin nucleation through Dia activation of profilin, which promotes actin nucleation. Therefore, RhoA sequestration could ostensibly also decrease actin nucleation and protrusion formation. Adding to this, RhoA-ROCK signalling has been implicated during axon-injury to induce the MLCK pathway to increasing actin contraction(Sakai et al., 2021). Conceivably, the action of cAMP effectors to decrease protrusion formation would appear to contradict our results. However, it is important to consider the fact that this contradictory evidence could be accounted for by the fact that it is appropriate spatiotemporal governance which produces the correct physiological response based on the stimuli, i.e. different stimuli could prompt different responses through the same signalling components of the cAMP pathway. Furthermore, it is well established that greater activation of RhoA at the lagging edge and increased Cdc42 and Rac activation at the leading-edge prompts actin nucleation at the leading edge and contraction at the lagging edge(Lawson and Ridley, 2018). This highlights the importance of the appropriate spatiotemporal activation of these key components. Credibly, this could be enacted by GPCR RAINs in which nanodomains of cAMP signalling exist to ensure that each stimulus prompts the correct response amid a multitude of signals from the wide variety of GPCRs in the cell(Anton et al., 2022). This idea is supported by the fact relative elevated cAMP concentrations were localised to the

protrusion tip, hinting at possible compartmentalisation of signalling. Although, in order to draw this conclusion, further study of the distribution of components known to be responsible for cAMP signal compartmentalisation, such as AKAPs and PDEs, is required. Additionally, as cAMP gradients within epithelial cells were recorded at basal, unstimulated levels during this project, it is possible that this approach could omit key aspects of cAMP signalling which is a significant limitation. It is possible to stimulate cAMP signalling using forskolin (an AC activator which stimulates production of AC) within *Drosophila melanogaster* however, due to time restraints, this was not possible during the project(Maiellaro et al., 2016). Therefore, we suggest future work should employ this protocol to measure stimulated cAMP gradients within the *Drosophila melanogaster* model system.

5.2 No Significant Difference in cAMP Concentration Was Detected Within Intermediate-Lateral Actin Protrusions or Cell Cytosol in Epithelial Cell Clones

Strangely, the same cAMP elevations within intermediate-lateral protrusions tips were not apparent in pnr-epac1camps^{+} clones. There was no statistically significant difference between the cell cytosol, intermediate-lateral protrusion base, middle or tip. This would appear to suggest that cAMP is not implicated in actin protrusion formation or any signalling occurring through the protrusions. However, this result could be due to practical challenges with quantitating FRET ratios within pnr-epac1camps^{+} clones; little cytosol is available for measurement and often it is ambiguous as to which cell the cytosol belongs to, due to the nature of the epithelial sheet, which could limit measurements undertaken within these cells. Furthermore, another reason underlying absence of differences in relative cAMP concentration could be a greater number neu-camps-epac1^{+} animals utilised in experiments (18 neu-camps-epac1^{+} animals, 30 cells and 5 pnr-camps-epac1^{+} animals, 25 clones), which could give a more representative picture of relative cAMP ratios. Additionally, labelling well-spaced neu-camps-epac1^{+} could be more sensitive due to decreased noise from adjacent cells. However, we compensated for this issue within our protocol by limiting the pinhole to 1AU to limit the amount of noise detected within pnr-camps-epac1^{+} clones.

5.3 A Confocal Microscopy Protocol for the Measurement and Analysis of Sensitised Emission FRET Was Established and Optimised

Although previous studies made use of widefield epifluorescence microscopy techniques to obtain measurements, upon use of this protocol to assess CFP emission and YFP sensitised emission it was discovered that Pnr-epac1camps^{+} and neu-epac1camps^{+} cells were not visible. The use of widefield techniques is advantageous in cases where FRET biosensor expression is low, such is the case where expression was driven by the promoter Neuralized, as the absence of pinhole filtering increases the amount of fluorescence emission detected(Willoughby and Cooper, 2008). However, the presence of high levels of autofluorescence originating from the cuticle in *Drosophila* limits the use of widefield epifluorescence microscopy in sensitised emission FRET experiments involving epithelial cells within the notum. It is likely that the lack of visible cells expressing the sensor observed using widefield techniques is due to a highly autofluorerscent cuticle 1µm above them, which could conceivably obscure any fluorescence originating from sensor excitation(McGurk et al., 2007). Although, this could be mitigated by the use of novel cAMP sensors or deployment of a red-shifted biosensor to mitigate background. Therefore, it made sense to utilise confocal microscopy for experiments as it also boasted preferable spatial resolution, allowing precise detection of cAMP gradients within the actin-membrane based protrusions.

5.4 Optimisation of Incubation Regimes Enhanced Sensor Expression in neu-epac1-camps^{+} cells

Initially, no neu-epac1-camps^{+} cells could be observed upon direct YFP excitation using confocal microscopy. As sensor expression had been confirmed prior to experiments using a fluorescent stereomicroscope, we could reliably conclude that Neuralized was successful in driving sensor expression but to what extent was unclear. Poor expression could be induced by a number of reasons; different *Drosophila* crosses could reach developmental milestones at different rates, incubators might not be holding the temperature displayed and protein folding rates vary at different temperatures(Guo et al., 2012). However, it should be noted that while tile-scans are useful for observing the general expression pattern of cells within the notum, they are limited by the fact that cell apexes could be located at different depths. This could lead to underestimation of the number of cells expressing the sensor. Despite this, optimisation of incubation regimes to maximise incubation at 25°C, in addition to imaging cells at 15.5 hours boosted sensor expression within neu-epac1-camps^{+} cells. However, it is a likely that a malfunctioning incubator contributed towards poor pupae expression as it was found to contain large quantities of ice, indicating that it had been holding sub-zero temperatures despite displaying the correct temperature on the display. Therefore, not only would this compromised protein folding, but pupae would have been imaged too young, before cells in the notum had developed. This is seemingly quite a plausible explanation especially as it was only used to incubate neu-epac1camps^{+} pupae. Pannier was found to drive sensor expression to much higher levels; this could be because pnr-epac1-camps^{+} pupae were incubated at 29°C and for a longer period than neu-epac1-camps^{+} cells, maximising the amount of protein folding and increasing sensor expression. An avenue for further optimisation could be incubation of neu-epac1-camps^{+} at 29°C for a period of time to determine whether

this could increase sensor expression. However, this could be made difficult by the fact that in order to age pupae correctly, some incubation at 18°C would also be required, thus limiting sensor folding.

5.5 Sensitised Emission FRET Could Not Be Detected Within the Basal Protrusions of Well-Spaced Epithelial Cells

Direct YFP excitation tile-scans of neu-epac1-camps^{+} cells revealed basal protrusions could not be observed using confocal microscopy. The idea that the lack of detectable signal within basal protrusions of neu-camps-epac1^{+} cells is due to a low of cAMP is not a plausible one. Even if cAMP was lacking in this locality, surely fluorescence would still be detectable indicating that this is not the case. Furthermore, other groups have pinpointed PKA localisation within the basal plasma membrane adjacent to filopodia implicating the presence of cAMP signalling within or near basal protrusions(Mo et al., 2017). Although, it is important to note that these observations were made within migrating cells which could possess a different spatial distribution of cAMP than wild-type non-migrating cells. As basal protrusions were visualised in pnr-epac1camps^{+} clones during sensitised emission FRET, we conclude that in order to undertake sensitised emission FRET measurements in neu-epac1camps^{+} cells a higher sensor expression is required.

Chapter 6: Conclusions and Future Perspectives

6.1 Conclusions

We have successfully created and optimised a protocol for undertaking sensitised emission FRET via confocal Microscopy. Not only did this confer high spatial resolution, enabling detection of localised relative basal cAMP concentrations within actin protrusions, but measurements were also undertaken within a three-dimensional, polarised epithelial sheet of a live animal making measurements highly physiologically relevant. We detected higher relative basal concentrations of cAMP within protrusion tips in comparison protrusion base, middle or cell cytosol in neu-camps-epac1^{+} cells but not pnr-camps-epac1^{+} clones, which we conclude could be due to limitations of working with pnr-camps-epac1^{+} clones, in addition to a smaller sample size. Much work so far has lacked accurate spatial resolution within actin membrane-based protrusions and was undertaken in cell lines which do not accurately represent the real cellular environment, further emphasising the promise of our preliminary investigation. Our preliminary results indicated a basis for subcellular compartmentalisation of within intermediate-lateral actin protrusions, warranting further investigation to determine whether notorious components responsible for enforcing cAMP compartmentalisation, such as PDEs and AKAPs, are present.

6.2 Future Perspectives

Experiments inhibiting key signalling components involved in cAMP compartmentalisation, such as AKAPs, would be an interesting next step to confirm the presence of cAMP nanodomain, in addition to the use of novel cAMP tools such as nanorulers within actin protrusions. Chemical inhibition of AKAPs could also a useful control to determine whether cAMP dynamics are a due to limited sensor detection or due to 'true' localised cAMP dynamics. Additionally, cAMP stimulation experiments could be performed to clearly visualise the effect of cAMP on protrusion dynamics. Importantly, time-lapse experiments should be undertaken to measure cAMP concentration within the dynamic actin protrusions. This would better capture the alterations in cAMP concentrations within intermediate lateral protrusions. A further experimental avenue involves the optimisation and application of a protocol for the use of the PKA-FLINC sensor previously mentioned within this thesis, to determine whether cAMP gradients are correlated with increased PKA activity, especially as recent experimental evidence suggests a role for PKA as an effector to transduce effects on the actin cytoskeleton. Flies containing YFP only and CFP proteins should also be measured to determine the effect of spectral bleedthrough of CFP into the YFP channel, in addition to further acceptor photobleaching experiments. Furthermore, use of PDE mutants could be useful in detecting abrogated cAMP gradients, in addition to pharmacological inhibition of cAMP production. Finally, experiments employing a catalytically inert sensor should be undertaken to confirm that results observed are due to alterations in cAMP concentration.

Bibliography

References

ALGAR, W. R., HILDEBRANDT, N., VOGEL, S. S. & MEDINTZ, I. L. 2019. FRET as a biomolecular research tool — understanding its potential while avoiding pitfalls. *Nature Methods,* 16**,** 815-829.

ANTON, S. E., KAYSER, C., MAIELLARO, I., NEMEC, K., MÖLLER, J., KOSCHINSKI, A., ZACCOLO, M., ANNIBALE, P., FALCKE, M., LOHSE, M. J. & BOCK, A. 2022. Receptor-associated independent cAMP nanodomains mediate spatiotemporal specificity of GPCR signaling. *Cell,* 185**,** 1130-1142.e11.

AOYAMA, H., IKEDA, Y., MIYAZAKI, Y., YOSHIMURA, K., NISHINO, S., YAMAMOTO, T., YANO, M., INUI, M., AOKI, H. & MATSUZAKI, M. 2011. Isoform-specific roles of protein phosphatase 1 catalytic subunits in sarcoplasmic reticulum-mediated Ca(2+) cycling. *Cardiovasc Res,* 89**,** 79-88.

BAUMAN, A. L., SOUGHAYER, J., NGUYEN, B. T., WILLOUGHBY, D., CARNEGIE, G. K., WONG, W., HOSHI, N., LANGEBERG, L. K., COOPER, D. M., DESSAUER, C. W. & SCOTT, J. D. 2006. Dynamic regulation of cAMP synthesis through anchored PKA-adenylyl cyclase V/VI complexes. *Mol Cell,* 23**,** 925-31.

BENDER, A. T. & BEAVO, J. A. 2006. Cyclic Nucleotide Phosphodiesterases: Molecular Regulation to Clinical Use. *Pharmacological Reviews,* 58**,** 488.

BERTHET, J., RALL, T. W. & SUTHERLAND, E. W. 1957. The relationship of epinephrine and glucagon to liver phosphorylase. IV. Effect of epinephrine and glucagon on the reactivation of phosphorylase in liver homogenates. *J Biol Chem,* 224**,** 463-75.

BERTHOUZE-DUQUESNES, M., LUCAS, A., SAULIÈRE, A., SIN, Y. Y., LAURENT, A. C., GALÉS, C., BAILLIE, G. & LEZOUALC'H, F. 2013. Specific interactions between Epac1, β-arrestin2 and PDE4D5 regulate β-adrenergic receptor subtype differential effects on cardiac hypertrophic signaling. *Cell Signal,* 25**,** 970-80.

BHAT, P., HONSON, D. & GUTTMAN, M. 2021. Nuclear compartmentalization as a mechanism of quantitative control of gene expression. *Nature Reviews Molecular Cell Biology,* 22**,** 653-670.

BIRO, M., MUNOZ, M. A. & WENINGER, W. 2014. Targeting Rho-GTPases in immune cell migration and inflammation. *Br J Pharmacol,* 171**,** 5491-506.

BOARDMAN, R., PANG, V., MALHI, N., LYNCH, A. P., LEACH, L., BENEST, A. V., BATES, D. O. & MACHADO, M. J. C. 2019. Activation of Notch signaling by soluble Dll4 decreases vascular permeability via a cAMP/PKA-dependent pathway. *American*

Journal of Physiology-Heart and Circulatory Physiology, 316**,** H1065-H1075.
BOCK, A., ANNIBALE, P., KONRAD, C., HANNAWACKER, A., ANTON, S. E., MAIELLARO, I., ZABEL, U., SIVARAMAKRISHNAN, S., FALCKE, M. & LOHSE, M. J. 2020. Optical Mapping of cAMP Signaling at the Nanometer Scale. *Cell,* 182**,** 1519-1530.e17.
BOEYNAEMS, S., ALBERTI, S., FAWZI, N. L., MITTAG, T., POLYMENIDOU, M., ROUSSEAU, F., SCHYMKOWITZ, J., SHORTER, J., WOLOZIN, B., VAN DEN BOSCH, L., TOMPA, P. & FUXREITER, M. 2018. Protein Phase Separation: A New Phase in Cell Biology. *Trends Cell Biol,* 28**,** 420-435.
BÖRNER, S., SCHWEDE, F., SCHLIPP, A., BERISHA, F., CALEBIRO, D., LOHSE, M. J. & NIKOLAEV, V. O. 2011. FRET measurements of intracellular cAMP concentrations and cAMP analog permeability in intact cells. *Nat Protoc,* 6**,** 427-38.
BOS, J. L. 2006. Epac proteins: multi-purpose cAMP targets. *Trends Biochem Sci,* 31**,** 680-6.
BRAND, A. H. & PERRIMON, N. 1993. Targeted gene expression as a means of altering cell fates and generating dominant phenotypes. *Development,* 118**,** 401-15.
BURACK, W. R. & SHAW, A. S. 2000. Signal transduction: hanging on a scaffold. *Curr Opin Cell Biol,* 12**,** 211-6.
BURDYGA, A., SURDO, N. C., MONTERISI, S., DI BENEDETTO, G., GRISAN, F., PENNA, E., PELLEGRINI, L., ZACCOLO, M., BORTOLOZZI, M., SWIETACH, P., POZZAN, T. & LEFKIMMIATIS, K. 2018. Phosphatases control PKA-dependent functional microdomains at the outer mitochondrial membrane. *Proc Natl Acad Sci U S A,* 115**,** E6497-e6506.
CADD, G. & MCKNIGHT, G. S. 1989. Distinct patterns of cAMP-dependent protein kinase gene expression in mouse brain. *Neuron,* 3**,** 71-9.
CALEBIRO, D. & GODBOLE, A. 2018. Internalization of G-protein-coupled receptors: Implication in receptor function, physiology and diseases. *Best Pract Res Clin Endocrinol Metab,* 32**,** 83-91.
CALEBIRO, D., NIKOLAEV, V. O., GAGLIANI, M. C., DE FILIPPIS, T., DEES, C., TACCHETTI, C., PERSANI, L. & LOHSE, M. J. 2009. Persistent cAMP-Signals Triggered by Internalized G-Protein–Coupled Receptors. *PLOS Biology,* 7**,** e1000172.
CANALES COUTIÑO, B., CORNHILL, Z. E., COUTO, A., MACK, N. A., RUSU, A. D., NAGARAJAN, U., FAN, Y. N., HADJICHARALAMBOUS, M. R., CASTELLANOS URIBE, M., BURROWS, A., LOURDUSAMY, A., RAHMAN, R., MAY, S. T. & GEORGIOU, M. 2020. A Genetic Analysis of Tumor Progression in Drosophila Identifies the Cohesin Complex as a Suppressor of Individual and Collective Cell Invasion. *iScience,* 23**,** 101237.
CANALES COUTIÑO, B., SZAMEK, E., MARKUS, Z. & GEORGIOU, M. 2021. Generation and live imaging of tumors with specific genotypes in the living fly pupa. *STAR Protocols,* 2**,** 100672.

CAZORLA, O., LUCAS, A., POIRIER, F., LACAMPAGNE, A. & LEZOUALC'H, F. 2009. The cAMP binding protein Epac regulates cardiac myofilament function. *Proceedings of the National Academy of Sciences,* 106**,** 14144-14149.
CLAYTON, N. S. & RIDLEY, A. J. 2020. Targeting Rho GTPase Signaling Networks in Cancer. *Frontiers in Cell and Developmental Biology,* 8.
COGHLAN, V. M., PERRINO, B. A., HOWARD, M., LANGEBERG, L. K., HICKS, J. B., GALLATIN, W. M. & SCOTT, J. D. 1995. Association of protein kinase A and protein phosphatase 2B with a common anchoring protein. *Science,* 267**,** 108-11.
COHEN, M., GEORGIOU, M., STEVENSON, N. L., MIODOWNIK, M. & BAUM, B. 2010. Dynamic Filopodia Transmit Intermittent Delta-Notch Signaling to Drive Pattern Refinement during Lateral Inhibition. *Developmental Cell,* 19**,** 78-89.
COUTO, A., MACK, N. A., FAVIA, L. & GEORGIOU, M. 2017. An apicobasal gradient of Rac activity determines protrusion form and position. *Nature Communications,* 8**,** 15385.
DAVIDSON, A. J. & WOOD, W. 2016. Unravelling the Actin Cytoskeleton: A New Competitive Edge? *Trends in Cell Biology,* 26**,** 569-576.
DESSAUER, C. W. 2009. Adenylyl cyclase--A-kinase anchoring protein complexes: the next dimension in cAMP signaling. *Mol Pharmacol,* 76**,** 935-41.
DEVREOTES, P. & HORWITZ, A. R. 2015. Signaling networks that regulate cell migration. *Cold Spring Harb Perspect Biol,* 7**,** a005959.
DODGE, K. L., KHOUANGSATHIENE, S., KAPILOFF, M. S., MOUTON, R., HILL, E. V., HOUSLAY, M. D., LANGEBERG, L. K. & SCOTT, J. D. 2001. mAKAP assembles a protein kinase A/PDE4 phosphodiesterase cAMP signaling module. *Embo j,* 20**,** 1921-30.
DODGE-KAFKA, K. L., BAUMAN, A., MAYER, N., HENSON, E., HEREDIA, L., AHN, J., MCAVOY, T., NAIRN, A. C. & KAPILOFF, M. S. 2010. cAMP-stimulated protein phosphatase 2A activity associated with muscle A kinase-anchoring protein (mAKAP) signaling complexes inhibits the phosphorylation and activity of the cAMP-specific phosphodiesterase PDE4D3. *J Biol Chem,* 285**,** 11078-86.
DOSTMANN, W. R., TAYLOR, S. S., GENIESER, H. G., JASTORFF, B., DØSKELAND, S. O. & OGREID, D. 1990. Probing the cyclic nucleotide binding sites of cAMP-dependent protein kinases I and II with analogs of adenosine 3',5'-cyclic phosphorothioates. *J Biol Chem,* 265**,** 10484-91.
DROR, R. O., ARLOW, D. H., MARAGAKIS, P., MILDORF, T. J., PAN, A. C., XU, H., BORHANI, D. W. & SHAW, D. E. 2011. Activation mechanism of the β2-adrenergic receptor. *Proc Natl Acad Sci U S A,* 108**,** 18684-9.
EFENDIEV, R., BAVENCOFFE, A., HU, H., ZHU, M. X. & DESSAUER, C. W. 2013. Scaffolding by A-kinase anchoring protein enhances

functional coupling between adenylyl cyclase and TRPV1 channel. *J Biol Chem,* 288**,** 3929-37.
ESPOSITO, M., FANG, C., COOK, K. C., PARK, N., WEI, Y., SPADAZZI, C., BRACHA, D., GUNARATNA, R. T., LAEVSKY, G., DECOSTE, C. J., SLABODKIN, H., BRANGWYNNE, C. P., CRISTEA, I. M. & KANG, Y. 2021. TGF-β-induced DACT1 biomolecular condensates repress Wnt signalling to promote bone metastasis. *Nature Cell Biology,* 23**,** 257-267.
ETIENNE-MANNEVILLE, S. & HALL, A. 2002. Rho GTPases in cell biology. *Nature,* 420**,** 629-35.
FORSTER, T. 1946. Energiewanderung und Fluoreszenz. *Naturwissenschaften,* 33**,** 166-175.
FURMAN, D. P. & BUKHARINA, T. A. 2008. How Drosophila melanogaster Forms its Mechanoreceptors. *Curr Genomics,* 9**,** 312-23.
GARBER, A. J. 1980. The Impact of Streptozotocin-induced Diabetes Mellitus on Cyclic Nucleotide Regulation of Skeletal Muscle Amino Acid Metabolism in the Rat. *The Journal of Clinical Investigation,* 65**,** 478-487.
GARCIA, R., NGUYEN, L. & BRAZILL, D. 2013. Dictyostelium discoideum SecG interprets cAMP-mediated chemotactic signals to influence actin organization. *Cytoskeleton (Hoboken),* 70**,** 269-80.
GEORGIOU, M. & BAUM, B. 2010. Polarity proteins and Rho GTPases cooperate to spatially organise epithelial actin-based protrusions. *J Cell Sci,* 123**,** 1089-98.
GOLIC, K. G. & LINDQUIST, S. 1989. The FLP recombinase of yeast catalyzes site-specific recombination in the Drosophila genome. *Cell,* 59**,** 499-509.
GUO, M., XU, Y. & GRUEBELE, M. 2012. Temperature dependence of protein folding kinetics in living cells. *Proceedings of the National Academy of Sciences,* 109**,** 17863-17867.
HALL, A. 1998. Rho GTPases and the actin cytoskeleton. *Science,* 279**,** 509-14.
HANLON, C. D. & ANDREW, D. J. 2015. Outside-in signaling--a brief review of GPCR signaling with a focus on the Drosophila GPCR family. *J Cell Sci,* 128**,** 3533-42.
HASHIMURA, H., MORIMOTO, Y. V., YASUI, M. & UEDA, M. 2019. Collective cell migration of Dictyostelium without cAMP oscillations at multicellular stages. *Communications Biology,* 2**,** 34.
HEBERT, B., COSTANTINO, S. & WISEMAN, P. W. 2005. Spatiotemporal image correlation spectroscopy (STICS) theory, verification, and application to protein velocity mapping in living CHO cells. *Biophys J,* 88**,** 3601-14.
HERZIG, S. & NEUMANN, J. 2000. Effects of serine/threonine protein phosphatases on ion channels in excitable membranes. *Physiol Rev,* 80**,** 173-210.
HILL, S. J. 2006. G-protein-coupled receptors: past, present and future. *British Journal of Pharmacology,* 147**,** S27-S37.

HOHL, C. M. & LI, Q. A. 1991. Compartmentation of cAMP in adult canine ventricular myocytes. Relation to single-cell free Ca2+ transients. *Circ Res,* 69**,** 1369-79.
HOUSLAY, M. D. & MILLIGAN, G. 1997. Tailoring cAMP-signalling responses through isoform multiplicity. *Trends Biochem Sci,* 22**,** 217-24.
HUANG, F., DAMBLY-CHAUDIÈRE, C. & GHYSEN, A. 1991. The emergence of sense organs in the wing disc of Drosophila. *Development,* 111**,** 1087-95.
ICHIKAWA, H., ITSUMI, M., KAJIOKA, S., MAKI, T., LEE, K., TOMITA, M. & YAMAOKA, S. 2018. Overexpression of exchange protein directly activated by cAMP-1 (EPAC1) attenuates bladder cancer cell migration. *Biochemical and Biophysical Research Communications,* 495**,** 64-70.
JANSEN, S., GOSENS, R., WIELAND, T. & SCHMIDT, M. 2018. Paving the Rho in cancer metastasis: Rho GTPases and beyond. *Pharmacology & Therapeutics,* 183**,** 1-21.
KADZIK, R. S., HOMA, K. E. & KOVAR, D. R. 2020. F-Actin Cytoskeleton Network Self-Organization Through Competition and Cooperation. *Annu Rev Cell Dev Biol,* 36**,** 35-60.
KAMPS, A. R., PRUITT, M. M., HERRIGES, J. C. & COFFMAN, C. R. 2010. An evolutionarily conserved arginine is essential for Tre1 G protein-coupled receptor function during germ cell migration in Drosophila melanogaster. *PLoS One,* 5**,** e11839.
KOMATSU, N., AOKI, K., YAMADA, M., YUKINAGA, H., FUJITA, Y., KAMIOKA, Y. & MATSUDA, M. 2011. Development of an optimized backbone of FRET biosensors for kinases and GTPases. *Molecular Biology of the Cell,* 22**,** 4647-4656.
KUMAR, N., GUPTA, S., DABRAL, S., SINGH, S. & SEHRAWAT, S. 2017. Role of exchange protein directly activated by cAMP (EPAC1) in breast cancer cell migration and apoptosis. *Mol Cell Biochem,* 430**,** 115-125.
KUMAR, N., PRASAD, P., JASH, E., SAINI, M., HUSAIN, A., GOLDMAN, A. & SEHRAWAT, S. 2018. Insights into exchange factor directly activated by cAMP (EPAC) as potential target for cancer treatment. *Molecular and Cellular Biochemistry,* 447**,** 77-92.
LAI, E. C., DEBLANDRE, G. A., KINTNER, C. & RUBIN, G. M. 2001. Drosophila neuralized is a ubiquitin ligase that promotes the internalization and degradation of delta. *Dev Cell,* 1**,** 783-94.
LANGENHAN, T., BARR, M. M., BRUCHAS, M. R., EWER, J., GRIFFITH, L. C., MAIELLARO, I., TAGHERT, P. H., WHITE, B. H. & MONK, K. R. 2015. Model Organisms in G Protein-Coupled Receptor Research. *Mol Pharmacol,* 88**,** 596-603.
LATORRACA, N. R., VENKATAKRISHNAN, A. J. & DROR, R. O. 2017. GPCR Dynamics: Structures in Motion. *Chemical Reviews,* 117**,** 139-155.
LAWSON, C. D. & RIDLEY, A. J. 2018. Rho GTPase signaling complexes in cell migration and invasion. *J Cell Biol,* 217**,** 447-457.

LEE, J. L. & STREULI, C. H. 2014. Integrins and epithelial cell polarity. *J Cell Sci,* 127**,** 3217-25.
LEE, S. H. & DOMINGUEZ, R. 2010. Regulation of actin cytoskeleton dynamics in cells. *Mol Cells,* 29**,** 311-25.
LEE, T. & LUO, L. 2001. Mosaic analysis with a repressible cell marker (MARCM) for Drosophila neural development. *Trends Neurosci,* 24**,** 251-4.
LEROY, J., ABI-GERGES, A., NIKOLAEV, V. O., RICHTER, W., LECHÊNE, P., MAZET, J. L., CONTI, M., FISCHMEISTER, R. & VANDECASTEELE, G. 2008. Spatiotemporal dynamics of beta-adrenergic cAMP signals and L-type Ca2+ channel regulation in adult rat ventricular myocytes: role of phosphodiesterases. *Circ Res,* 102**,** 1091-100.
LI, Y., KAO, G. D., GARCIA, B. A., SHABANOWITZ, J., HUNT, D. F., QIN, J., PHELAN, C. & LAZAR, M. A. 2006. A novel histone deacetylase pathway regulates mitosis by modulating Aurora B kinase activity. *Genes Dev,* 20**,** 2566-79.
LIN, Q., FUJI, R. N., YANG, W. & CERIONE, R. A. 2003. RhoGDI is required for Cdc42-mediated cellular transformation. *Curr Biol,* 13**,** 1469-79.
LODISH, H. F. 2016. *Molecular cell biology / Harvey Lodish ... [et al.],* New York, New York : W.H. Freeman.
MAIELLARO, I. 2022. In Vivo cAMP Dynamics in Drosophila Larval Neurons. *In:* ZACCOLO, M. (ed.) *cAMP Signaling: Methods and Protocols.* New York, NY: Springer US.
MAIELLARO, I., LOHSE, M. J., KITTEL, R. J. & CALEBIRO, D. 2016. cAMP Signals in Drosophila Motor Neurons Are Confined to Single Synaptic Boutons. *Cell Rep,* 17**,** 1238-1246.
MALBON, C. C., TAO, J. & WANG, H. Y. 2004. AKAPs (A-kinase anchoring proteins) and molecules that compose their G-protein-coupled receptor signalling complexes. *Biochem J,* 379**,** 1-9.
MCCORMICK, K. & BAILLIE, G. S. 2014. Compartmentalisation of second messenger signalling pathways. *Current Opinion in Genetics & Development,* 27**,** 20-25.
MCGURK, L., MORRISON, H., KEEGAN, L. P., SHARPE, J. & O'CONNELL, M. A. 2007. Three-Dimensional Imaging of Drosophila melanogaster. *PLOS ONE,* 2**,** e834.
MCMURRAY, C. T. 2000. Neurodegeneration: diseases of the cytoskeleton? *Cell Death & Differentiation,* 7**,** 861-865.
MO, G. C., ROSS, B., HERTEL, F., MANNA, P., YANG, X., GREENWALD, E., BOOTH, C., PLUMMER, A. M., TENNER, B., CHEN, Z., WANG, Y., KENNEDY, E. J., COLE, P. A., FLEMING, K. G., PALMER, A., JIMENEZ, R., XIAO, J., DEDECKER, P. & ZHANG, J. 2017. Genetically encoded biosensors for visualizing live-cell biochemical activity at super-resolution. *Nat Methods,* 14**,** 427-434.
MOEYAERT, B. & DEDECKER, P. 2014. pcSOFI as a Smart Label-Based Superresolution Microscopy Technique. *In:* CAMBRIDGE, S. (ed.) *Photoswitching Proteins: Methods and Protocols.* New York, NY: Springer New York.

NIKOLAEV, V. O., BÜNEMANN, M., HEIN, L., HANNAWACKER, A. & LOHSE, M. J. 2004. Novel single chain cAMP sensors for receptor-induced signal propagation. *J Biol Chem,* 279**,** 37215-8.
OISHI, A., MAKITA, N., SATO, J. & IIRI, T. 2012. Regulation of RhoA signaling by the cAMP-dependent phosphorylation of RhoGDIα. *The Journal of biological chemistry,* 287**,** 38705-38715.
PALCZEWSKI, K., KUMASAKA, T., HORI, T., BEHNKE, C. A., MOTOSHIMA, H., FOX, B. A., LE TRONG, I., TELLER, D. C., OKADA, T., STENKAMP, R. E., YAMAMOTO, M. & MIYANO, M. 2000. Crystal structure of rhodopsin: A G protein-coupled receptor. *Science,* 289**,** 739-45.
PEREIRA, L., CHENG, H., LAO, D. H., NA, L., VAN OORT, R. J., BROWN, J. H., WEHRENS, X. H., CHEN, J. & BERS, D. M. 2013. Epac2 mediates cardiac β1-adrenergic-dependent sarcoplasmic reticulum Ca2+ leak and arrhythmia. *Circulation,* 127**,** 913-22.
PEREZ-MOCKUS, G., ROCA, V., MAZOUNI, K. & SCHWEISGUTH, F. 2017. Neuralized regulates Crumbs endocytosis and epithelium morphogenesis via specific Stardust isoforms. *J Cell Biol,* 216**,** 1405-1420.
PIGGOTT, L. A., BAUMAN, A. L., SCOTT, J. D. & DESSAUER, C. W. 2008. The A-kinase anchoring protein Yotiao binds and regulates adenylyl cyclase in brain. *Proceedings of the National Academy of Sciences,* 105**,** 13835-13840.
RAFTOPOULOU, M. & HALL, A. 2004. Cell migration: Rho GTPases lead the way. *Dev Biol,* 265**,** 23-32.
RASMUSSEN, S. G., DEVREE, B. T., ZOU, Y., KRUSE, A. C., CHUNG, K. Y., KOBILKA, T. S., THIAN, F. S., CHAE, P. S., PARDON, E., CALINSKI, D., MATHIESEN, J. M., SHAH, S. T., LYONS, J. A., CAFFREY, M., GELLMAN, S. H., STEYAERT, J., SKINIOTIS, G., WEIS, W. I., SUNAHARA, R. K. & KOBILKA, B. K. 2011. Crystal structure of the β2 adrenergic receptor-Gs protein complex. *Nature,* 477**,** 549-55.
RICHARDS, M., LOMAS, O., JALINK, K., FORD, K. L., VAUGHAN-JONES, R. D., LEFKIMMIATIS, K. & SWIETACH, P. 2016. Intracellular tortuosity underlies slow cAMP diffusion in adult ventricular myocytes. *Cardiovasc Res,* 110**,** 395-407.
RIDLEY, A. J. & HALL, A. 1992. The small GTP-binding protein rho regulates the assembly of focal adhesions and actin stress fibers in response to growth factors. *Cell,* 70**,** 389-99.
RIDLEY, A. J., PATERSON, H. F., JOHNSTON, C. L., DIEKMANN, D. & HALL, A. 1992. The small GTP-binding protein rac regulates growth factor-induced membrane ruffling. *Cell,* 70**,** 401-10.
ROBICHAUX, W. G., 3RD & CHENG, X. 2018. Intracellular cAMP Sensor EPAC: Physiology, Pathophysiology, and Therapeutics Development. *Physiol Rev,* 98**,** 919-1053.
ROSENBAUM, D. M., RASMUSSEN, S. G. & KOBILKA, B. K. 2009. The structure and function of G-protein-coupled receptors. *Nature,* 459**,** 356-63.

SAKAI, Y., TSUNEKAWA, M., OHTA, K., SHIMIZU, T., PASTUHOV, S., HANAFUSA, H., HISAMOTO, N. & MATSUMOTO, K. 2021. The Integrin Signaling Network Promotes Axon Regeneration via the Src–Ephexin–RhoA GTPase Signaling Axis. *The Journal of Neuroscience,* 41**,** 4754.

SASSONE-CORSI, P. 2012. The cyclic AMP pathway. *Cold Spring Harb Perspect Biol,* 4.

SCOTT, J. D., DESSAUER, C. W. & TASKÉN, K. 2013. Creating order from chaos: cellular regulation by kinase anchoring. *Annu Rev Pharmacol Toxicol,* 53**,** 187-210.

SELBIE, L. A. & HILL, S. J. 1998. G protein-coupled-receptor cross-talk: the fine-tuning of multiple receptor-signalling pathways. *Trends Pharmacol Sci,* 19**,** 87-93.

SHEN, J. X. & COOPER, D. M. 2013. AKAP79, PKC, PKA and PDE4 participate in a Gq-linked muscarinic receptor and adenylate cyclase 2 cAMP signalling complex. *Biochem J,* 455**,** 47-56.

SORIANO, O., ALCÓN-PÉREZ, M., VICENTE-MANZANARES, M. & CASTELLANO, E. 2021. The Crossroads between RAS and RHO Signaling Pathways in Cellular Transformation, Motility and Contraction. *Genes,* 12.

SPIERING, D. & HODGSON, L. 2011. Dynamics of the Rho-family small GTPases in actin regulation and motility. *Cell Adh Migr,* 5**,** 170-80.

SURDO, N. C., BERRERA, M., KOSCHINSKI, A., BRESCIA, M., MACHADO, M. R., CARR, C., WRIGHT, P., GORELIK, J., MOROTTI, S., GRANDI, E., BERS, D. M., PANTANO, S. & ZACCOLO, M. 2017. FRET biosensor uncovers cAMP nano-domains at β-adrenergic targets that dictate precise tuning of cardiac contractility. *Nat Commun,* 8**,** 15031.

SVITKINA, T. 2018. The Actin Cytoskeleton and Actin-Based Motility. *Cold Spring Harb Perspect Biol,* 10.

TAPON, N. & HALL, A. 1997. Rho, Rac and Cdc42 GTPases regulate the organization of the actin cytoskeleton. *Curr Opin Cell Biol,* 9**,** 86-92.

TAUSSIG, R. 2013. Adenylyl Cyclases. *In:* LENNARZ, W. J. & LANE, M. D. (eds.) *Encyclopedia of Biological Chemistry (Second Edition).* Waltham: Academic Press.

TAYLOR, S. S., KIM, C., VIGIL, D., HASTE, N. M., YANG, J., WU, J. & ANAND, G. S. 2005. Dynamics of signaling by PKA. *Biochim Biophys Acta,* 1754**,** 25-37.

TAYLOR, S. S., ZHANG, P., STEICHEN, J. M., KESHWANI, M. M. & KORNEV, A. P. 2013. PKA: Lessons learned after twenty years. *Biochimica et Biophysica Acta (BBA) - Proteins and Proteomics,* 1834**,** 1271-1278.

TONUCCI, F. M., ALMADA, E., BORINI-ETICHETTI, C., PARIANI, A., HIDALGO, F., RICO, M. J., GIRARDINI, J., FAVRE, C., GOLDENRING, J. R., MENACHO-MARQUEZ, M. & LAROCCA, M. C. 2019. Identification of a CIP4 PKA phosphorylation site involved in the regulation of cancer cell invasiveness and metastasis. *Cancer Lett,* 461**,** 65-77.

VAN HAASTERT, P. J. M., KEIZER-GUNNINK, I. & KORTHOLT, A. 2007. Essential role of PI3-kinase and phospholipase A2 in Dictyostelium discoideum chemotaxis. *Journal of Cell Biology,* 177**,** 809-816.
WILLOUGHBY, D. & COOPER, D. M. 2008. Live-cell imaging of cAMP dynamics. *Nat Methods,* 5**,** 29-36.
WILLOUGHBY, D., EVERETT, K. L., HALLS, M. L., PACHECO, J., SKROBLIN, P., VACA, L., KLUSSMANN, E. & COOPER, D. M. 2012. Direct binding between Orai1 and AC8 mediates dynamic interplay between Ca2+ and cAMP signaling. *Sci Signal,* 5**,** ra29.
WONG, W. & SCOTT, J. D. 2004. AKAP signalling complexes: focal points in space and time. *Nature Reviews Molecular Cell Biology,* 5**,** 959-970.
WOOTTEN, D., CHRISTOPOULOS, A., MARTI-SOLANO, M., BABU, M. M. & SEXTON, P. M. 2018. Mechanisms of signalling and biased agonism in G protein-coupled receptors. *Nature Reviews Molecular Cell Biology,* 19**,** 638-653.
WÜLBECK, C. & SIMPSON, P. 2002. The expression of pannier and achaete-scute homologues in a mosquito suggests an ancient role of pannier as a selector gene in the regulation of the dorsal body pattern. *Development,* 129**,** 3861-71.
YANG, D., ZHOU, Q., LABROSKA, V., QIN, S., DARBALAEI, S., WU, Y., YULIANTIE, E., XIE, L., TAO, H., CHENG, J., LIU, Q., ZHAO, S., SHUI, W., JIANG, Y. & WANG, M.-W. 2021. G protein-coupled receptors: structure- and function-based drug discovery. *Signal Transduction and Targeted Therapy,* 6**,** 7.
YANG, M., KOHLER, M., HEYDER, T., FORSSLUND, H., GARBERG, H. K., KARIMI, R., GRUNEWALD, J., BERVEN, F. S., NYRÉN, S., MAGNUS SKÖLD, C. & WHEELOCK, Å. M. 2018. Proteomic profiling of lung immune cells reveals dysregulation of phagocytotic pathways in female-dominated molecular COPD phenotype. *Respiratory Research,* 19**,** 39.
ZACCOLO, M. 2021. cAMP Buffering via Liquid-Liquid Phase Separation. *Function (Oxf),* 2**,** zqaa048.
ZACCOLO, M. & POZZAN, T. 2002. Discrete microdomains with high concentration of cAMP in stimulated rat neonatal cardiac myocytes. *Science,* 295**,** 1711-5.
ZACCOLO, M., ZERIO, A. & LOBO, M. J. 2021. Subcellular Organization of the cAMP Signaling Pathway. *Pharmacological Reviews,* 73**,** 278.
ZEITLINGER, J. & BOHMANN, D. 1999. Thorax closure in Drosophila: involvement of Fos and the JNK pathway. *Development,* 126**,** 3947-56.
ZHANG, J., MA, Y., TAYLOR, S. S. & TSIEN, R. Y. 2001. Genetically encoded reporters of protein kinase A activity reveal impact of substrate tethering. *Proceedings of the National Academy of Sciences,* 98**,** 14997.
ZHANG, J. Z., LU, T. W., STOLERMAN, L. M., TENNER, B., YANG, J. R., ZHANG, J. F., FALCKE, M., RANGAMANI, P., TAYLOR, S. S., MEHTA, S. & ZHANG, J. 2020. Phase Separation of a PKA

Regulatory Subunit Controls cAMP Compartmentation and Oncogenic Signaling. *Cell,* 182**,** 1531-1544.e15.

Appendix

A1. Gal4 UAS & MARCM & FLP FRT Systems

A1.1 The Gal4 UAS System

The Gal4/UAS system, relying on the yeast transcriptional activator Gal4, allows targeted gene expression within cells of a particular tissue during different developmental stages. It segregates the transcription factor from the transcriptional activator, allowing controlled activation of target gene transcription. The *driver line* contains a tissue-specific promoter, upstream of a sequence encoding the Gal4 transcription factor from yeast. The *responder line* contains the UAS (upstream activation sequence), upstream of the target gene to be expressed in the insect(Brand and Perrimon, 1993). The responder line is crossed with the driver line producing a fly which contains both Gal4 and the UAS. As the promoter in this system is tissue-specific, it only possesses activity in specific tissues, therefore by utilising a promoter which is specific for the tissue of interest, researchers can ensure the gene of interest is only expressed there(Brand and Perrimon, 1993). The tissue-specific promoters used in this study are Neuralized, which targets expression to the well-spaced SOP cells in the notum, and Pannier drives expression to the epithelial sheet in the notum. Neuralized is a highly conserved E3 ubiquitin ligase; it is a component of the Notch signalling pathway and is highly expressed in the pupal salivary gland making it ideal for driving gene transcription to the SOP cells(Lai et al., 2001, Perez-Mockus et al., 2017). On the other hand, Pannier encodes a zinc-finger transcription factor within the GATA family. It is implicated in dorsal sensory bristle patterning within the dorsal epidermis by repressing achaete-scute activity which is required to allow patterning(Wülbeck and Simpson, 2002). Thus, it is an ideal

candidate for driving expression to the noturm. Within the desired cell, RNA pol assembles on the promoter and the *gal4* gene is transcribed producing dimeric Gal4 protein(Brand and Perrimon, 1993). Gal4 dimers bind to the UAS by interacting with DNA via a double cysteine-6 zinc finger motif located at the N-terminus of Gal4. The UAS is a sequence of DNA which acts as an enhancer increasing the frequency of transcriptional bursts. This facilitates more transcription by increasing the activity of the core promoter for the transgene(Brand and Perrimon, 1993). Thus, transcription is activated and more RNA encoding the transgene is produced and translated to generate the gene product.

A1.2 The MARCM/FLP/FRT System

The FLP/FRT system is a inducible site-specific recombination technique which relies on recombination system of *Saccharomyces cerevisiae(Golic and Lindquist, 1989).* It relies on insertion of flippases (Flp), an enzyme which induces post-mitotic recombination during the G2 phase of the cell cycle, at identical flippase recognition sites (FRT) on homologous chromosomes within the *Drosophila melanogaster* genome(Golic and Lindquist, 1989). This produces homozygous mutant or homozygous wild-type daughter cells. The promoter *Ultrabithorax* can be employed to confine expression of the Flp to the notum. Addition of the Mosaic Analysis with a Repressible Marker system (MARCM) affords greater control of transgene expression. The MARCM system combines the FLP/FRT system with Gal80, a repressor of the transcriptional activator Gal4(Lee and Luo, 2001). Gal80 prevents gene transcription, therefore by inducing site-specific recombination of Gal80 in combination with the transgene, generates homozygous daughter cells without Gal80 and homozygous cells containing Gal80. This creates a mosaic of cells within the tissue; some will not express the UAS-transgene while homozygous mutants lacking the Gal80 freely express the UAS-transgene(Lee and Luo, 2001).

Furthermore, this system allows the expression of many UAS-transgenes within the genome.